GEORG-AUGUST-UNIVERSITÄT GÖTTINGEN

II. Physikalisches Institut

A Study of Tau Identification with the ATLAS Detector at the LHC

von

Philip James Ilten

An investigation of hadronic τ lepton identification and reconstruction with the ATLAS detector on the LHC is presented. Using a varying signal cone parameterized with respect to reconstructed τ lepton E_T is found to be detrimental to efficiency and fakerate. Parameterizing the isolation cone as an ellipse in ΔR is found to provide no noticeable advantages. Identification of hadronic τ leptons using cut flows, likelihoods, boosted decision trees, and artificial neural nets is demonstrated. Finally, a method for finding total hadronic τ lepton efficiency from data is implemented.

Friedrich-Hund-Platz 1
37077 Göttingen
Germany

II.Physik-UniGö-Dipl-2009/02
II. Physikalisches Institut
Georg-August-Universität Göttingen
March 2009

GEORG-AUGUST-UNIVERSITÄT

GÖTTINGEN

II. Physikalisches Institut

A Study of Tau Identification with the ATLAS Detector at the LHC

von

Philip James Ilten

Dieser Forschungsbericht wurde als Diplomarbeit von der Fakultät für Physik der Georg-August-Universität zu Göttingen angenommen.

Angenommen am:	March 20, 2009
Autor:	Philip James Ilten
Referent:	Prof. Dr. Markus Klute
Korreferent:	Prof. Dr. Hans Hofsäss

II.Physik-UniGö-Dipl-2009/02

Contents

1 Introduction

The Large Hadron Collider (LHC) at CERN with its unprecedented center of mass energies will allow physicists to test the current Standard Model and search for new physics, both seen and unforeseen by current theory. The ATLAS detector, positioned at one of the four interaction points of the LHC, will provide a window into the sub-atomic interactions being explored. Before any discoveries of new physics can be claimed however, the detector must be validated and calibrated by observing already known physics.

One particle that provides a handle on many known physics processes, such as Z and W boson decay, along with playing an important role in possible new physics, is the τ lepton, heaviest of the three Standard Model leptons. Many searches for both the Standard Model and the Minimal Supersymmetric Model Higgs bosons rely heavily upon reconstruction and identification of τ leptons.

To facilitate such searches along with verifying currently known physics, this paper explores the reconstruction and identification of τ leptons within the ATLAS detector using Monte Carlo simulation. The decay of the Z boson into a τ lepton pair is a known Standard Model process, but kinematically similar to possible decays from Higgs bosons. Subsequently, this paper examines simulated τ leptons from such decays, and their underlying kinematics along with possible backgrounds.

Chapter 2 begins by introducing the Standard Model and the theory behind the τ lepton. A detailed account is given on the various production mechanisms of the τ lepton from both known processes and hypothesized physics. Special attention is given to the Higgs boson sector, as the τ lepton plays an important role in both standard and supersymmetric models. Additionally, the theory behind τ lepton decay is explored.

Both the LHC and ATLAS detector are outlined in Chapter 3. A general explanation of the LHC is given, focusing on the basic design of the collider and the relevant operating parameters such as luminosity and beam energy. Summaries of the inner tracker, calorimeters, muon chambers, and trigger systems of the ATLAS detector are also given following the design of the LHC. Each of these sub-detectors is critical for the analysis performed within this paper.

After Chapter 3, a comprehensive description of the current methods used by ATLAS for reconstruction of hadronic τ leptons is provided in Chapter 4. Special focus is given to the definition of the signal and isolation cones used for reconstruction. The kinematics of τ lepton decays and how they relate to reconstruction through both the signal and isolation cone is explored. Efficiencies and fakerates are found for reconstructed hadronic τ leptons using a variety of definitions for signal and isolation cones.

While reconstruction and identification are interrelated and combined in many experiments, a distinct separation is made within ATLAS. Chapter 5 details the current identification methods being used by ATLAS for hadronic τ lepton identification along with the general variables used to distinguish τ leptons from other objects within the event. Current multivariate methods such as likelihoods, artificial neural nets, and boosted decision trees are investigated and compared against each other using efficiencies and fakerates.

Chapter 6 combines the results of Chapters 4 and 5 to calculate the total efficiency of hadronic τ leptons using a data driven method. Methods such as this will prove important in new physics

searches when the efficiencies of hadronic τ leptons are required to calculate cross sections. Finally, a conclusion is given in Chapter 7, discussing the results presented within this paper.

2 Theory

The theory behind high energy particle physics is one of the most successful scientific theories ever, yet still remains incomplete. The Standard Model describes the interactions of potentially fundamental half integer spin particles, fermions, and integer spin force carriers or bosons. A summary of the fundamental particles and forces of the Standard Model is given in Figure 2.1.

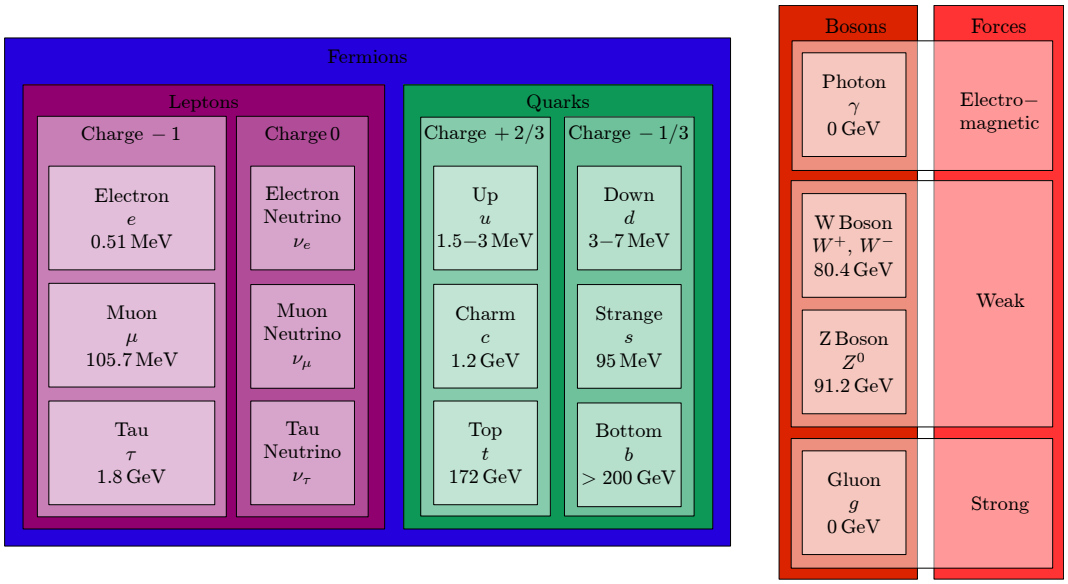

Figure 2.1: Summary of the fundamental particles of the Standard Model. Half integer spin particles, or fermions are outlined in blue, being further broken down into leptons and quarks. Both the leptons and quarks are split by charge, and arranged by generation from lightest to heaviest, with the mass given below the symbol for each particle, excluding the neutrinos. The integer spin bosons are outlined in red and matched with the corresponding force they carry. Figure adapted from Reference [1].

The three fundamental forces of the Standard Model are the electromagnetic force, the weak force, and the strong force. At higher energies the weak and electromagnetic forces unify to the electroweak force. The photon is the force carrier for the electromagnetic force, while the carriers of the weak force are the $W^{\pm}$ and Z bosons. Both the photon and Z boson are neutral while the $W^{\pm}$ bosons are charged. The gluon mediates the strong force and is neutral, but carries a color charge combination of red, blue, and green. The gravitational force is not explained by the Standard Model, and is much weaker than the remaining three forces on the size scale of fundamental particle interactions.

Fermions are grouped into leptons and quarks. The leptons interact through the electromagnetic force, weak interactions, and the gravitational force and have an integer charge of either one or zero. The charged leptons are split into three generations ordered both by mass and time of discovery: the electron, the muon, and the τ lepton. Corresponding to each charged lepton

is a light neutral lepton or neutrino with a neutrino flavor for each charged lepton, ν_e, ν_μ, and ν_τ. Recent experiments have measured the relative mass differences between neutrino flavors, indicating that neutrinos have mass, although no measurements of the absolute masses have yet been made [2].

Quarks interact through the same forces as the leptons but with the inclusion of the strong force. Because of the way in which the strong force acts, quarks are confined; they cannot exist without a partner in nature. This color confinement makes measuring individual quark masses difficult and explains why mass ranges are given in Figure 2.1. Just as the leptons are grouped in three generations, so are the quarks: u/d, c/s, and t/b. Each generation has a quark with charge $+2/3$ and another with charge $-1/3$. Quarks of either charge also must carry a color charge of either red, blue, or green.

All fermions have associated antiparticles with opposite charge and color charge. Combinations of quarks and anti-quarks generate hadrons. Currently, quarks have only been seen to combine in pairs or triplets. Quark pairs are mesons while quark triplets, such as the proton and neutron, are baryons.

The following two sections provide a more detailed examination of the above particles and their interactions. First an introduction to the formalism of the Standard Model is given, highlighting the Higgs mechanism, current shortcomings, and possible solutions and extended models such as supersymmetry. Following this underlying physics motivation, the properties and significance of the τ lepton are explored.

2.1 The Standard Model

The formalism of the Standard Model (SM) is local time dependent relativistic quantum field theory and is derived from classical field theory. The Lagrangian for a system, given by Equation 2.1 is the kinetic energy T less the potential V.

$$L = T - V \tag{2.1}$$

For a system of position and time dependent fields, the Lagrangian for the system can be defined as the integral of the Lagrangian density, $\mathcal{L}(\phi, \partial_\mu\phi, x_\mu)$, over all space. Here the Lagrangian density is dependent upon the fields of the system, $\phi(\vec{x})$, their subsequent derivatives $\partial\phi(\vec{x})/\partial x_\mu$, and the components x_μ of the time and space vector $\vec{x}$. The action of the system is the time integral of the Lagrangian,

$$S = \int L\, dx_0 = \int \mathcal{L}(\phi, \partial_\mu\phi, x_\mu)\, d^4\vec{x} \tag{2.2}$$

which in turn is the time and space integral of the Lagrangian density. Here, $\vec{x}$ represents the standard four vector of time and space, although Lagrangian formalism can be expanded to n-dimensions.

The equations of motion for the system are found by applying the "principle of least action" to the system: the evolution of a system over time is accomplished by an extremum of the action. Such a condition yields the Euler-Lagrange equation, Equation 2.3, which in turn provides the equations of motion for the system.

$$\partial_\mu \left(\frac{\partial \mathcal{L}}{\partial(\partial_\mu\phi)} \right) - \frac{\partial \mathcal{L}}{\partial \phi} = 0 \tag{2.3}$$

The field theory behind the Standard Model, however, is not classical, and modifications must be made accordingly to accommodate the relativistic and quantum nature of the Standard

Model. Relativity is accounted for by requiring the Lagrangian density to remain Lorentz invariant, as this will lead to a Lorentz invariant system. To obtain a quantum theory, fields are recast as operators, and interactions are calculated from the Lagrangian density.

The recasting of fields as operators introduces an interesting side effect. Evolution in time of interacting fields which produces particle interactions, cross sections, etc. can no longer be calculated exactly but must be found using perturbative theory. Here the Lagrangian density plays a crucial role by defining the Feynman rules of the system. Once the rules for a specific Lagrangian have been defined, quantities can be calculated by drawing the corresponding Feynman diagrams, and pertubartively adding the quantities from each diagram.

The underlying field theory of the Standard Model is rarely seen, and indeed the Feynman diagrams necessary for theoretical predictions are the primary instruments of particle physicists. However, the underlying symmetries of the Lagrangian densities define the Feynman rules, and it is from this underlying structure that it is easiest to understand the current short comings of the Standard Model [3].

2.1.1 Quantum Electrodynamics and Chromodynamics

The Dirac equation dictates the motion of an electron, and is the necessary stepping stone to create a Lagrangian density for electrodynamic theory. The Lagrangian density that satisfies the Dirac equation is given by,

$$\mathcal{L}_{\text{Dirac}} = i\psi^\dagger \gamma_\mu \partial^\mu \psi - m\psi^\dagger \psi \tag{2.4}$$

where γ_μ corresponds to the four Dirac matrices. This Lagrangian density is invariant under a phase shift $\psi \to e^{i\alpha}\psi$ where α is some constant, but the density is not locally gauge invariant, when $\alpha(\vec{x})$ is dependent on time and space. By requiring $\mathcal{L}_{\text{Dirac}}$ to be locally gauge invariant, theory is elegantly matched to experimental observation, and so the Lagrangian is modified by replacing ∂_μ with the covariant derivative D_μ defined in Equation 2.5.

$$D_\mu \equiv \partial_\mu - ieA_\mu \tag{2.5}$$

The field $\vec{A}$ is introduced to maintain the local gauge invariance of the Lagrangian density, and physically corresponds to the field of the photon. However, as a potential for the photon is added to the Lagrangian density by the covariant derivative, a kinetic term for the photon must also be added in the form of one half the square of the field strength tensor matrix $\mathbf{F}$ for $\vec{A}$ defined by Equation 2.6.

$$F_{\mu\nu} \equiv \partial_\mu A_\nu - \partial_\nu A_\mu \tag{2.6}$$

Substituting the covariant derivative of Equation 2.5 into Equation 2.4 with the addition of the photon kinetic energy of Equation 2.6 yields the full Lagrangian density of quantum electrodynamics (QED) given by Equation 2.7. Here the charge operator Q is introduced, which produces an eigenvalue of -1 when acted upon the field of an electron. Notice that the mass of the electron m must be given, and is not a prediction of the Lagrangian. However, the photon field $\vec{A}$ must remain massless. Introducing a mass term for $\vec{A}$ would spoil the gauge invariant nature of the Lagrangian density obtained by the introduction of $\vec{A}$.

$$\mathcal{L}_{\text{QED}} = \underbrace{\psi^\dagger \left(i\gamma^\mu \partial_\mu - m\right)\psi}_{\substack{\text{electron} \\ \text{KE/mass}}} - \underbrace{e\psi^\dagger \gamma^\mu Q \psi A_\mu}_{\text{interaction}} - \underbrace{\frac{1}{4} F_{\mu\nu} F^{\nu\mu}}_{\substack{\text{photon} \\ \text{KE}}} \tag{2.7}$$

Note that the group of this Lagrangian density is $U(1)$. In this case the basis for the unitary transformation is chosen to be the gauge transformation,

$$U\left(\alpha\left(\vec{x}\right)\right) \equiv e^{i\alpha(\vec{x})} \tag{2.8}$$

where $\alpha(\vec{x})$ is a scalar infinitesimal generator of $U(1)$. This group is Abelian, commutative under multiplication, and results in an invariant charge current density that does not change under transformation.

A similar process can be performed for quantum chromodynamics (QCD), which governs the interactions of quarks, by also assuming a gauge invariant Lagrangian density. However, quarks may assume a current of three different colors, and subsequently three color fields must be considered. The free Dirac Lagrangian density of Equation 2.4 now must accommodate three fields ψ_j, where j runs from 1 to 3 and represent the red, blue, and green color fields respectively.

$$\mathcal{L}_{\text{Dirac}} = i\psi_i^\dagger \gamma_\mu \partial^\mu \psi_j - m\psi_i^\dagger \psi_j \tag{2.9}$$

Equation 2.9 provides the Dirac Lagrangian density for QCD, taking into account only one quark flavor for simplicity and without loss of generality. Requiring that the Lagrangian density maintain gauge invariance is more complicated than for QED as the unitary matrix must now be of dimension three as defined in Equation 2.10.

$$U\left(\alpha\left(\vec{x}\right)\right) \equiv e^{i\alpha_a(\vec{x})\mathbf{T}_a} \tag{2.10}$$

The generators $\mathbf{T}_a$ are color operators and represent a basis for the possible color combinations carried by the gluon, corresponding to eight traceless matrices of dimension three. The operator $\mathbf{T}$ is the QCD equivalent of the charge operator of QED and and the algebra of $\mathbf{T}$ is the Lie algebra of Gell-Mann matrices. The gauge transformations defined by Equation 2.10 provide a unitary basis of dimension three, or an $SU(3)$ group. One of many possible representations of the eight possible $\mathbf{T}$ matrices is given in the compact form of Equation 2.11. Each linearly independent equation corresponds to a Gell-Mann matrix with r, b, and g representing the columns and $\bar{r}$, $\bar{b}$, and $\bar{g}$ the rows respectively [4].

$$\begin{aligned}
\mathbf{T}_1 &= \frac{1}{\sqrt{2}}\left(r\bar{b} + b\bar{r}\right) & \mathbf{T}_5 &= \frac{-i}{\sqrt{2}}\left(r\bar{g} - g\bar{r}\right) \\
\mathbf{T}_2 &= \frac{-i}{\sqrt{2}}\left(r\bar{b} - b\bar{r}\right) & \mathbf{T}_6 &= \frac{1}{\sqrt{2}}\left(b\bar{g} + g\bar{b}\right) \\
\mathbf{T}_3 &= \frac{1}{\sqrt{2}}\left(r\bar{r} - b\bar{b}\right) & \mathbf{T}_7 &= \frac{-i}{\sqrt{2}}\left(b\bar{g} - g\bar{b}\right) \\
\mathbf{T}_4 &= \frac{1}{\sqrt{2}}\left(r\bar{g} + g\bar{r}\right) & \mathbf{T}_8 &= \frac{1}{\sqrt{6}}\left(r\bar{r} + b\bar{b} - 2g\bar{g}\right)
\end{aligned} \tag{2.11}$$

Just as with QED, a vector field $\vec{G}$ is introduced in order to preserve gauge invariance. Now however, eight fields, $\vec{G}^a$, must be introduced, one for each generator corresponding to the basis representation of the eight possible color combinations given by Equation 2.11. To obtain gauge invariance under local $SU(3)$ transformations given by Equation 2.10, $\vec{G}$ must be transformed as,

$$G_\mu^a \rightarrow G_\mu^a - \frac{1}{g}\partial_\mu \alpha(\vec{x})_a - f_{abc}\alpha(\vec{x})_b G_\mu^c \tag{2.12}$$

where g is an arbitrary coupling constant, and f_{abc} are the structure constants of $SU(3)$.

The covariant derivative is,

$$D_\mu \equiv \partial_\mu + ig\mathbf{T}_a G_\mu^a \tag{2.13}$$

and the full Lagrangian density for QCD is given by Equation 2.14.

$$\mathcal{L}_{\text{QCD}} = \underbrace{\psi_i^\dagger \left(i\gamma^\mu \partial_\mu - m\right)\psi_j}_{\substack{\text{quark} \\ \text{KE/mass}}} - \underbrace{g G_\mu^a \psi_i^\dagger \gamma^\mu T_{ij}^a \psi_j}_{\text{interaction}} - \underbrace{\frac{1}{4} G_{\mu\nu}^a G_a^{\mu\nu}}_{\substack{\text{gluon} \\ \text{KE}}} \tag{2.14}$$

Again, introducing a mass term for the gluon would break the gauge symmetry of the Lagrangian density, just as it would for QED. However, the kinetic energy term of the gluon field is a self-interacting term. Gluons are allowed to couple to other gluons, unlike photons which cannot self-interact. Gluons carry color charge, and this is reflected in the non-commutative nature of the $SU(3)$ group [5].

2.1.2 The Weak Interaction and the Higgs Mechanism

While the previous section demonstrated that both QED and QCD can be represented by gauge invariant Lagrangian densities, a problem occurs when attempting to provide a Lagrangian density for the weak force. Prior to the discovery of the $W^\pm$ and Z bosons, it was known that the weak force must exist by the experimental observation of the neutron decaying to a proton, electron, and at the time, unobserved electron neutrino through β decay. However, at the energy levels of the available experiments, the presence of the weak force was not observed, prompting the conclusion that the weak force carriers must be massive on a scale above the attainable energy regime.

Requiring the weak force carriers to have mass would however, at first glance, eliminate the possibility of constructing a gauge invariant Lagrangian density for the weak force. However, through the introduction of the Higgs mechanism to a local $SU(2)$ symmetry, representing the charged and neutral currents of the weak force, massive bosons can be produced while maintaining the symmetry of the group. The following is a brief outline of the Higgs mechanism as first proposed by Peter Higgs [6].

Consider first a field $\phi(\vec{x})$ given by Equation 2.15 and a Lagrangian density given by Equation 2.16. Here μ is an arbitrary mass term and λ a self-coupling term.

$$\phi(\vec{x}) = \frac{1}{\sqrt{2}} \begin{pmatrix} \phi_1(\vec{x}) + i\phi_2(\vec{x}) \\ \phi_3(\vec{x}) + i\phi_4(\vec{x}) \end{pmatrix} \tag{2.15}$$

$$\mathcal{L}_{\text{Goldstone}} = \underbrace{\left(\partial_\mu \phi_i\right)^\dagger \left(\partial^\mu \phi_j\right)}_{\text{KE}} - \underbrace{\mu^2 \phi_i^\dagger \phi_j - \lambda \left(\phi_i^\dagger \phi_j\right)^2}_{\text{potential}} \tag{2.16}$$

The Lagrangian density must be invariant under gauge transformations given by Equation 2.17, where $\boldsymbol{\tau}_a$ are the unitary matrices of dimension two which are the infinitesimal generators of $SU(2)$. These operators correspond to the Q operator of QED and the $\mathbf{T}$ operator of QCD. For consistency the basis for $\boldsymbol{\tau}$ is chosen to be the three Pauli matrices.

$$U\left(\alpha\left(\vec{x}\right)\right) \equiv e^{i\alpha_a(\vec{x})\boldsymbol{\tau}_a} \tag{2.17}$$

Again, just as in QCD and QED a field $\vec{W}^a$ is introduced, this time allowing the index a to run from one to three, corresponding to the chosen basis representation of the $SU(2)$ group. To

maintain gauge invariance the following transformation to $\vec{W}^a$ must be made,

$$W_\mu^a \to W_\mu^a - \frac{1}{g}\partial_\mu \alpha(\vec{x})_a - f_{abc}\alpha(\vec{x})_b W_\mu^c \tag{2.18}$$

where the same notation as 2.12 is used. The covariant derivative is also defined,

$$D_\mu \equiv \partial_\mu + \frac{ig}{2}\boldsymbol{\tau}_a W_\mu^a \tag{2.19}$$

which when substituted into the Lagrangian density of Equation 2.16 provides the locally gauge invariant Lagrangian density for the weak force.

$$\mathcal{L}_{\text{Weak}} = \underbrace{\left(\partial_\mu \phi_i + \frac{ig}{2}\boldsymbol{\tau}_{ij}^a W_\mu^a \phi_i\right)^\dagger \left(\partial_\mu \phi_j + \frac{ig}{2}\boldsymbol{\tau}_{ij}^a W_\mu^a \phi_j\right)}_{\text{interaction and mass}} - \underbrace{V(\phi_{i,j})}_{\text{potential}} - \underbrace{\frac{1}{4}W_{\mu\nu}^a W_a^{\mu\nu}}_{\text{weak KE}} \tag{2.20}$$

When the potential is minimized,

$$\frac{\partial V(\phi)}{\partial \phi} = \mu^2 + 2\lambda\phi^\dagger\phi = 0 \tag{2.21}$$

there exist infinite solutions to the four fields contained in ϕ. Arbitrarily, the fields ϕ_1, ϕ_2, and ϕ_4 can be set to zero and ϕ_3^2 to $-\mu^2/\lambda \equiv v^2$. The field ϕ expanded around this minima for the potential is given in Equation 2.22 where $h(\vec{x})$ is the Higgs field.

$$\phi(\vec{x}) = \frac{1}{\sqrt{2}}\begin{pmatrix} 0 \\ v + h(\vec{x}) \end{pmatrix} \tag{2.22}$$

Assuming that $\mu^2 < 0$ the three fields $\vec{W}^a$ acquire mass, corresponding to the three weak bosons, and a neutral massive scalar H, the Higgs boson, is created. The mass of the Higgs is uniquely determined by the quartic self-coupling parameter λ and given in Equation 2.23.

$$M_H = v\sqrt{2\lambda} \tag{2.23}$$

The value v, vacuum expectation of the Higgs field, has been experimentally determined to be 246 GeV from the Fermi coupling, $v = (\sqrt{2}G_F)^{-1/2}$, where the Fermi coupling is determined from precision measurements of muon decay [7].

The above exposition does not provide a full Lagrangian for electroweak unification theory, nor is it intended to. The intention is merely to provide a conceptual idea of how spontaneous symmetry breaking through the Higgs mechanism allows for massive vector bosons while maintaining local gauge invariance. The necessary byproduct of a massive scalar boson allows for a testable hypothesis of the Standard Model with a single free parameter.

An electroweak unification theory is provided by Weinberg and Salam [8, 9] in $SU(2)_L \otimes U(1)_Y$ theory where L is weak isospin and Y hypercharge. The theory was proven to be renormalizable by 't Hooft [10] and lead to the experimentally verified prediction of masses for the $W^\pm$ and Z bosons. The current Standard Model is a $SU(3)_C \otimes SU(2)_L \otimes U(1)_Y$ theory where the Higgs mechanism has been introduced to the full Lagrangian density, coupling to both fermions and the massive gauge bosons. The Standard Model however is is not unified; just as the coupling constants of the $SU(2)$ and $U(1)$ components of electroweak theory are independent, so is the coupling constant of $SU(3)$. This separation of coupling constants has lead to the proposal of various unified theories of a higher order. Glashow and Georgi proposed that $SU(5)$ is the gauge group of such a unified theory [11], which has since been ruled out, and more recent attempts at unification theory have lead to supersymmetric models.

2.1.3 Beyond the Standard Model

One possible extension of the Standard Model, supersymmetry (SUSY), proposes an operator that transforms fermions to bosons, and bosons to fermions. Such an introduction allows for the unification of the three SM gauge coupling constants at the Plank energy scale of 10^{19} GeV. Additionally, the intrinsic instability of the SM through the gauge hierarchy problem, where incredibly precise fine-tuning of the cancellation between quadratic radiative corrections for the Higgs and the Higgs bare mass result in a Higgs much lighter than the Planck energy scale, can be resolved with a natural explanation [12]. Furthermore, the minimal supersymmetric model (MSSM) provides possible explanations for the large amounts of dark matter observed to exist within the universe [13].

A detailed explanation of MSSM will not be given here, as it is not within the scope of this paper. However, excellent reviews are available from Reference [13] and Reference [14]. Within the MSSM, two Higgs fields are required to maintain local gauge invariance, h_d and h_u, which couple exclusively with the down-type/up-type quarks and leptons respectively. Each field has a corresponding vacuum expectation value specified by Equation 2.24 where v is defined in Section 2.1.2.

$$v_d^2 + v_u^2 = v^2 \tag{2.24}$$

The result of two Higgs fields leads to five Higgs bosons: a charged pair $H^{\pm}$, a $\mathcal{CP}$-even light neutral h^0, a $\mathcal{CP}$-even heavy neutral H^0, and a $\mathcal{CP}$-odd neutral A^0. The quantity $\tan\beta$ given by Equation 2.25 is a free parameter of the model and defined by the ratio of the vacuum expectation value for h_u to the vacuum expectation value for h_d. An additional free parameter, the mass of the $\mathcal{CP}$-odd neutral must also be specified.

$$\tan\beta = \frac{v_u}{v_d} \tag{2.25}$$

Further supersymmetric models exist, including minimal supergravity (mSUGRA), gauge mediated supersymmetry (GMSM), and anomaly mediated supersymmetry (AMSM). All such supersymmetric models have advantages and disadvantages, and no particular model is considered the definitive model. Both MSSM and mSUGRA have larger support than other models, but neither remains problem free.

2.2 The Tau Lepton

The identification of tau leptons is crucial for the discovery of many proposed new physics processes. The following two sections highlight the possible productions of τ leptons, along with the subsequent decay of the τ lepton. A special emphasis is placed on the SM Higgs boson, as the τ lepton will play a critical role in searches for the SM Higgs at the LHC.

2.2.1 Decay

The τ lepton is the most massive of the three leptons, as shown earlier in Figure 2.1, with a mass of 1777 MeV. In 1975 at the Stanford Linear accelerator, 64 events were observed to have the detected form of $e^+ + e^- \rightarrow e^{\pm} + \mu^{\mp}$, but with a momentum and energy that could not be conserved if the decay was only through two bodies. The hypothesis set forth in the original paper [15], postulated that the undetected particle was either a heavy lepton or charged boson. The paper states that the undetected particles either escaped the fiducial region of the detector,

or, were "particles very difficult to detect". While much has been learned about the τ lepton over the years, the initial statement of the τ lepton being "very difficult to detect" remains true.

The mean lifetime of the τ lepton is given by Equation 2.26,

$$\tau_\tau = \left(\frac{G_F^2 \mu^5}{192\pi^3}\right)\left(\frac{m_\mu}{m_\tau}\right)^5 BR(\tau \to \mu) \tag{2.26}$$

where the first term corresponds to the mean lifetime of the muon. The branching ratio of the τ lepton to a muon can also be calculated from theory, as will be shown shortly. Measurements of the τ lepton lifetime have placed it at $290.6 \pm 1.0 \times 10^{-15}$ seconds, which in comparison to the muon lifetime is very short, as expected due to the large mass difference [16].

This short lifetime of the τ lepton makes identification difficult. Due to the τ lepton's high mass, all remaining leptons and a variety of lighter hadrons, are available as decay products, providing a large variety of decay channels. This variety in turn makes proper identification even more difficult. Figure 2.2 gives the three possible τ lepton decay channels: leptonic, radiative leptonic, and hadronic.

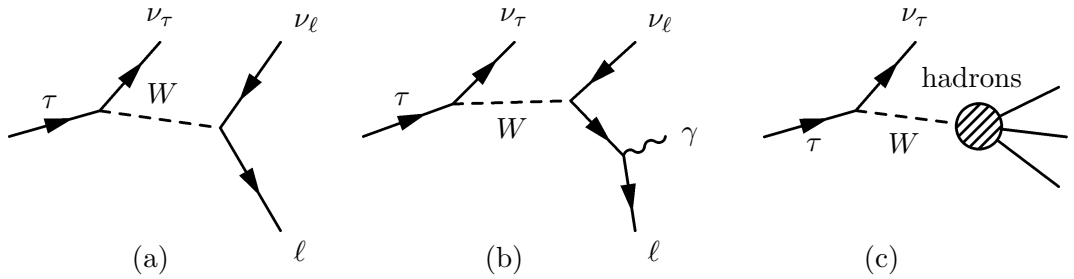

Figure 2.2: The three possible decay modes of the τ lepton: (a) leptonic, (b) radiative leptonic, and (c) hadronic.

Leptonic

The first two diagrams of Figure 2.2 depict leptonic decays of the τ lepton which account for approximately 35% of all decays. Pure leptonic decay consists of two weak vertices which can be determined from electroweak theory and complete calculations for decay widths, momenta spectra, and angular distributions can be performed. Furthermore, radiative corrections can be applied to determine the decay width for leptonic and radiative leptonic decays. Equation 2.27 provides the decay width for muon and electron decay with radiative corrections included [17].

$$\begin{aligned}\Gamma\left(\tau \to \nu_\tau \ell \nu_\ell(\gamma)\right) = &\frac{G_F^2 m_\tau^2}{192\pi^3}\left(\frac{m_\ell^2}{m_\tau^2}\right)\left(1 + \frac{3}{5}\frac{m_\tau^2}{m_W^2}\right)\left(1 - 8x_\ell + 8x_\ell^3 - x_\ell^4 - 12x_\ell^2 \ln x_\ell\right) \\ &\left(1 + \frac{\alpha(m_\tau)}{2\pi}\left(\frac{25}{4} - \pi^2\right)\right)\end{aligned} \tag{2.27}$$

Here the quantity x_ℓ is defined as m_ℓ^2/m_τ^2 and the constant $\alpha(m_\tau)$ is the fine structure constant at the mass of the τ lepton where $\alpha^{-1}(m_\tau) \approx 133.3$.

From the form of the above equation it is apparent that the decay widths for both the electron and muon products should be similar, with the electron width slightly larger due to the electron's

lighter mass. This is the case and experiment closely matches the theory with the τ lepton decay to electrons measured to be $17.85 \pm 0.05\%$ and the decay to muons measured to be $17.36 \pm 0.05\%$ [18].

Hadronic

Due to the QCD nature of the hadronic decay channels of the τ lepton, no general theoretical form for the decay width can be given. However, a hadronic decay can be generalized to the form of $\tau^{\pm} \to \nu_{\tau} \hbar^{\pm}$. Here, $\hbar^{-}$ corresponds to all hadronic decay products with a total negative charge. Equation 2.28 provides a decay width for this generalized decay process [19].

$$\begin{aligned}\Gamma\left(\tau \to \nu_{\tau} \hbar\right) = & \frac{G_F m_{\tau}^2}{32\pi^2} \int_0^{m_{\tau}^2} dq^2 \left(1 - \frac{q^2}{m_{\tau}^2}\right) \left[\cos^2\theta_c \left(\left(1 + 2\frac{q^2}{m_{\tau}^2}\right)\right.\right. \\ & \left.\left(v_1(\hbar, q^2) + a_1(\hbar, q^2)\right) + a_0(\hbar, q^2)\right) + \sin^2\theta_c \left(\left(1 + 2\frac{q^2}{m_{\tau}^2}\right)\right. \\ & \left.\left.\left(v_1^s(\hbar, q^2) + a_1^s(\hbar, q^2)\right) + v_0^s(\hbar, q^2) + a_0^s(\hbar, q^2)\right)\right]\end{aligned} \tag{2.28}$$

In Equation 2.28, q is the invariant mass of the hadronic system, $\hbar$, while v_J and a_J designate continuous spectral functions in q. The a function corresponds to the axial part of the weak charged current while v is given by the Lorentz vector part of the current. Each spectral function is broken into parts by the spin subscript J while the superscript s denotes a strange state of $\hbar$. The normal definition for the Cabbibo mixing angle $\theta_c \equiv \tan^{-1}|V_{us}/V_{ud}|$ is used.

In the case of a single charged pion decay, the spectral functions are represented by a delta distribution due to the the decay of $\pi^+ \to \mu^+ \nu_{\mu}$ and its corresponding charge conjugate. The low mass of both the neutral and charged pion in conjunction with the general representation of the hadronic decay width of Equation 2.28 favors pions in the final decay state of the τ lepton. Experiment agrees with theory and pion decays are indeed favored with $BR(\tau^- \to \nu_{\tau}\pi^-) \approx 12\%$, $BR(\tau^- \to \nu_{\tau}\pi^-\pi^0) \approx 25\%$, $BR(\tau^- \to \nu_{\tau}\pi^-2\pi^0) \approx 11\%$, and $BR(\tau^- \to \nu_{\tau}\pi^-\pi^+\pi^-) \approx 10\%$ with the corresponding ratios for the τ^+ lepton [18]. Including small contributions from channels involving kaons and other heavier hadrons along with the two leptonic channels accounts for all known τ lepton decays.

For purposes of identification within a particle detector the τ lepton decays are grouped by number of charged particles and are refered to as one, three, and five prong decays which correspond to one, three, and five charged particles respectively. Table 2.1 gives a general overview of the branching ratios grouped with respect to number of charged particles. Within this paper for notational purposes, ℓ is either an electron or muon, while $\hbar$ is a hadron.

2.2.2 Production

The τ lepton can be produced from a variety of processes, including known SM processes, hypothetical SM Higgs decays, hypothetical MSSM Higgs decays, and hypothetical superparticle (sparticle) decays. The following outlines these possible channels of τ lepton production within the LHC.

Channel	Percent	
one prong decays		
$\Rightarrow\ \nu_\tau h^- + h^0 \geq 1$	37%	**85**%
$\Rightarrow\ \nu_\tau \ell^- \bar{\nu}_\ell$	35%	
$\Rightarrow\ \nu_\tau h^-$	12%	
three prong decays		
$\Rightarrow\ \nu_\tau h^- h^- h^+$	10%	**15**%
$\Rightarrow\ \nu_\tau h^- h^- h^+ + h^0 \geq 1$	5%	
five prong decays	$< \mathbf{1}\%$	

Table 2.1: Table of primary decay channels for the τ lepton adapted from Reference [1]. Data taken from Reference [18].

Standard Model Processes

The two primary SM processes contributing to τ lepton production at the LHC are $W^\pm$ decay and Z decay. The $W^\pm$ is experimentally measured to have a branching ratio of $11.25 \pm 0.20\%$ to a τ lepton and corresponding τ neutrino and is expected to be produced in large quantities by top and bottom quark decays from top and bottom pair production at the LHC. The Z decays to a τ lepton pair in $3.370 \pm 0.008\%$ of all decays [18]. The Drell-Yan Z production and decay has been well observed by previous experiments and will provide a standard candle for the LHC detectors. The process itself, while used as the signal for this paper, is not of interest for new physics and is considered a background for new physics searches as the process will be kinematically similar to that of a Higgs decay. Details on expected cross sections for both W and Z production at the LHC can be found in Reference [20] and the $Z \rightarrow \tau^+\tau^-$ process is examined more closely in Section 4.2.1.

Additionally, τ leptons can be formed through the decay of charged B mesons, $B^\pm \rightarrow \bar{D}^0 \tau^\pm \nu_\tau$, or charged D mesons, $D^\pm \rightarrow \tau^\pm \nu_\tau$. In the case of the charged B meson, $2.2 \pm 0.6\%$ of all decays result in a τ lepton and neutrino with an additional neutral D meson. Further decays for the charged B meson have been observed but are less than $0.7 \pm 0.4\%$ of decays. The D meson decay is negligible with an upper limit of $< 0.21\%$.

The SM Higgs Boson

The SM Higgs boson can be produced through a variety of mechanisms at the LHC, as shown in the Feynman diagrams of Figure 2.3. The upper left diagram demonstrates gluon gluon fusion, the leading production mechanism for the SM Higgs at the LHC as shown in the right plot of Figure 2.4. The next to leading order production mechanism is weak boson fusion, shown in the lower right diagram of Figure 2.3. The bottom left diagram demonstrates associated W production, and the top right gives associated top/bottom quark pair production.

Weak boson fusion is of special interest as it provides a much cleaner signal than gluon gluon fusion. Since both quark jets maintain color flow preservation and are highly boosted, jet activity within the central region of the detector is surpressed. The subsequent decay of the Higgs occurs within the cleaner central region of the detector, allowing for better identification of the decay products. The two quark jets also provide a means for eliminating background. An ATLAS study on weak boson fusion using fully simulated signal and backgrounds can be found in Reference [21].

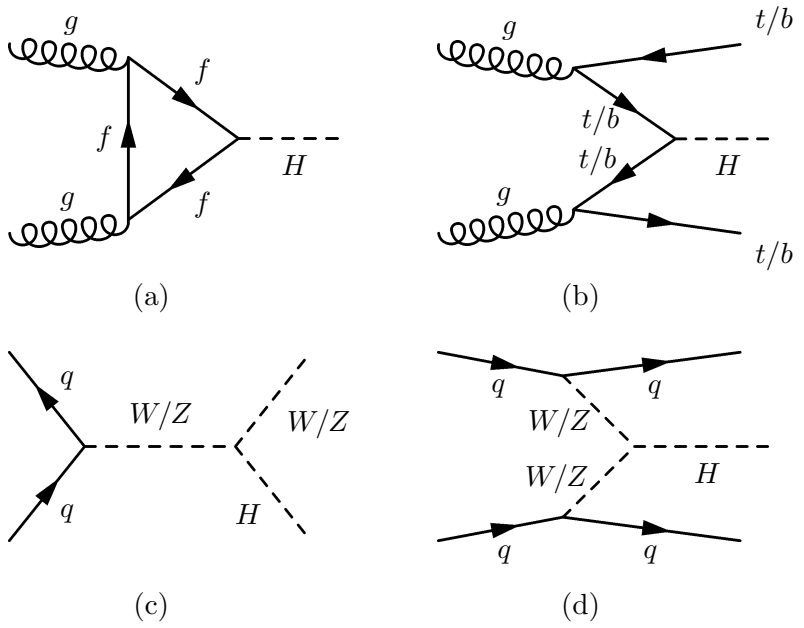

Figure 2.3: Production mechanisms of the SM Higgs boson at the LHC: (a) gluon gluon fusion, (b) top/bottom associated production, (c) W/Z associated production, (d) weak boson fusion.

The leading order decay width of the SM Higgs boson to fermion pairs is given by Equation 2.29 [22]. Here N_C specifies the number of colors available, M_f the mass of the fermion, M_H the mass of the SM Higgs, and G_F the Fermi coupling constant.

$$\Gamma(H \to \bar{f}f) = \frac{N_C G_F M_f^2 M_H}{4\sqrt{2}\pi} \left(1 - \frac{4M_f^2}{M_H^2}\right)^{3/2} \tag{2.29}$$

The form of Equation 2.29 arises from the stronger coupling of more massive particles with the Higgs field. As can be seen, both the b quark and τ lepton will have distinct advantages as decay products over the remaining fermions for a Higgs mass less than twice the top mass. Similar leading order decays for the decay width of the SM Higgs to W^+W^- and ZZ pairs is written in Equations 2.30 and 2.31 respectively [23].

$$\Gamma(H \to W^+W^-) = \frac{G_F M_W^2}{8\pi\sqrt{2}} \frac{\sqrt{1 - x_W}}{x_W} \left(3x_W^2 - 4x_W + 4\right) \tag{2.30}$$

$$\Gamma(H \to ZZ) = \frac{G_F M_W^2}{16\pi\sqrt{2}} \frac{\sqrt{1 - x_Z}}{x_W} \left(3x_Z^2 - 4x_Z + 4\right) \tag{2.31}$$

The value x_W is defined as $4M_W^2/M_H^2$ and x_Z as $4M_Z^2/M_H^2$ which can also be written in terms of x_W and the W mixing angle, $x_W/\cos^2\theta_W$. The left plot of Figure 2.4 shows the branching ratios for the SM Higgs decay versus Higgs mass with next to leading order QCD corrections included in the calculation [24].

From the above decay widths and Figure 2.4 it can be seen that for low masses of the SM Higgs, $M_H < 140$ GeV, the fermionic channels will dominate the Higgs decay with the most massive available fermionic pair, $b\bar{b}$, contributing as leading order. However, separating Higgs $b\bar{b}$ events from QCD backgrounds can be difficult leaving the next to leading order $\tau^+\tau^-$ channel

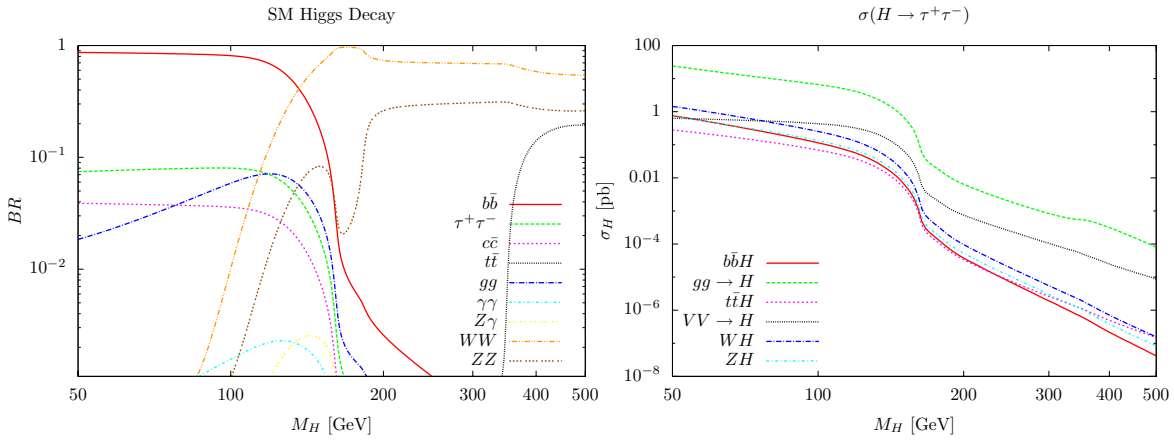

(a) (b)

Figure 2.4: Branching ratios for the SM Higgs decay calculated using NLO QCD corrections with HDECAY [25] are given in (a). Production cross sections for SM Higgs production within the LHC environment at $\sqrt{s} = 14$ TeV with a final $\tau^+\tau^-$ state are given in (b) with details given in Appendix D.

as the preferred signal. Note that this decay channel is the channel of choice for low mass Higgs searches and as such, hadronic τ lepton identification is of vital importance.

At higher Higgs masses, $M_H > 140$ GeV, the W^+W^- and ZZ channels dominate the Higgs decay. From these channels it is possible to identify a Higgs signal through a two lepton decay in the case of the W^+W^- channel, and a four lepton decay in the case of the ZZ channel. While the preferred identification of these two signals will be through electron and muon identification, including hadronic τ lepton identification will increase statistics.

Specifically, the efficiencies for the ZZ and W^+W^- channels is given in Equation 2.32, assuming an identification criteria of four or two leptons respectively.

$$\begin{aligned} \varepsilon_{H\to ZZ} &= \sum_{i=e,\mu,\tau} \sum_{j=e,\mu,\tau} \delta_i^2 BR_i \delta_j^2 BR_j \\ \varepsilon_{H\to WW} &= \sum_{i=e,\mu,\tau} \sum_{j=e,\mu,\tau} \delta_i BR_i \delta_j BR_j \end{aligned} \tag{2.32}$$

Here δ_i is defined by Equation 2.33 where δ_i(leptonic) considers only leptonically decaying τ leptons, and δ_i(hadronic) includes hadronically decaying τ leptons. The quantity BR_i is the branching ratio of either the Z or the W to lepton i for the respective expressions and also the branching ratio of the τ lepton in Equation 2.33. The value ε_i is the identification efficiency for the corresponding lepton. In the case of the τ lepton, this efficiency is for hadronically decaying τ leptons only.

$$\begin{aligned} \delta_i(\text{leptonic}) &= \begin{cases} \varepsilon_e BR(\tau \to e) + \varepsilon_\mu BR(\tau \to \mu) & i = \tau \\ \varepsilon_i & i \neq \tau \end{cases} \\ \delta_i(\text{hadronic}) &= \begin{cases} \varepsilon_e BR(\tau \to e) + \varepsilon_\mu BR(\tau \to \mu) + \varepsilon_\tau BR(\tau \to \hbar) & i = \tau \\ \varepsilon_i & i \neq \tau \end{cases} \end{aligned} \tag{2.33}$$

Equation 2.34 presents the results for an efficiency of 91% (excluding trigger efficiencies and detector acceptance) for muon identification, 77% for electron identification, and 30% for hadronic τ lepton identification. The efficiencies above are taken from preliminary ATLAS studies [26] and are only meant as rough estimates for a possible analysis.

$$\frac{\varepsilon_{H\to ZZ}(\text{hadronic})}{\varepsilon_{H\to ZZ}(\text{leptonic})} \approx 1.21 \qquad \frac{\varepsilon_{H\to WW}(\text{hadronic})}{\varepsilon_{H\to WW}(\text{leptonic})} \approx 1.22 \tag{2.34}$$

As can be seen, including hadronic τ leptons, even with a diminished efficiency increases the signal by nearly 20% for both the ZZ and W^+W^- cases. However, the analysis is not as simple as outlined above. Including both leptonic and hadronic τ lepton channels significantly complicates the analysis with larger missing transverse energy, triggering issues, introducing new backgrounds, etc. Despite these complications, it is clear that the τ lepton is important for high mass SM Higgs searches and critical for low mass SM Higgs searches.

The MSSM Higgs Bosons

The τ lepton also plays a vital role in searches for the MSSM Higgs bosons. The decay channels for h^0 of a significance greater than 10^{-4}% are the same channels as those shown for the SM Higgs in Figure 2.4. Significant decays for the H^0 include b quark, τ lepton, muon, and s quark pair production along with decays to the lighter MSSM Higgs: h^0h^0, A^0A^0, A^0Z, and $W^\pm H^\mp$. For the $\mathcal{CP}$-odd A^0 the same fermion pair production as the H^0 is significant along with the gg, $\gamma\gamma$, γZ, and h^0Z channels. For the charged H^+ $c\bar{b}$, $\tau^+\nu_\tau$, $\mu^+\nu_\mu$, $u\bar{s}$, $c\bar{s}$, $t\bar{b}$, h^0W^+, and A^0W^+ are all significant decay channels, with the subsequent charge conjugates for the H^-. In general, larger $\tan\beta$ enhances coupling of the Higgs bosons to the heavier fermions.

As the decay widths for each MSSM Higgs boson change with respect to the free parameters, $\tan\beta$ and M_{A^0}, and due to the large number of possible channels, an attempt to demonstrate the percentages of each channel is not made. However, the plots of Figure 2.5 demonstrate the relevant τ lepton decay channels for each MSSM boson versus M_{A^0} for $\tan\beta = 3$ and 30, while assuming the $m_{h^0}^{\max}$ scenario. This scenario ensures conservative exclusion of $\tan\beta$ by choosing the free parameters such that the Higgs boson masses are at a maximum for a specified $\tan\beta$; more details are outlined in Reference [27]. Current ATLAS studies place the maximum discoverable M_{A^0} within the ATLAS detector at 500 GeV [28] and searches at LEP have placed the bounds $m_{h^0} > 92.8$ and $M_{A^0} > 93.4$ GeV with a 95% confidence level [18].

For $M_{H^+} < 180$ GeV ($M_{A^0} < 142$ GeV) and a low $\tan\beta$ of 3 the H^+ decay products are $\tau^+\nu_\tau$ for over 50% of decays. Note, however, that this corresponds to $M_{h^0} < 94$, indicating that the discovery of a H^+ through the $\tau^+\nu_\tau$ for low $\tan\beta$ is unlikely as it is places m_{h^0} close to the current excluded range. As $\tan\beta$ increases so does the probability of the τ lepton channel, and for $\tan\beta = 30$, at least 90% of decays are $\tau^+\nu_\tau$ up to $M_{H^+} < 180$ GeV corresponding to $M_{A^0} < 165$ GeV and $M_{h^0} \approx 118$ GeV. This occurs from the larger Yukawa couplings of the third generation of fermions. From this it is clear that the $\tau^+\nu_\tau$ channel is important for identification of the H^+ decay for high $\tan\beta$.

Both the A^0 and H^0 have significant τ lepton decays for both low and high $\tan\beta$ although the branching ratios for τ lepton channels increase for higher $\tan\beta$, as expected. While not on the order of the $H^\pm$ decay, rates remain constant near 10% for both A^0 and H^0 at $\tan\beta = 30$. For low $\tan\beta$ the A^0 decay to τ leptons remains near 10% for $M_{A^0} < 340$ GeV. The H^0 decay channel for low $\tan\beta$ is not as promising as the A^0, with a branching ratio of 8% for $M_{A^0} < 140$ GeV. For masses above this, the H^0 τ lepton branching ratio remains below 3%.

The light MSSM Higgs, h^0 also has a significant branching fraction to a $\tau^+\tau^-$ final state. From both plots of Figure 2.5 it can be seen that for nearly all $\tan\beta$ and M_{A^0} a τ lepton pair is produced in approximately 8% of decays from the h^0.

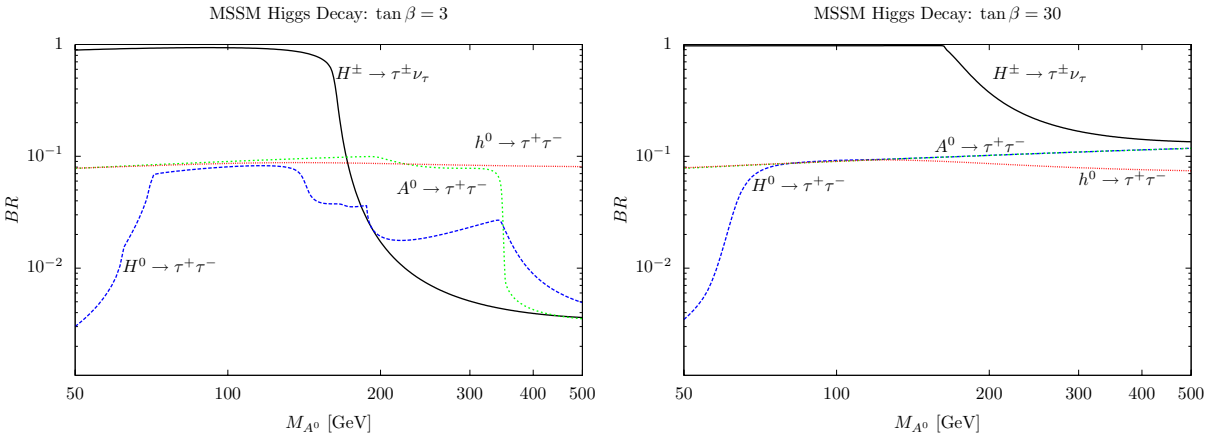

Figure 2.5: Branching ratios for the five MSSM Higgs bosons decaying to final products containing τ leptons. The parameter $\tan\beta$ is fixed at 3 (a) and 30 (b) while the ratios are plotted with respect to the remaining free parameter, M_{A^0}. Note $M_{h^0} > 92.8$ GeV given $M_{A^0} > 134.6$ GeV for $\tan\beta = 3$ while $M_{h^0} > 92.8$ GeV given $M_{A^0} > 93.9$ GeV for $\tan\beta = 30$. The plot was made neglecting LSP decay using HDECAY [25] with full details given in Appendix D.

Full Higgs Sector

In order to fully emphasize the importance of the τ lepton for a Higgs discovery and exploration, Figure 2.7 shows the cross sections for MSSM Higgs events with final states containing τ leptons. The right plot of Figure 2.4 shows the same cross sections, but for the SM Higgs. Here H corresponds to the SM Higgs, h^0 to the light MSSM Higgs, H^0 to the heavy MSSM Higgs, A^0 to the $\mathcal{CP}$-odd MSSM Higgs, and $H^\pm$ to the charged Higgs. A $m_{h^0}^{\max}$ benchmark scenario is assumed, just as in Figure 2.5.

Note that the number of events for a specific process with a given integrated luminosity, shown by Equation 2.35, is directly proportional to the cross section of that process.

$$N_{\text{events}} = \mathscr{L}_{\text{int}} \cdot BR(X \to \tau^+\tau^-) \cdot \sigma(X) \tag{2.35}$$

The variable X represents one of the neutral SM or MSSM Higgs bosons, while $BR(X \to \tau^+\tau^-)$ is the branching ratio of that specific Higgs into a τ lepton pair. The integrated luminosity, $\mathscr{L}_{\text{int}}$, is highly dependent upon operational parameters during data taking and is explained further in Section 3.1.

The production mechanisms are broken into the diagrams of Figure 2.3 with $b\bar{b}$ and $t\bar{t}$ associated production corresponding to (b), gg fusion production corresponding to (a) with next to leading order gq and qq production included, associated W and Z production corresponding to (c), and VV fusion corresponding to (d). For the SM Higgs, leading order production through the gg channel begins with $\sigma(H \to \tau^+\tau^-) \approx 4.7$ pb at a mass of $M_H \approx 115$ GeV and drops off below 0.05 pb for masses above ≈ 165 GeV. The remaining mechanisms for the SM Higgs

also produce a similar curve, but beginning at $\sigma(H \to \tau\tau) \approx 0.7$ pb for $M_H \approx 115$ GeV and dropping below 0.05 pb for $M_H > 155$ GeV.

For MSSM Higgs productions, leading order production is primarily through gg fusion for low $\tan\beta$ and $b\bar{b}$ associated production for high $\tan\beta$. Beginning at a mass of $M_{A^0} = 135$ for $\tan\beta = 3$ the leading order production cross section for the light MSSM Higgs is $\sigma(h^0 \to \tau^+\tau^-) \approx 5.7$ pb and dominates the production cross sections for both H^0 and A^0 for nearly all M_{A^0}. The production of H^0 and A^0 is significantly lower than that of h^0 with the leading order production starting at $\sigma(H^0 \to \tau^+\tau^-) \approx 1.5$ pb and $\sigma(A^0 \to \tau^+\tau^-) \approx 1.5$ for $M_{A^0} = 135$.

At $\tan\beta = 30$ the production cross sections for all MSSM Higgs bosons increases by nearly two orders of magnitude for τ final products, as expected from Figure 2.5. For the minimum excluded mass of $M_{A^0} = 93.9$ the leading order production for the light h^0 is both gg fusion and associated bottom production, while for the A^0 and H^0 the leading order production is gg fusion. For $M_{A^0} > 115$ GeV associated bottom production becomes leading order for A^0 and H^0 production. Gluon gluon fusion becomes the dominating production for h^0 at $M_{A^0} > 130$ GeV.

For luminosities on the order described in Section 3.1 these cross sections translate into over $500,000$ observable Higgs events with a τ lepton final state at the LHC within a year of nominal activity. While nominal activity is not expected within the near future, the significance of τ lepton channels for Higgs searches is apparent.

Sparticles

For a SUSY parameter space detectable at the level of the electroweak scale, large numbers of squarks and gluinos will be produced within the LHC environment. The final states of such particles will be currently undetected lightest supersymmetric particles (LSP) or fermions, in an R-parity conserving scenario. For mSUGRA the $\tilde{\tau}$ is predicted to be the lightest slepton, and expected to decay into τ lepton final states. With the parameter space $m_0 < m_{1/2}$ and $\tan\beta = 35$, nearly 80% of all events at the LHC are expected to contain at least one τ lepton [29].

The decay chains of squarks and gluinos are mediated by neutralinos which for moderate to high $\tan\beta$ will have a decay largely dominated by τ leptons. Such a possible decay chain is shown in the Feynman diagram of Figure 2.6 [30]. One of the primary sources of this decay chain will be from a gluino decay, $\tilde{g} \to b\tilde{b} \to bb\tilde{\mathcal{X}}_2^0 \to bb\tau\tilde{\tau} \to bb\tau\tau\tilde{\mathcal{X}}_1^0$, and while searches using τ leptons in early data will be difficult, such searches will prove to be important over time.

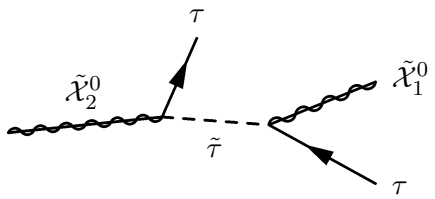

Figure 2.6: Decay chain of a neutralino to τ^- lepton and $\tilde{\tau}$ followed by a τ^+ lepton and another neutralino. Such a decay chain could occur in a gluino decay chain.

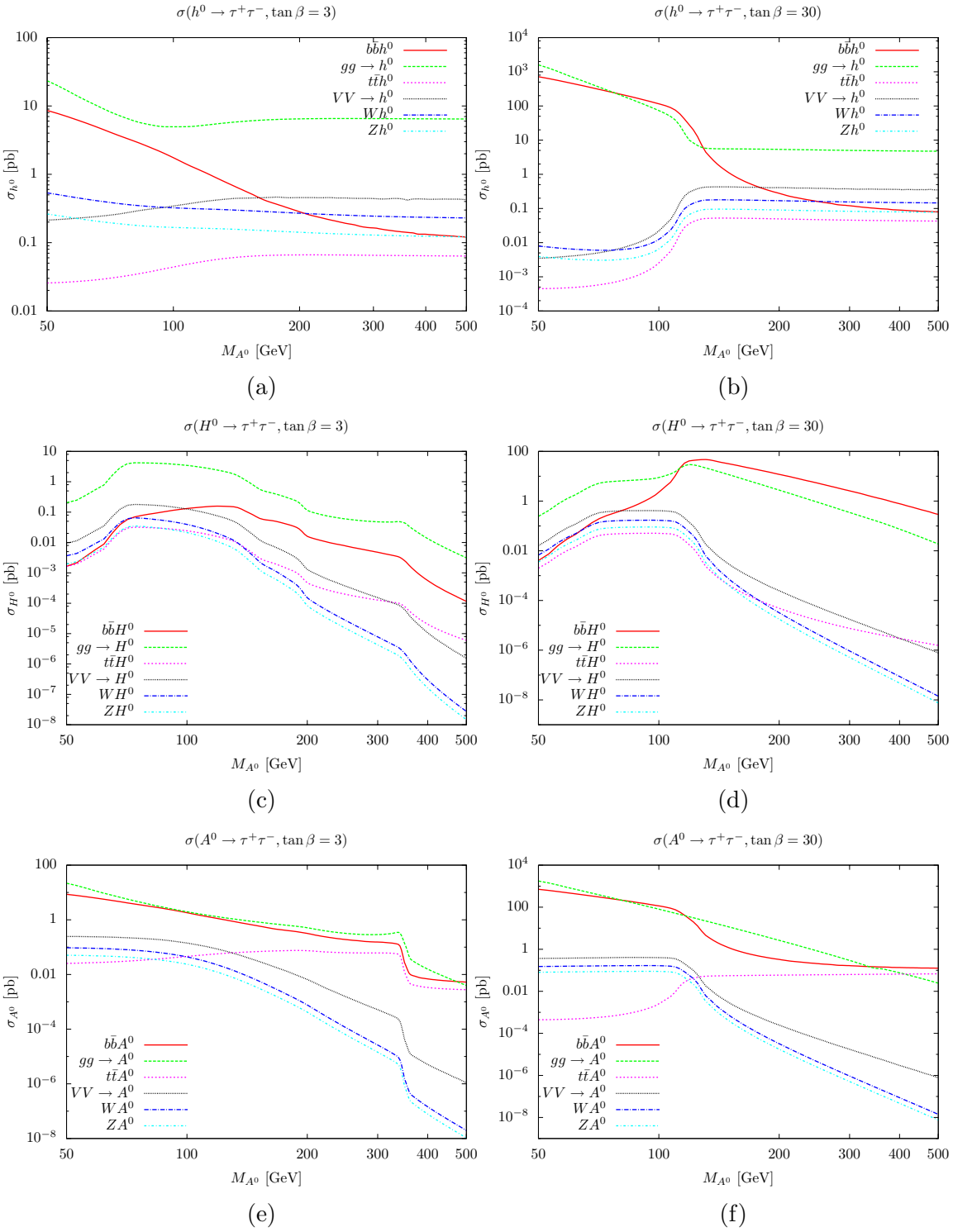

Figure 2.7: Theoretical MSSM Higgs cross sections with a $\tau^+\tau^-$ final state for h^0 (upper), H^0 (middle), and A^0 (lower) at $\tan\beta = 3$ (left) and $\tan\beta = 30$ (right). The production processes are given by Figure 2.3 where gg fusion includes next to leading order gq and qq not shown in Figure 2.3. Note that $H^\pm$ is not included as it is not produced by the mechanisms of Figure 2.3. Further details on the production of the plots are given in Appendix D.

3 Experiment

To further explore the Standard Model, it is necessary to develop more advanced detectors and colliders. While LEP has excluded the existence of a Higgs boson up to masses of ≈ 115 GeV, the search is far from over, and further experiments are required. Even neglecting the search for the Higgs, higher energies are necessary to further understanding of the Standard Model through new physics. A world wide collaboration of scientists and engineers at CERN is providing such an opportunity to investigate the Standard Model through the LHC and its subsequent detectors.

3.1 Large Hadron Collider

The LHC is a proton-proton collider located in Geneva, Switzerland at CERN. Shown in Figure 3.1, the LHC is 27 km in circumference with a 14 TeV center-of-mass energy. The accelerator supports two multipurpose detectors, ATLAS and CMS, along with a dedicated heavy ion detector ALICE, and LHC-b, designed specifically for the detection of hadrons containing bottom quarks. Two additional detectors, TOTEM and LHCf, share facilities with ATLAS and CMS. The LHCf is located in the same cavern as the ATLAS detector and is designed to explore the forward regions of proton-proton interactions not covered by ATLAS. TOTEM shares a cavern with CMS and measures total cross sections, elastic scattering, and diffraction dissociation.

The LHC itself is an extraordinarily complex machine and the result of decades of planning. The following is not intended as a full technical description of the machine, but rather a brief overview of the underlying concepts important to this paper. As for any particle physics experiment, the luminosity of the accelerator is critical to the design and discovery potential of the associated detectors. The injector chain also plays a critical role in the operation time of the accelerator, and determines the total integrated luminosity for a specified time period. Finally, the collider layout determines the beam parameters necessary to calculate the luminosity, and provides a general impression of the physical design of the detector. A full review can be found in Reference [31].

3.1.1 Luminosity

The rate of events generated, R_{event}, for a specific process with cross section σ_{event} and instantaneous beam luminosity $\mathscr{L}$ is given in Equation 3.1.

$$R_{\text{event}} = \mathscr{L}\sigma_{\text{event}} \tag{3.1}$$

As many of the processes being searched for at the LHC have low cross sections, it is necessary for the LHC beam to have a high luminosity to provide a detectable number of events.

$$\mathscr{L} = F\left(\frac{n_p^2 n_b f \gamma_{\text{r}}}{4\pi\epsilon\beta^*}\right) \tag{3.2}$$

The luminosity, as given in Equation 3.2 [31], is dependent upon the collision frequency f, the number of particles colliding in each beam n_p, the number of bunches n_b, the relativistic factor

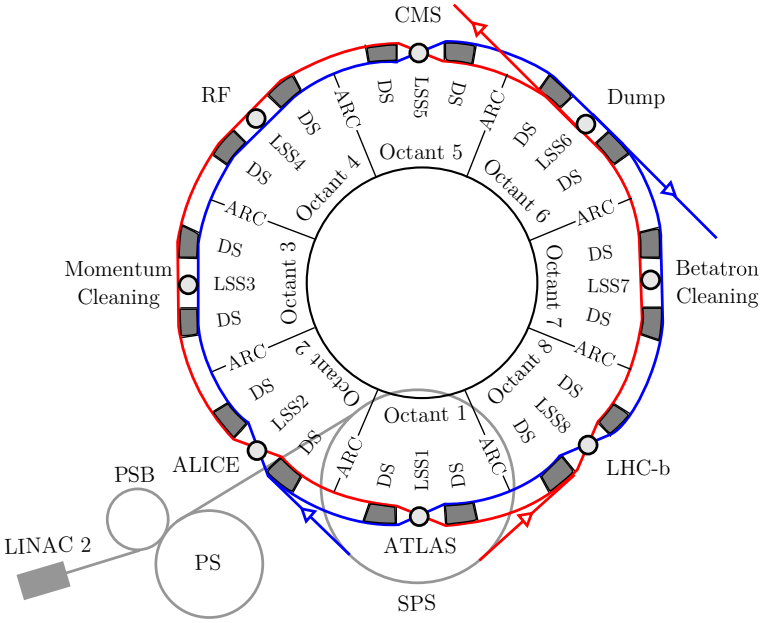

Figure 3.1: Schematic of the LHC including the injection chain and layout of the collider. Beam 1 is shown in blue and circulates clockwise, as seen from above. Beam 2 is in red and circulates counter-clockwise. Four beam crossings are depicted at Points 1, 2, 5, and 8. Beam 1 is injected at Point 2 while Beam 2 is injected at Point 8.

γ_r of the beam, a geometric reduction factor F, the normalized transverse emmitance function ϵ_n, and the transverse betatron function at the interaction point, β^*. The geometric reduction factor is given in Equation 3.3.

$$F = \left[1 + \left(\frac{\theta_c \sigma_z}{2\sigma^*}\right)^2\right]^{-1/2} \tag{3.3}$$

The beam is assumed to have a Gaussian shape with a known width at the interaction point, σ^*, and length, σ_z, determined by the preparation of the beam. The angle θ_c is the full beam crossing angle and is determined from the geometry of each interaction point.

The transverse beam emmitance is defined as the maximum amplitude of an average particle within a bunch. Equation 3.4 defines the beam emmitance in terms of the betatron function and transverse beam size. The normalized transverse beam emmitance is $\epsilon_n \gamma_\mathrm{r} \beta_\mathrm{r}$ where β_r is the relativistic β factor of the beam.

$$\epsilon \equiv \frac{\sigma(s)^2}{\beta(s)} \tag{3.4}$$

The betatron is a periodic function with respect to position s within the collider ring and dependent upon the the placement and strength of the LHC quadrapole magnets, fully determined by the lattice arrangement of the LHC [32].

The parameters of Equations 3.2 and 3.3 for the LHC at Point 1 where the ATLAS detector is located are given in Table 3.1 for a goal peak luminosity of $\mathscr{L} \approx 10^{34}\ \mathrm{cm}^{-2} \cdot \mathrm{s}^{-1}$. Limits on the parameters place this luminosity as a maximum. The number of bunches and frequency of the accelerator are dictated by a necessary bunch spacing of 25 ns due to the time resolution of

Beam Parameters	Value	Point 1 Parameters	Value
n_p	1.5×10^{11} particles	ϵ_n	3.75 μm
n_b	2808 bunches	σ^*	16.7 μm
f	21.4 Hz	β^*	74.4 μm
γ	7461	θ_c	142.5 °
σ_z	7.55 μm		

Table 3.1: Relevant parameters of Equations 3.2 and 3.3 for an LHC operation of $\mathscr{L} \approx 10^{34}$ cm$^{-2} \cdot$ s^{-1} at Point 1 [31].

the LHC detectors. From the geometry of the LHC beam screens, a maximum transverse beam emittance of $\epsilon = 3.75$ μm is allowed. The sum of the linear tune shift over all interaction points, defined in Equation 3.5, should not exceed 0.015 as determined by previous experiments. Here, m_p is the mass of the proton.

$$\xi \equiv \frac{n_p e^2}{16\pi^2 c^2 m_p \epsilon_0 \epsilon_n} \tag{3.5}$$

With three experiments requiring head on proton collisions (ATLAS, CMS, and LHC-b), the linear tune shift must remain below 0.005. As the transverse beam emmitance is already limited by the beam screen, this requires the number of protons per bunch to be less than 1.15×10^{11}.

The relativistic factors γ_r and β_r are both limited by the energy of the beam, which is subsequently limited by the maximum attainable strength of the dipole magnetic field of 8.33 T. Restrictions on beam dump capacity also limit the energy of the beams. The final parameters, beam width and length, are limited by the timing and accuracy of the magnetic fields.

Due to beam collisions, elastic scattering, and Touschek scattering, beam luminosity lifetime is limited. If the beam vacuum is well maintained, elastic scattering is minimized, but both beam collisions and Touschek scattering remain. Touschek scattering occurs if protons within the beam collide and produce a longitudinal momenta outside the limits of the accelerator [33]. Taking all effects into account, the beam luminosity mean lifetime is estimated to be $\tau_\mathscr{L} \approx 14.9$ hours [31].

3.1.2 Injector Chain

The injection chain is shown in Figure 3.1 and is a critical aspect in the integrated beam luminosity of the LHC. Beams begin within an Alvarez linear accelerator (LINAC 2). Here a duoplasmatron creates a plasma from a highly ionized gas. The plasma is accelerated into a proton beam and fed through a 750 keV radio frequency quadrapole into three Alvarez tanks. The protons are accelerated to an energy of 50 MeV, frequency of 0.8 Hz, and maximum pulse length of 150 μs and fed to the Proton Synchrotron Booster (PSB) [34].

The PSB was first built in 1968 and has since been upgraded through various projects to meet the needs of the current experiments at CERN. Four rings with a radius of 25 m are filled from the LINAC 2 by means of an electrostatic deflector with each ring holding one bunch. After the beams are simultaneously accelerated to 1.4 GeV they are recombined and ejected to the Proton Synchrotron (PS) by kicker magnets [35].

Two batches from the PSB are required to fill the PS in a scheme designed to maintain sufficient brightness of the beam. The beam within the PS is designed to hold 84 bunches with

a bunch spacing of 25 ns. The beam is accelerated to 26 GeV where an 80 MHz cavity reduces the bunch lengths to 4 ns such that they can fit within the 200 MHz RF cavities of the Super Proton Synchrotron (SPS). The bunches are kicked into the SPS with 3 bunches lost due to kicker magnet rise times [36].

The SPS with a radius of 1.1 km accelerates the beam from an energy of 26 GeV to 450 GeV using two RF cavities operated at a frequency of 200 MHz. The beam is then fed into the main LHC ring at Point 2 or Point 8 as shown in Figure 3.1 [37]. The beam traveling in a clockwise direction, as viewed from above, enters at Point 2, while the beam traveling in the counterclockwise direction is inserted at Point 8.

The main LHC ring requires 12 cycles from the SPS to fill completely. Each SPS fill takes 21.6 seconds and requires 4 cycles of 3.6 seconds each from the PS. An additional 4 SPS cycles are assumed for an initial setup, with a 2 minute calibration period between each injection cycle. This brings the total injection time to approximately 16 minutes for the complete filling of both beams for the LHC. An additional 60 minutes is required to ramp the beam energies from 450 GeV to the full energy of 7 TeV for each beam. A planned system check of 10 minutes brings the complete injection cycle to approximately 86 minutes under ideal conditions.

The optimal run time t_{run} is given by Equation 3.6 where $\tau_{\mathscr{L}}$ is the luminosity lifetime and t_{turn} is the average turnaround for each injection cycle.

$$t_{\text{run}} = \tau_{\mathscr{L}} \ln\left(\frac{t_{\text{run}} + t_{\text{turn}}}{\tau_{\mathscr{L}}} + 1\right) \tag{3.6}$$

Using $\tau_{\mathscr{L}} \approx 894$ minutes as previously mentioned in Section 3.1.1, and $t_{\text{turn}} \approx 86$ minutes yields an optimal run time of $t_{\text{run}} \approx 366$ minutes.

Integrating the instantaneous luminosity of the accelerator over the run time is given by Equation 3.7. Plugging the optimal run time obtained from Equation 3.6 and the optimal instantaneous luminosity from Section 3.1.1 into Equation 3.7, the integrated luminosity for one run is found to be 1.5×10^{31} cm$^{-2} \cdot$ s^{-1}.

$$\mathscr{L}_{\text{run}} = \mathscr{L}\tau_{\mathscr{L}}\left(1 - e^{-t/\tau_{\mathscr{L}}}\right) \tag{3.7}$$

Assuming the LHC is constantly operated 200 days out of the year, the maximum integrated luminosity for a year is given by Equation 3.8.

$$\mathscr{L}_{\text{year}} = \frac{(200)(24)(60)}{t_{\text{run}} + t_{\text{turn}}}\mathscr{L}_{\text{run}} \tag{3.8}$$

Using the previously calculated values for t_{run} and t_{turn} a value of $\mathscr{L}_{\text{year}} \approx 69$ fb^{-1} is found [31].

3.1.3 Collider Layout

The collider ring contains three types of sections, long straight sections (LSS), arcs, and dispersion suppressors (DS). Figure 3.1 diagrams the locations of each section type within the collider ring. The ring is divided into octants, and contains eight arcs alternated with eight long straight sections. Each long straight section provides an access point to the surface, with the ability of additional infrastructure to be added at each access point.

Point 1, corresponding to LSS1 in Figure 3.1, houses the ATLAS experiment, while Point 5 houses the CMS experiment. Both interaction regions contain identical hardware. However, the crossing angle at Point 1 is perpendicular to the surface, and the crossing angle at Point 5 is horizontal. On either side of the interaction point a free space of 23 m is maintained, dictating

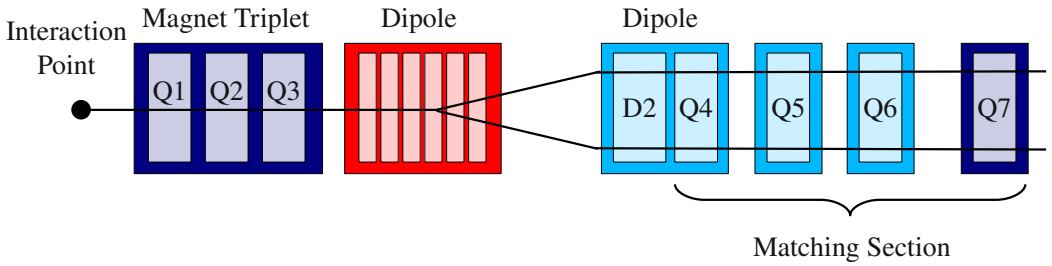

Figure 3.2: Simplified half schematic of the magnet layout of LSS1 and LSS5 surrounding the ATLAS and CMS detectors. Dark blue indicates a cryostat kept at 1.9 K, light blue a cryostat maintained at 4.5 K, and red a warm cryostat.

the maximum length of either experiment. Figure 3.2 shows a simplified schematic of the LSS's surrounding both Point 1 and Point 5.

Following along the beam line from the interaction point at Point 1 and 5 in both directions is located a 31 m triplet assembly of magnets with an operational gradient of 205 T/m. The triplet assembly is proceeded by the separation and recombination dipoles. The first dipole is a 20.4 m assembly of six warm magnet modules with operating fields of 1.38 T. The second dipole is a a single 9.4 m superconducting magnet with a field of 3.8 T. A matching section consisting of four quadrapole magnets is adjacent to the separation dipole. The first quadrapole provides a gradient of 160 T/m while the following three quadrapoles provide gradients of 200 T/m. Standard dispersion suppressor and arc sections follow the matching quadrapoles.

Point 2 houses both the ALICE experiment and the injection system for Beam 1, shown in blue of Figure 3.1. The magnet configuration is similar to that of Point 1 and 5 in layout, but the hardware parameters must fulfill the more stringent requirements necessary for the beam injection system. The injection system is inserted within the matching section left of the interaction point (as viewed from the center of the ring) from below the plane of the LHC ring. Similar constraints are placed on Point 8 which houses both the LHC-b experiment and the injection system for Beam 2, shown in red in Figure 3.1.

Points 3, 4, 6, and 7 do not contain beam crossings but house various beam monitoring and cleaning equipment. Momentum cleaning occurs in LSS3 while betatron cleaning is performed in LSS7. RF and feedback services are housed in the old ALEPH cavern of LSS4. Finally, LSS6 houses the beam abort systems for both Beam 1 and Beam 2. In the case of a beam extraction, the beams are horizontally kicked into iron septum magnets which vertically deflect the beams into separate tunnels terminated by absorbers. Each dump system must be able to dissipate over 362 MJ.

Each LSS section is followed by a dispersion suppressor responsible for adapting the orbit of the LHC beams to the geometry of the LEP tunnel. Additionally, the suppressors eliminate horizontal dispersion caused by the separation and recombination of the beam by the dipoles. Both the DS and arc cells are similar in design, with the DS cells having the dipole units of the arc cell removed. Each arc is made of 23 cells containing 6 dipoles, a short straight section, and two cold masses [31].

3.2 ATLAS Detector

The ATLAS detector is a multi-purpose detector designed to explore the wide range of known and unknown physics available at the energy scale of the LHC. The detector, shown in Figure 3.3, consists of six primary systems: the magnet system, the inner detector, the electromagnetic calorimeter, the hadronic calorimeter, the muon system, and the trigger system. All six systems are specifically designed to compliment each other in order to provide a comprehensive detector.

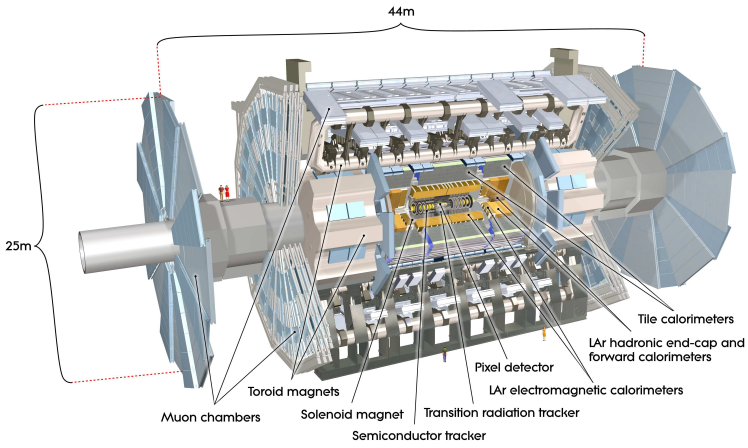

Figure 3.3: The ATLAS detector as taken from Reference [38].

Located at Point 1 on the LHC ring 100 meters below the surface, ATLAS resides in a cavern approximately 45 by 25 meters, and weighs 6.4×10^6 kg. ATLAS uses a right-handed coordinate system with the x-axis directed to the center of the LHC ring, the y-axis pointing towards the surface, and the z-axis pointing along the direction of the beam such that $\hat{x} \times \hat{y} = \hat{z}$. Furthermore, the angle ϕ, always given in radians, is defined to be an azimuthal angle perpendicular to the z-axis, such that $\phi = 0$ corresponds to the x-axis. The range of ϕ is $-\pi \leq \phi \leq +\pi$ and the angle increases in a clock-wise direction around the z-axis. The angle θ is defined to be a polar angle perpendicular to the x-axis with the z-axis corresponding to $\theta = 0$.

However, due to the highly relativistic nature of the collisions occurring within the detector, particle production is approximately constant with respect to rapidity, the quantity invariant under Lorentz boosts defined in Equation 3.9.

$$y \equiv \frac{1}{2} \ln \left(\frac{E + p_z}{E - p_z} \right) \tag{3.9}$$

Here E is the energy of a particle and p_z the longitudinal momentum along the z-axis. As energy is much greater than mass for collisions within the LHC, energy can be approximated by momentum, $E \approx |\vec{p}|$. This approximation yields pseudorapidity, as defined in Equation 3.10, which can be written in terms of the polar angle θ. Because of its near Lorentz invariant properties, pseudorapidity is often favored over θ.

$$\eta \equiv -\frac{1}{2} \ln \left(\frac{|\vec{p}| + p_z}{|\vec{p}| - p_z} \right) = -\ln \left(\tan \frac{\theta}{2} \right) \tag{3.10}$$

A pseudorapidity of $\eta = 0$ corresponds to the y-axis while a pseudorapidity of $\eta = \pm\infty$ corresponds to the $\pm z$-axis.

3.2.1 Magnet System

The magnet system, as shown in Figure 3.4 consists of a central solenoid, a barrel toroid, and two end-cap toroids. Because the central solenoid is located between the inner detector and electromagnetic calorimeter the solenoid is designed to be as thin as possible while maintaining reliability. A particle incident to the normal of the solenoid passes through approximately 0.7 radiation lengths. The solenoid is one coil with 1154 turns of a niobium-titanium (Nb-Ti) alloy with aluminum and copper added for stabilization. To maintain super-conducting properties, the coil must be kept at 4.5 K, which is achieved by a cryostat shared with the electromagnetic calorimeter. While operating at an operational current of 7.73 kA, a maximum magnetic field of 2 T is provided by the solenoid, with a field of 2.6 T achieved within the coil itself. The coil has an outer diameter of 2.6 m and a length of 5.3 m, covering a pseudorapidity range of $|\eta| < 2.7$ [39].

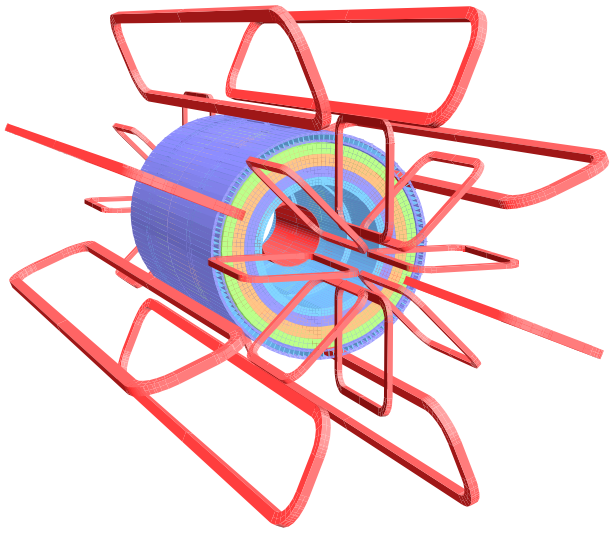

Figure 3.4: The ATLAS magnet system is shown in red with the four layers of the calorimeter. The outermost cylinder, in dark blue, is the return yolk for the central solenoid, represented by the centrally located red cylinder. The barrel toroid is shown by the six long red coils about the center of the detector, while the end-cap toroids correspond to the eight small loops on either side of the detector. Image adapted from Reference [38].

The barrel toroid is located outside the calorimeters and provides a variable magnetic field for the muon system. Eight coils of an Al/Cu/NbTi alloy, similar to the central solenoid alloy, make up the barrel toroid, with 120 turns per coil. The operating temperature of the barrel toroid is 4.5 K with a nominal current of 20.5 kA. As the barrel toroid does not provide a constant magnetic field, the bending power, as defined in Equation 3.11, is measured instead.

$$P \equiv \oint_R B_z \cdot dl \tag{3.11}$$

Here B_z is the component of the magnetic field along the z-axis, and R is a radial path in the xy-plane through the magnetic field. The barrel toroid provides a bending power of $2 - 6$ T·m and covers a pseudorapidity range of $0 \leq |\eta| \leq 1.3$. This range corresponds to a physical length of 25.3 m, with an inner diameter of 9.4 m and an outer diameter of 20.1 m [40].

The two end-cap toroids each consist of eight coils each with 116 turns of the same Al/Cu/NbTi alloy used in the barrel toroid. These coils also operate at a temperature of 4.5 K and nominal current of 20.5 kA. A bending power of $4 - 8$ T·m is provided by each end-cap and covers $1.6 \leq |\eta| \leq 2.7$ in each hemisphere of the detector. The length of the coils for each end-cap is 5 m while the outer diameter is 10.7 m and the inner diameter is 1.65 m [41].

The entire magnet system is supported with a vacuum and cryogenic system controlled by a complex electronic system. A measurement and calibration of the fields was performed in August of 2006 by a machine with 12 moveable Hall cards [42]. A full field map has been reconstructed using both theory and empirical measurements.

3.2.2 Inner Detector

The ATLAS inner detector, shown in Figure 3.5 with a detailed schematic in Figure 3.6, consists of three sub-detectors: the pixel detector, the silicon microstrip tracker (SCT), and the transition radiation tracker (TRT). Both the pixel detector and the SCT operate on the principles of a doped semiconductor. A particle passes through the silicon of the detector and creates a series of electron-hole pairs. A bias voltage is run across the silicon and the electrons created from the passing particle flow to the anode of the detector. A measured current signals that a particle has been detected.

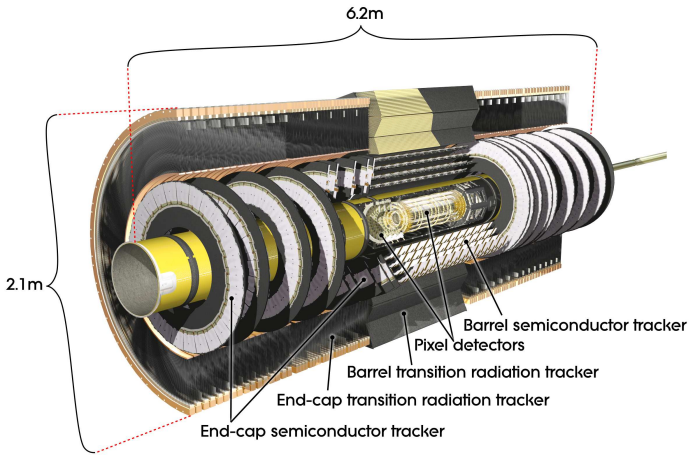

Figure 3.5: The ATLAS inner detector as taken from Reference [38].

The TRT consists of straw tubes, which differ in first principles from silicon based detectors. A straw tube consists of a long gas filled cylinder with an anode wire running down the center. As a particle passes through the cylinder the gas is ionized. The ions flow to the anode and trigger a change in current, signaling a detected particle. Additionally, as relativistic charged particles pass between material interfaces of different dielectric constants, transition radiation is produced in the direction of the particle trajectory. The additional radiation is detected by the straw tubes producing an increased current. Due to the large mass difference between electrons and hadrons, electrons with a momentum greater than 1 GeV produce transition radiation while hadrons such as pions begin to produce transition radiation only when their momentum is greater than 100 GeV. This difference allows for the separation of electrons from hadrons using the TRT.

The pixel detector barrel is composed of three layers: Layer-0 critical for vertexing located at

$r = 50.5$ mm, Layer-1 at $r = 88.5$ mm, and Layer-2 at 122.5 mm. Six end-caps are located at $\pm z = 495$, 580, and 650 mm. Layer-0 contains 13.2×10^6 pixels while Layer-1 has 22.8×10^6 pixels and Layer-2 has 31.2×10^6 pixels. Each end-cap contains 2.2×10^6 pixels bringing the total number of pixels within the pixel detector to 80.4×10^6. Each pixel has a physical size of 19×63 mm with an intrinsic accuracy σ_x of 10×115 μm [43].

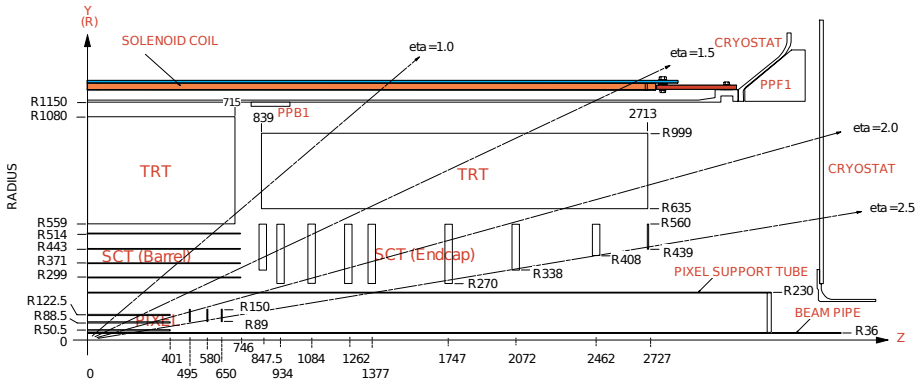

Figure 3.6: A detailed schematic of one quadrant of the ATLAS inner detector, as taken from Reference [44].

The SCT barrel consists of four layers at $r = 299$, 371, 443, and 514 mm. Each layer consists of two strips to provide a single stereo hit. A total of 18 end-caps, 9 in either hemisphere, are located at $\pm z = 847.5$, 934, 1084, 1262, 1377, 1747, 2072, 2462, and 2727 mm. The SCT contains 15912 sensors each with $\sigma_x = 17 \times 580$ μm [44].

The TRT is made up of 37 (end-cap) and 144 mm (barrel) straws manufactured from a polyimide film and filled with a $Xe/CO_2/O_2$ gaseous mixture. The electron collection time for each straw is approximately 48 ns which provides a drift time accuracy of $\sigma_x = 130$ μm with a position given only in the radial ϕ direction. The TRT spans from a radius of 544 to 1082 mm [45].

The entire inner detector covers a range of $|\eta| < 2.5$ with a required track resolution of $\sigma_{p_T}/p_T = 0.05\%\ p_T \oplus 1\%$. An average number of 43 hits for a track with $p_T > 0.5$ GeV is provided by 3 hits from the pixel detector, 4 from the SCT, and 36 from the TRT. Detailed tests of the pixel detector, SCT, and TRT at various stages of assembly were performed. After integration of the SCT with the TRT, an average of 0.23% of the channels from the SCT were found to have defects. Similarly the pixel detector was found to have an average of 0.33% channels defective. After the entire inner detector was lowered from the surface and integrated into the full ATLAS detector, the TRT was found to have an average of 1.8% of the channels defective [38].

The material budget within the inner detector is significant and leads to serious consequences. Specifically, for a particle with $|\eta| \approx 0$ a total of $0.469X_0$ is traversed within the inner detector while for a particle with $|\eta| \approx 1.8$ a total of $1.126X_0$ is traversed. These high radiation lengths result in a large number of electrons losing the majority of their energy through bremsstrahlung before entering the electromagnetic calorimeter. Nearly 40% of photons are absorbed by pair production prior to entering the electromagnetic calorimeter and a large number of charged pions undergo inelastic hadronic interaction within the inner detector [38].

3.2.3 Electromagnetic Calorimeter

The electromagnetic calorimeter, shown in light brown in Figure 3.7, consists of two half-barrels around the central region, two end-caps, one on either side of the detector, and a presampler. Charged particles pass into the calorimeter and are rapidly decelerated as they pass through the electric fields of the absorber material. As the particles decelerate through bremsstrahlung radiation, virtual photons are emitted which subsequently initiate electron-positron showers. The shower passes into the sampling portion of the calorimeter where the gas is ionized and drifts to the cathodes of the calorimeter cell producing a detected current. The electromagnetic calorimeter is able to detect photons which also initiate electron-positron showers.

The barrel calorimeters each cover one hemisphere of the detector with $0 < |\eta| < 1.475$ and are lead and liquid argon (LAr) sampling calorimeters. Argon was chosen as the active medium due to its linear behaviour, stable response time, and radiation hardness while lead was chosen as the absorber due to its high radiation length. Each barrel has an accordian geometry to ensure full coverage in ϕ, consisting of 1024 absorber plates interleaved with readout electronics. A LAr presampler is located just before the two barrels, within the barrel cryostat, and consists of an 11 mm layer of liquid argon split into 64 sectors.

Each barrel is split into three active sampling layers with varying granularities. The first sampling layer has a very fine granularity of $\Delta\eta \times \Delta\phi = 0.0031 \times 0.0982$ designed to differentiate between single photons and π^0 decays. The second sampling layer is coarser with a granularity of $\Delta\eta \times \Delta\phi = 0.025 \times 0.0245$ and absorbs most of the energy from particle showers. The third sampling layer absorbs the remainder of the energy from the particle showers and has a granularity of $\Delta\eta \times \Delta\phi = 0.050 \times 0.0245$ [46].

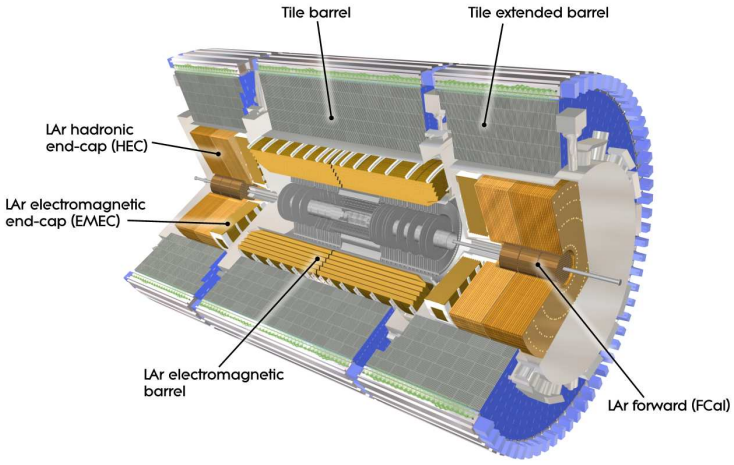

Figure 3.7: The ATLAS calorimeters as taken from Reference [38].

The end-caps of the electromagnetic calorimeter are also lead-LAr sampling calorimeters with an accordian design similar to the barrel calorimeters. Each end-cap covers a region of $1.375 < |\eta| < 3.2$ and provides a thicknes of greater than $24X_0$. However, as the end-caps are composed of two co-axial wheels, a coverage gap of 3 mm does exist at $|\eta| = 2.5$. A LAr presampler, similar to the barrel presampler, is located just before the end-caps [38].

In 2006 a section of the barrel calorimeter was subjected to the CERN H8 electron test beam to determine the energy resolution and response properties of the calorimeter. Test data

was fit to Equation 3.12 and the constants were found to be $a = 10.1 \pm 0.1\% \cdot \sqrt{\text{GeV}}$ and $b = 0.17 \pm 0.04\%$. Both the stochastic and sampling terms were found to be in agreement with Monte Carlo simulations of the calorimeter resolution [47].

$$\frac{\sigma_E}{E} = \frac{a}{\sqrt{E}} \oplus b \tag{3.12}$$

After the calorimeter was inserted into the full detector and cooled to operational temperatures, a full test of all calorimeter readout channels was performed. For the barrel presampler no defective channels were found, while for the remaining barrel calorimeter only 24 defective channels were found out of 109952 channels, with a fault rate well below the required 0.05% [48]. A similar test was performed on the end-cap calorimeters with 1 of 1536 channels found to be defective for the presampler and 15 of 68160 channels for the end-caps [49].

3.2.4 Hadronic Calorimeter

The hadronic calorimeter, highlighted in grey and dark brown in Figure 3.7, has three components, a tile calorimeter, a LAr end-cap calorimeter, and a LAr forward calorimeter. Both LAr components work on the same principles as the electromagnetic LAr calorimeter. The tile calorimeter also utilizes a similar principle of measuring electron-positron showers, but rather than ionizing a gas, a scintillator is luminesced by the shower. Photomultiplier tubes are struck by the photons from the scintillator and produce a current that signals a detected particle shower.

The tile calorimeter is located behind the electromagnetic barrel calorimeter and covers a pseudorapidity of $|\eta| < 1.7$. A steel absorber is used, rather than lead, as the steel not only acts as an absorber but also provides the structural support for the tile calorimeter. The scintillator tiles are 3 mm thick and range in widths of 97 to 187 mm and 200 to 400 mm. The scintillating material used is polystyrene which produces ultraviolet light. Fluors of polystyrene doped with PTP and POPOP elongate the wavelength of the scintillated light before passing the light to wavelength shifting collection fibers placed at the edges of the tiles. The wavelength shifting fibers again increase the wavelength before passing the light to the photomultiplier tubes where the photonic signal is converted to an electric signal [50].

Just as the electromagnetic barrel calorimeter, the tile calorimeter barrel has three active sampling layers. Each sampling layer has a time resolution of approximately 1 ns necessary for the expected high luminosity of the LHC. The first two sampling layers have a granularity of $\Delta\eta \times \Delta\phi = 0.1 \times 0.1$ while the final layer has a granularity of $\Delta\eta \times \Delta\phi = 0.2 \times 0.1$ [51].

The hadronic end-cap calorimeter (HEC), uses a copper absorber and steel support frame along with the sampling liquid argon. Each end-cap contains two wheels, and covers $1.5 < |\eta| < 3.2$. The forward calorimeters (FCal) provide a coverage of $3.1 < |\eta| < 4.9$. As the FCal is very close to the beamline, high particle flux is expected, and smaller gaps filled with liquid argon are used to increase the response time of the system [38].

In 1996 portions of the electromagnetic LAr calorimeter and the hadronic tile calorimeter were exposed to the CERN H8 test beam. The combined energy resolution for hadronic processes was estimated to be $a = 52.0 \pm 1.0\% \cdot \sqrt{\text{GeV}}$ and $b = 3.0 \pm 0.1\%$ using Equation 3.12 [52].

3.2.5 Muon System

The muon system, shown in Figure 3.8 contains four primary components: monitored drift tubes (MDT), cathode strip chambers (CSC), resistive plate chambers (RPC), and thin gap chambers (TGC). The system is designed to provide high transverse momentum resolution of

approximately 10% for muons with a p_T of 1 TeV with a spacial resolution of 50μm while maintaining a fast triggering system.

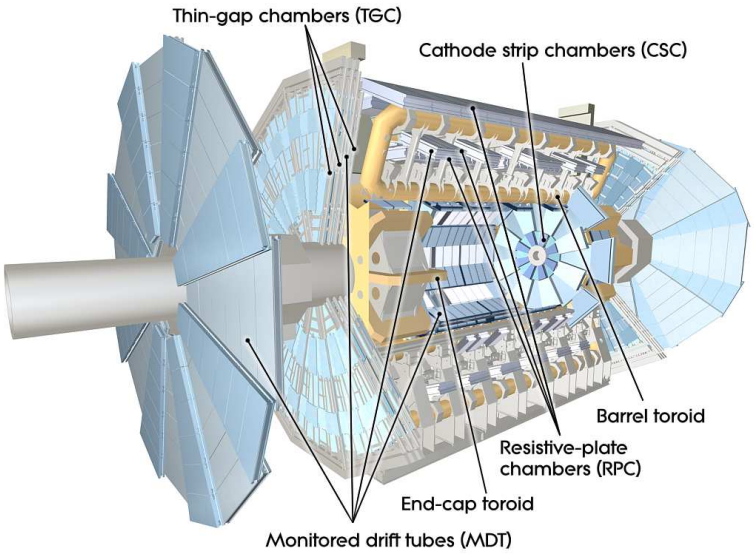

Figure 3.8: The ATLAS muon as taken from Reference [38].

The MDT's operate in a similar fashion as the TRT. A narrow cylindar is filled with gas, and a wire is passed down the center of the tube. A high voltage is applied between the shell of the tube and the central wire. As a muon passes through the tube the gas within is ionized, and if the particle is energetic enough, an ionization cascade is initiated, producing a current on the anode. Calibration of drift times within tube allow for precise position measurement of the ionizing particles.

The CSC system is made of multiwire proportional chambers, similar to the MDT's on first principle, but is constructed from flat chambers with multiple anode wires, rather than one anode wire per tube. A series of cathode strips are layed perpindicular to the anodes, allowing for full position determination, with additional position verification information from pulse timing. The TGC system is the same as the CSC system, but the spacing of the anodes within the chambers is smaller, providing better time resolution for triggering.

An RPC consists of two charged plates, with a gaseous layer seperating the plates. The electric field within the chamber is maintained to trigger a cascade after an initial gas atom is ionized by a passing charged particle. While such a system does not provide precise position location, the fast response time and excellent time resolution of the chamber is favorable for triggering operations.

The MDT's are located centrally around the hadronic calorimeter, but also in wheels in the forward regions of the detector for a coverage of $|\eta| < 2.7$. Used for tracking, the MDT system contains 1088 chambers with 339000 output channels. In both the end-cap and barrel 20 measurements are performed per track with a resolution of 35 μm in the z-direction for the barrel and the radial direction for the end-caps. The tubes are made of aluminum with a diameter of 30 mm and a wall thickness of 0.4 mm. The anode wires have diameters of 50 μm and are manufactured from rhenium and tungsten with a gold plating. Each tube is filled with a gas mixture of $Ar/CO_2/H_2O$ and maintained at a pressure of 3 bar [53].

For occupancy rates that exceed 150 Hz/cm^2, corresponding to an $|\eta| > 2$ the MDT's timing

resolution is no longer adequate, and the CSC system must be used in conjuction with the MDT system. Two end-cap wheels are used, covering a range of $2 < |\eta| < 2.7$. The chambers contain an $ArCO_2$ gas mixture with an anode and cathode spacing of 2.5 mm [54].

Both the RPC and TGC system are designed specifically to provide muon triggering for the full detector. Both systems are able to quickly provide an estimation of momentum and energy information for passing muons. The RPC system is present around the central barrel of the detector in three concentric layers. The layers are positioned in such a manner as to provide a low trigger of $6 < p_T < 9$ GeV from the seperation between the first two layers, and a high trigger of $9 < p_T < 35$ GeV from the seperation between the first and third layers. The chambers provide a seperation of 2 mm filled with $C_2H_2F_4/\text{Iso}{-}C_4H_{10}/SF_6$ and provide an electric field of 4.9 kV/mm. The RPC system has a 1.5 ns response time with 544 chambers and 359000 output channels [38].

The TGC system is located in the forward region of the detector in two end-cap wheels and provides muon triggering for the higher pseudorapidity range of $1.05 < |\eta| < 2.4$. The system contains 3588 chambers with 318000 channels with a response time of 4 ns. The individual chambers are similar to the CSC system but use smaller anode and cathod spacing along with a gas mixture of CO_2/n−pentane.

3.2.6 Trigger and Data Acquisition

Due to the high luminosity of the LHC as previously discussed in Section 3.1, a high event rate on the order of 1 GHz is expected. Selecting relevant data from this high rate requires a trigger and data acquisition system that is not only fast but also extremely efficient. While data acquisition and the trigger are seperate systems, both are dependent upon each other and are therefore presented together.

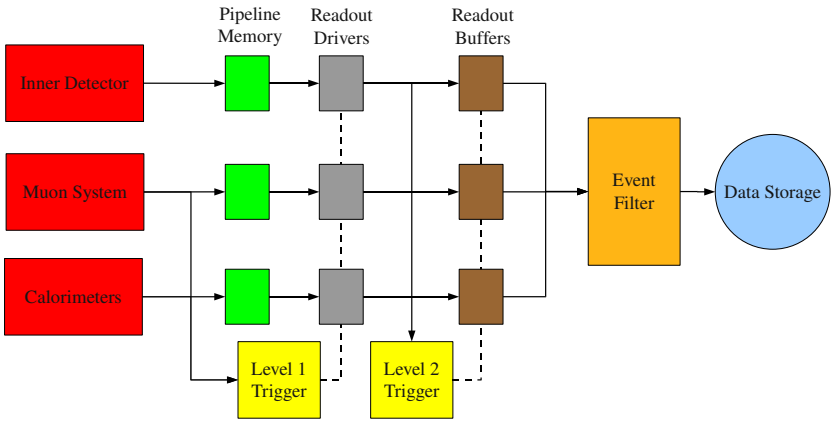

Figure 3.9: A simplified diagram of the ATLAS trigger and data aquisition system.

Figure 3.9 shows a simplified flow-chart of data movement through the ATLAS trigger and data acquisition systems. Information is read directly from the detector systems into pipeline memory. Here reduced granularity data from the RPC, TGC, and full calorimeter systems is passed to the level one trigger (L1) where searches for regions of interest containing high E_T objects and large amounts of $\not{E}_T$ are performed. While the L1 is making a selection, the full data from the detectors is held within the pipeline memory. If an event passes the L1 trigger decision, the full data is passed from pipeline memomory to the readout drivers where it is then

read by the level two trigger (L2) at a rate of no more than 75 kHz.

The L2 trigger and Event Filter (EF) are both fully implemented with software on commercially available hardware unlike the custom hardware of the L1 trigger. The L2 trigger is seeded by regions of interest passed from the L1 trigger while relevant data is held within the readout buffers. However, the L2 trigger uses full granularity from all detectors along with inner detector information within the regions of interest passed from the L1 trigger. This full granularity allows for more precise locations of the regions of interest. After passing the L2 selection, data is sent at a rate of 3.5 kHz to the EF. The EF further reduces the rate of data flow to 200 Hz and passes the data to be written to data storage. After data is stored it is made available to the ATLAS community through the GRID for offline analysis [38].

4 Tau Lepton Reconstruction

The reconstruction of hadronic τ leptons is challenging, but can be accomplished by taking advantage of the unique kinematic properties of the hadronic τ lepton decay products. As discussed earlier in Section 2.2.1, the products of a hadronic decay are primarily charged and neutral pions, a signal very similar to jets created within generic QCD events. However, hadronic τ leptons decay through the W boson, as depicted in Figure 2.2, and subsequently provide a clean signal with no surrounding tracks. QCD jets are produced through strong interactions and produce busy events with high track multiplicity. Additionally, the hadronic τ leptons of interest in Higgs searches are produced from significantly more massive particles, m_Z (91 GeV) $\gg$ m_τ (1.8 GeV), and so the produced τ leptons are highly boosted. These two points provide the key kinematics of hadronic τ leptons: highly collimated and isolated jets. The following sections will outline how these two kinematic properties can be utilized, both within the official ATLAS reconstruction algorithms, and proposed modifications to the current algorithms.

4.1 ATLAS Reconstruction

ATLAS τ lepton reconstruction is performed both on the trigger level and during offline reconstruction. While reconstruction on the trigger level is not necessary, as hadronic τ leptons can be reconstructed from offline events triggered on for example a single lepton, such a reconstruction allows for more robust triggering and an increase in efficiency for events where hadronic τ leptons could be reconstructed in offline analysis.

4.1.1 Trigger

In the past many detectors have had no dedicated hadronic τ lepton trigger as the ability to quickly perform the necessary algorithms was not available. However, with increases in computing and hardware technology, ATLAS is able to implement a hadronic τ lepton trigger.

The ATLAS trigger system, as described in Section 3.2.6 consists of a hardware based level one trigger (L1), and a software based high level trigger broken into a level two trigger (L2) and event filter (EF). The L1 hadronic τ lepton trigger begins within the cluster processor modules by assessing trigger towers of size $\Delta\eta \times \Delta\phi = 0.1 \times 0.1$ from the EM calorimeter with $|\eta| < 2.5$.

The E_T of all four towers within a 2×2 selected core, based on a local energy maxima, are summed horizontally in pairs of 1×2 and vertically in pairs of 2×1. The maximum E_T sum is required to pass an energy cut, specified by the various available trigger menus. Additionally, the entire E_T of the 2×2 core within the region of interest, along with the corresponding 2×2 hadronic towers, must also pass an E_T minimum. This process, depicted in Figure 4.1, ensures that the identified jet is highly collimated, as is expected from a hadronic τ lepton decay.

Following the selection of a 2×2 core within the region of interest that meets the specific requirements described above, an isolation requirement is imposed, also shown in Figure 4.1. Here, the surrounding 4×4 trigger tower region in both the EM and hadronic calorimeter is summed. Each sum must then pass a programmable maximum. If all the requirements for the region of interest are met, the event is passed onto the L2 trigger for further analysis [55].

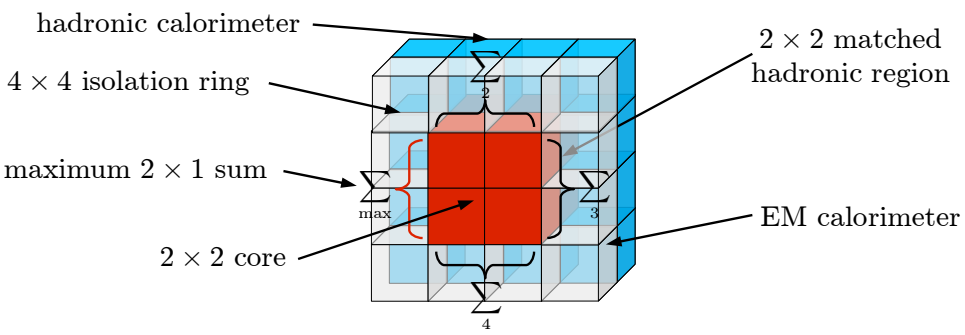

Figure 4.1: Diagram of a region of interest from the L1 ATLAS hadronic τ lepton trigger.

The L2 trigger begins by refining the location passed from the L1 trigger using the second layer of the EM calorimeter. After the region of interest location has been pinpointed, the EM radius, defined in Equation 4.1 is calculated from calorimeter cell information and must fall below a programmable maximum.

$$\text{EM radius} = \frac{\sum_{\text{cells}} E_i \Delta R_i^2}{\sum_{\text{cells}} E_j} \tag{4.1}$$

Here, the energy of each calorimeter cell within the 6×6 calorimeter towers surrounding the region of interest is multiplied by the ΔR of that cell, where ΔR is defined in Equation 4.2.

$$\Delta R \equiv \sqrt{\Delta\phi^2 + \Delta\eta^2} \tag{4.2}$$

This quantity is then divided by the sum of the energy of the cells. The final calorimetry step of the L2 trigger is the summation of the E_T within the region of interest for both calorimeters [56].

Next the L2 trigger considers inner detector information from the SCT and pixel detectors. Tracks within an area of $\Delta\eta \times \Delta\phi = 0.6 \times 0.6$ around the calorimeter region of interest are reconstructed, using a fast track finding algorithm specific to the L2 trigger. The tracks are sorted by p_T and the track with the highest p_T is chosen as the signal track. A signal cone in $\eta - \phi$ space of $\Delta R_{\text{S}} = 0.15$ is drawn around the signal track and an isolation cone with $\Delta R_{\text{I}} = 0.3$ is drawn around the signal cone as depicted in Figure 4.2.

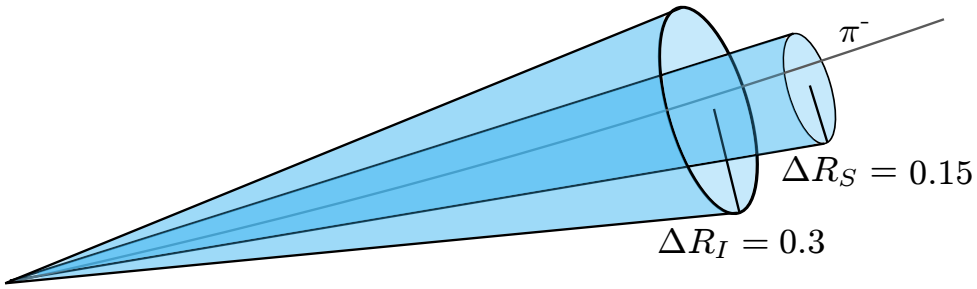

Figure 4.2: Cones drawn in $\eta - \phi$ space around the leading p_T track found within a $\Delta\eta \times \Delta\phi = 0.6 \times 0.6$ area about the L2 trigger region of interest for a hadronic τ lepton decay into a π^- with the τ neutrino not shown.

From these cones four selection variables are defined. First, a minimum p_T cut is made on the leading track p_T. Next, the p_T sum of all tracks within the signal code is divided by the p_T sum of all tracks within the isolation cone but not within the signal cone. A minimum cut is performed on this variable, ensuring isolation of the signal tracks. The final two variables used are the total charge of tracks within the isolation and signal cones along with the total number of tracks in the isolation and signal cones. The total number of tracks in the isolation and signal cones are used as the number of incorrectly reconstructed tracks by the L2 track reconstruction is relatively high, and implementing a strict cut on a single variable would significantly decrease efficiency [56]. After an event passes both calorimeter and inner detector cuts from the L2 trigger, it is passed on to the EF.

The EF uses offline reconstruction methods for both the calorimeter and the tracker, but does so only in a $\Delta\eta \times \Delta\phi = 0.8 \times 0.8$ area around the region of interest passed from the L2 trigger. A topological jet is formed within the calorimeters and the energy is calibrated to ensure a quality E_T measurement. The EM radius of Equation 4.1 is calculated, but with the quantity ΔR_i rather than ΔR_i^2. Tracks are associated with the topological jet, and required to meet certain p_T requirements determined by the trigger menu. Final cuts are made on the invariant mass of the reconstructed tracks associated with the τ lepton, the EM radius, the calibrated E_T, and the number of tracks in the case of a multi prong decay. If an event passes, it is passed to data acquisition for storage.

A variety of trigger menus are available in association with a single hadronic τ lepton trigger, as described above, and can be applied for specific physics processes. The following trigger combinations are currently available with the ATLAS trigger menus [56]. For each trigger combination an example is given for a specific physics process which could be selected by the trigger. These examples are not intended to be inclusive, but merely provide a possible usage scenario for the trigger.

- $\tau_h + \not{E}_T$: For $W \rightarrow \tau\nu_\tau$ searches a hadronic τ lepton trigger is combined with a $\not{E}_T$ requirement corresponding to the missing energy of the τ neutrino.

- $\tau_h + \ell$: A hadronic τ lepton trigger in conjunction with a single lepton is used for physics processes creating τ lepton pairs where one τ lepton decays hadronically and the other leptonically. These events correspond to many of the Higgs signals described in Section 2.2.2.

- $\tau_h + \tau_h$: This combination will trigger on the same processes as the $\tau_h + \ell$ combination but looks for a final state where both τ leptons decay hadronically.

- $\tau_h +$ jets : A hadronic τ lepton trigger plus associated jets provides an alternative trigger for t quark pair production through the strong interaction. The t quark decays nearly entirely into a W boson and a b quark. The b quark provides the jets to the signal, while the W decay provides the hadronic τ lepton jet.

A maximum of eight regions of interest may be selected by the L1 trigger and carried through to the EF. This requirement is made to keep the time in which each trigger executes at a minimum. This is necessary to account for the 25 ns bunch crossings expected during nominal LHC operation. Simulations performed in Reference [56] place the current total performance of the L2 hadronic τ lepton trigger at $8 - 10$ ms per event depending on the filtering thresholds used. The EF hadronic τ lepton trigger was found to be $25 - 68$ ms, also depending upon the filtering thresholds. The study was performed on QCD background events with the generated events in the transverse momentum range of $35 < p_T < 70$. The efficiencies for the combined

L1, L2, and EF triggers vary greatly depending on the threshold cuts chosen, but can range anywhere from an estimated 40% to 80% for $W \rightarrow \tau_h \nu_\tau$ and $Z \rightarrow \tau_h^+ \tau_h^-$ signals. Whether such efficiencies can be maintained under actual detector conditions including pile-up and multiple interactions remains to be seen.

4.1.2 Offline

The offline reconstruction of hadronic τ leptons is very similar to that of the EF reconstruction, but is now performed with full detector information over the entirety of the event. Currently, ATLAS uses a merged scheme between track seeded and calorimeter seeded reconstruction.

The track seeded algorithm begins by choosing the highest p_T track within the event. This track must have $p_T > 6$ GeV with a maximum χ^2 over number of degrees of freedom such that $\chi^2/NDOF < 1.7$. Additional requirements are placed on the number of hits within the SCT and TRT. A signal cone of $\Delta R_S = 0.2$ is drawn around the leading track, and any additional tracks with $p_T > 1$ GeV which fall within this cone are considered to be part of τ lepton.

The number of tracks that fall within the the signal must be of multiplicity one or three, corresponding to the one or three prong hadronic decays of the τ lepton described in Section 2.2.1. Any calorimeter clusters which fall within the signal cone radius are added to the τ lepton object. The η and ϕ of the object are defined by the line tangent to the perigee of the track, if only one track is found. If the decay is three pronged, the direction of the object is defined by the center of mass of the system of tracks.

The calorimeter seeded algorithm searches for jets within the calorimeter with $E_T > 10$ GeV. A cone of $\Delta R = 0.4$ is drawn around the center of the jet and and the energy of the surrounding cells are calibrated. Track association is performed by matching tracks of $p_T > 1$ GeV with the calorimeter hit within a cone of $\Delta R = 0.3$.

The merged tracker and calorimeter seeded algorithm combines both methods. The seeding for the algorithm begins with tracks, but for each seed track a calorimeter jet candidate is searched for within a cone of $\Delta R = 0.2$. If a jet candidate is found, the candidate is taken as a jet seed and the tracker and calorimeter algorithms are run simultaneously. The position and all track variables of the candidate are defined by the tracker seeded algorithm while the energy of the object is defined by the calorimeter seeded algorithm. Notice that no isolation requirements are made during offline reconstruction.

In the case of no calorimeter seed, the track algorithm constitutes the entirety of the τ lepton candidate. After all tracker seeds are exhausted, the remaining jets within the calorimeter that have not been associated with τ lepton candidates have the calorimeter seeded algorithm run on them. This merged method provides traditional track based seeding while also utilizing the fine granularity of the ATLAS calorimeters [57].

4.2 Proposed Reconstruction

While the current ATLAS algorithms provide adequate results for hadronic τ lepton reconstruction, various improvements can be made by studying the underlying kinematics of both a signal and a background. This section proposes modifying current techniques by parameterizing cone shapes with respect to relevant variables. First the signal and background used for the study are introduced, then studies of both the signal and isolation cone are shown, and finally a track based reconstruction algorithm is proposed.

4.2.1 Signal and Background

The signal used for this study is $Z \rightarrow \tau^+\tau^-$ as depicted in the left Feynman diagram of Figure 4.3. Here a quark from one of the incoming protons annihilates with a sea quark, creating a Z boson which subsequently decays into two τ leptons. This specific signal was chosen as the production of a τ lepton pair is similar to the signals generated by the SM Higgs and MSSM Higgs bosons. While the mass of the Z boson is below the masses of the particles being searched for, the mass is high enough to provide kinematics similar to the Higgs processes. This signal is a standard candle for high energy particle physics, and τ lepton identification and reconstruction can be tuned specifically with early data involving these events. Such tuning will prepare the τ lepton algorithms for identification and discovery of new physics.

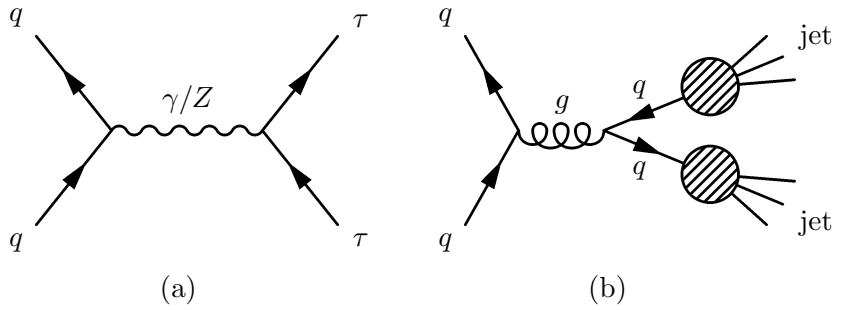

Figure 4.3: Signal (a) and background (b) used in studies. The background is meant only to demonstrate the possible formation of a QCD dijet event.

The background used is a QCD dijet sample. This provides two or more jets formed through QCD with a kinematic end product similar to that of the signal sample. Figure 4.3 also shows a possible background event with the exchange of a W causing a flavor change between quarks and triggering a hadronization process that produces two jets.

The background sample was generated using Pythia 6.418 and the signal was generated using MC@NLO 3.1 while both samples were reconstructed with ATLAS reconstruction software Athena version 14.2.21 with further details given in Appendix A. The center of mass energy for the proton proton collision was set at 10 TeV as this is the expected collision energy of the LHC in 2009 and 2010.

4.2.2 Signal Cone

Nearly 70% of hadronic τ lepton decays are one prong, while only 30% are three prong decays. These decays imply that for nearly 70% of reconstructed hadronic τ leptons, the shape or size of the signal cone does not affect the track based reconstruction efficiency, assuming the lead track is well isolated within the signal cone. However, for both backgrounds and three prong hadronic decays, the signal cone has a significant effect. Placing a tight restriction on the signal cone eliminates background, but also eliminates three prong signal. Conversely, a loose signal cone will increase the three prong signal but also increase the background. Subsequently, an ideal signal cone must take into account the kinematic shape and possible parameterizations of the three prong decays.

Before parameterizations for the three prong decays can be analyzed, the general kinematic shape of the decay must be taken into account to provide the best possible signal cone shape.

From the physics of the hadronic τ lepton decay as discussed in Section 2.2.1, it is expected that the three prong hadronic τ lepton decay products should be distributed symmetrically around the axis of the τ lepton and an elliptical cone should fit the distribution well. Within a detector environment two natural coordinate systems for the cone can be defined: $\eta - \phi$ space and $\theta - \phi$ space. The radius in $\eta - \phi$ space is given by ΔR defined by Equation 4.2. Similarly, in $\theta - \phi$ space the radius can be given by an absolute opening angle α as defined in Equation 4.3.

$$\alpha \equiv \cos^{-1}(\cos\phi \cos\theta) \tag{4.3}$$

To determine the coordinate space in which the signal cone should be defined, the kinematics of generator level information were explored. All generator level τ leptons with hadronic decays were selected, and the final hadronic stable particles of the τ lepton were found. The momentum four vector for the τ lepton, excluding all neutrino decay products, was then calculated. All hadronic τ leptons with a visible transverse momentum below 6 GeV were discarded, as the current ATLAS reconstruction requires a $p_T > 6$ GeV for a seed track. Of the remaining τ leptons, all with three or five prong decays were accepted, while the one prong decays were removed. Each remaining visible τ lepton was assigned an η bin: $|\eta| < 0.5$, $0.5 \leq |\eta| < 1.5$, or $1.5 \leq |\eta| < 2.5$. Within each bin the angle between the stable, charged decay products, with $p_T > 1$ GeV and the center of the visible mother τ lepton, were found for $\Delta\eta$, $\Delta\theta$, and $\Delta\phi$. The results are shown in the top plot of Figure 4.4.

As can be seen, the decay product distribution of the one or three prong hadronic τ leptons remains constant in $\eta-\phi$ space for all η, while it collapses in $\theta-\phi$ space for high η. This behavior can be understood from the underlying physics, as the higher η range will be dominated by τ leptons from highly boosted Z bosons. This boosting causes the decay products of the τ lepton to also be boosted. Rapidity is invariant under Lorentz boosts, and so the τ decay distribution should remain approximately constant in $\Delta\eta$ for most particles.

A similar plot for the QCD background can also be seen in Figure 4.4. Here, stable generator level particles with $p_T > 1$ GeV and a charge of ± 1 were matched against generator level jets constructed using the standard ATLAS jet reconstruction algorithm applied to generator level information. The matching was performed with a cone of $\Delta R = 0.7$ as this is the standard cone size for ATLAS jet reconstruction. The background was taken from four independent samples binned by p_T as explained in Appendix A. The four samples were normalized with respect to cross section and combined to produce the background plot of Figure 4.4. The resulting distribution, as expected, is also constant in $\eta - \phi$ space, while it collapses in $\theta - \phi$ space. However, it can be seen that the jets from the QCD background are much less collimated than the hadronic τ lepton jets.

It is only natural, from Figure 4.4, to choose the definition of the signal cone to be in $\eta - \phi$ space with a radius of ΔR. With this definition for the signal cone set, it is now possible to proceed with the parameterization of the signal cone. For τ leptons with large amounts of transverse energy, it is expected that the collimation of the decay products would be greater due to the subsequent Lorentz boost of the products. This leads to a natural parameterization of the signal cone radius: the higher the E_T of the τ lepton, the tighter the radius of the signal cone.

Figure 4.5 demonstrates the dependence of the hadronic τ lepton opening angle with respect to the energy of the τ lepton. Here, all generator level τ leptons with a three or five prong decay and $p_T > 6$ GeV were found along with their subsequent charged stable decay products with $p_T > 1$ GeV. The ΔR between the decay product and the center of the visible generated τ lepton was found and plotted against the E_T of the visible generator level τ. A similar plot was made for the QCD dijet background, with all generator level jets with a $p_T > 6$ GeV being selected.

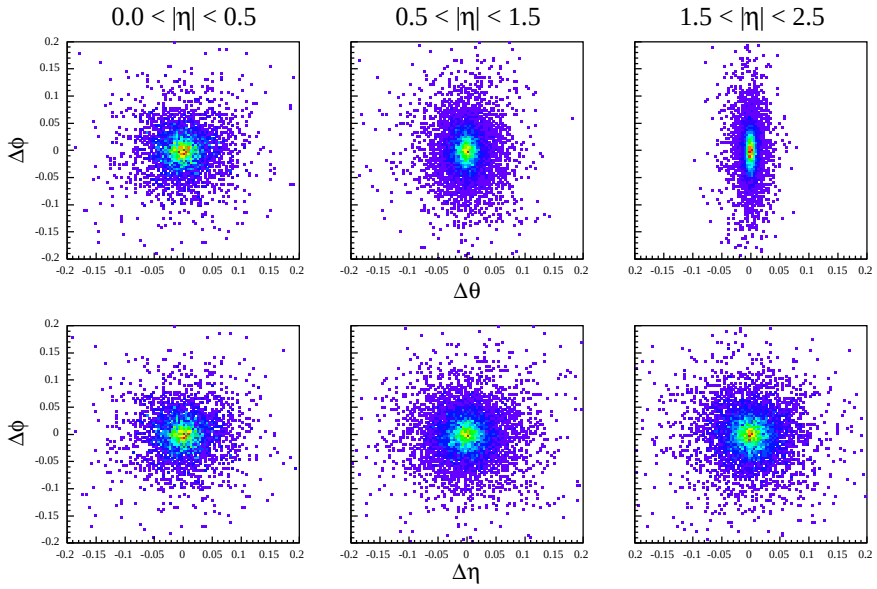

(a)

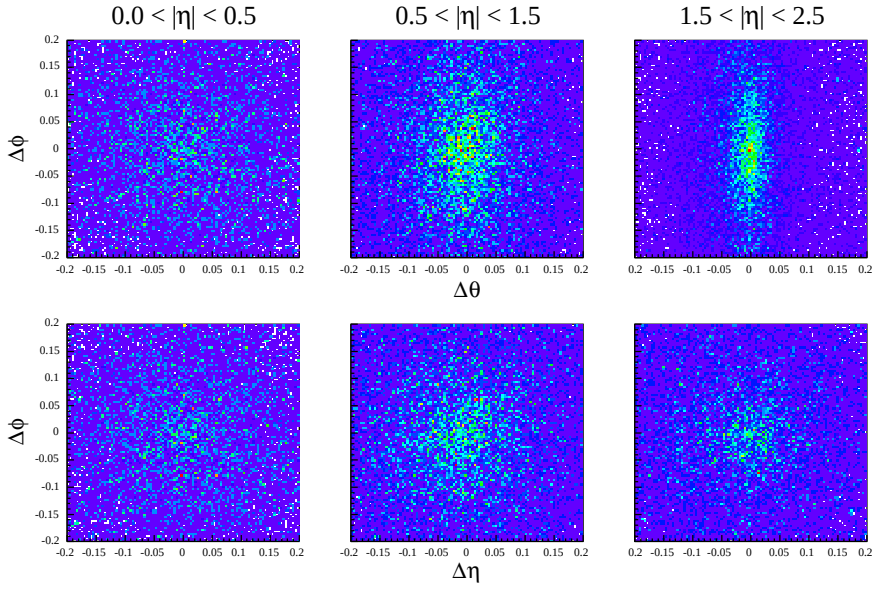

(b)

Figure 4.4: The charged decay product distribution of three and five prong hadronic τ leptons is shown in (a). Plot (b) provides the same distribution but for the decay products of jets from the QCD dijet background sample. The scale for both (a) and (b) is relative with red representing high and purple representing low. Both plots were made using generator level information.

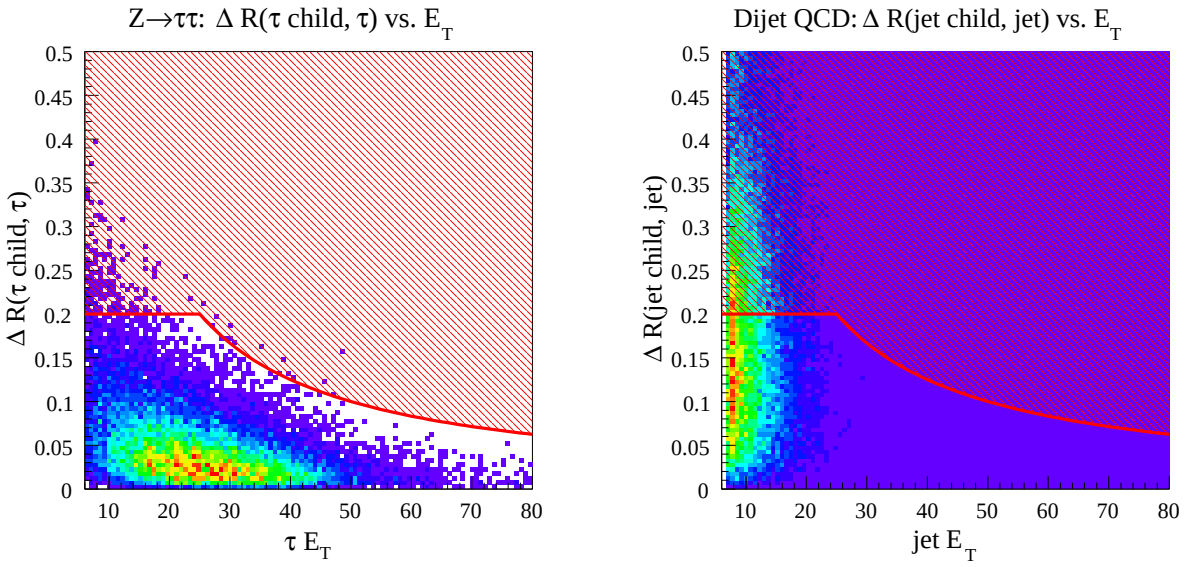

(a) (b)

Figure 4.5: The opening angles for three and five prong hadronic τ leptons versus transverse energy of the generated τ lepton is shown in (a). Plot (b) provides the same distribution but for the decay products of jets from the QCD dijet background sample. Both plots were made using generator level information.

The opening angle in ΔR for each stable generator level particle within a cone of $\Delta R = 0.7$, $p_T > 1$ GeV, and a charge of ± 1, was plotted versus the transverse energy of the generator level jet.

The signal and background plots of Figure 4.5 differ significantly, implying that a signal cone opening angle parameterized with respect to the E_T of the τ lepton could provide a method to differentiate the signal and background. A clear correlation exists between the E_T of the visible τ lepton and the opening angle of the decay products in ΔR. The same correlation in the QCD dijet example is not as pronounced, with the distribution remaining nearly vertical with respect to the energy of the jet. This can also be explained from the underlying physics, as the jets from the QCD events are not decaying from a massive Z, and should in general not be as boosted as the τ leptons.

The parameterization chosen for the signal cone is given in Equation 4.4 and shown by the red exclusion region in Figure 4.5. A maximum opening angle of $\Delta R_S = 0.2$ is allowed, matching the current ATLAS reconstruction signal cone. However, for τ leptons with higher transverse energy, the cone is defined as $\Delta R_S = 5/E_T$ where E_T is given in GeV. The intersection of $\Delta R_S = 0.2$ and $\Delta R_S = 5/E_T$ occurs at $E_T = 25$ GeV. Such a definition for the signal cone has also been proposed for CMS in References [1] and [58] and also for CDF in Reference [59].

$$\Delta R_S \equiv \min(0.2, 5/E_T) \tag{4.4}$$

4.2.3 Isolation Cone

The isolation cone, unlike the signal cone, is relevant to both one, three, and five prong decays of hadronic τ leptons, as all τ leptons should have a similar isolation. However, finding an

isolation requirement that maintains efficiency while rejecting background is challenging and highly dependent upon the signal sample and background processes. For a $Z \rightarrow \tau\tau$ signal sample, it would be expected that the τ leptons should be relatively well isolated, as the majority of the energy in the event should be in the production of the Z boson. Note that the isolation cone is considered part of the reconstruction process on the trigger level, but in offline analysis the isolation cone is used during identification.

Just as for the signal cone, a coordinate space must be chosen to define the shape of the isolation cone. To determine the shape and coordinate space, it is again necessary to look at generator level information, but now also include reconstruction level information as track reconstruction is critical to isolation. Figure 4.6 shows the track distributions surrounding both a hadronic τ lepton and a QCD jet. For the signal distribution, hadronic τ leptons were found at generator level and their visible energy was calculated. Hadronic τ leptons with $p_T > 6$ GeV were separated into the same η bins as were used for Figure 4.4. Every track from reconstruction level with charge ± 1 and $p_T > 1$ GeV that did not fall within a signal cone of $\Delta R_S = 0.2$ was plotted against the visible center of the hadronic τ in $\Delta\phi$, $\Delta\eta$, and $\Delta\theta$. Positive $\Delta\eta$ and $\Delta\theta$ have been defined to be towards the beamline, as the track distribution is expected to be symmetric around the z-axis of the detector.

A similar method is used for the background plot in Figure 4.6. Generator level jets with $p_T > 6$ GeV are again separated into η bins and the opening angle between the center of the jet and reconstructed tracks is plotted. All reconstructed tracks must have a charge of ± 1 and $p_T > 1$ GeV. Any track which falls within the standard ATLAS signal cone of $\Delta R_S = 0.2$ is excluded from the plot. Again, the background was taken from four independent samples binned by p_T but were combined and normalized according to cross section.

The distinct cut-offs in both the signal and background plots of Figure 4.6 emerge from the maximum allowable $|\eta|$ of 2.5 for a track as constrained by the fiducial region of the inner detector. In the $1.5 \leq |\eta| < 2.5$ bin of both plots the maximum $\Delta\eta$ is given by the maximum track η less the minimum η of the bin, or 1 in this case. The number of tracks slowly tapers as the number of hits available within the TRT diminishes with respect to higher η as can be seen in Figure 3.6. A similar effect occurs in the $\Delta\theta$ plot, this time with the maximum $\Delta\theta$ being given by,

$$\Delta\theta_{\max} = 2\left(\tan^{-1} e^{-1.5} - \tan^{-1} e^{-2.5}\right) \tag{4.5}$$

which is ≈ 0.27. Such a cut-off was not seen in the plots of Figure 4.4 as the range for $\Delta\eta$ and $\Delta\theta$ was only from -0.2 to 0.2.

An interesting pattern emerges in Figure 4.6. First, it is apparent that regarding the track distribution in $\eta - \phi$ space rather than $\theta - \phi$ space is more natural. In the middle bin of the signal plot, a high density of tracks can be seen just to the left (away from the beamline) of the actual τ lepton. The same increase in density is also seen to the left of the τ lepton in the final bin. Upon closer inspection of the first bin of the signal, a similar density can also be seen, but this time to the right of the τ lepton. In all three cases the increased density is coplanar with the τ lepton.

Looking at the underlying physics, this behavior is understandable. The tracks being generated that spoil the isolation cone are from the underlying creation process of the Z, a proton proton collision, and as such, should be correlated. For the low η regions, the Z should have very little energy, allowing the remaining energy of the event to be channeled to the remaining processes within the collision. For higher Z energies, corresponding to higher η, less energy is available to the processes that contribute the isolation spoiling tracks. This explains why for low η the density is more boosted, and to the right of the τ lepton, while for high η the τ lepton is more boosted and the increase of spoiling tracks appears to the left.

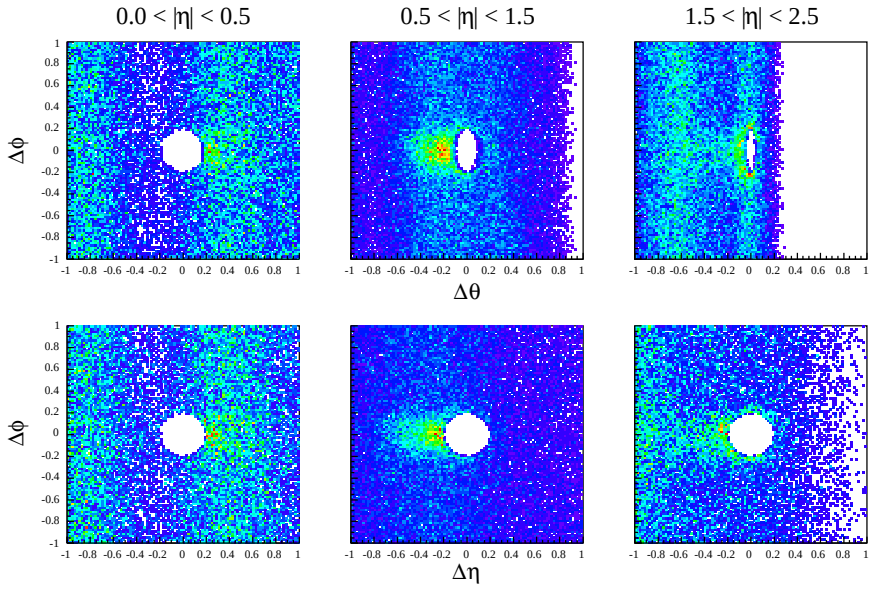

(a)

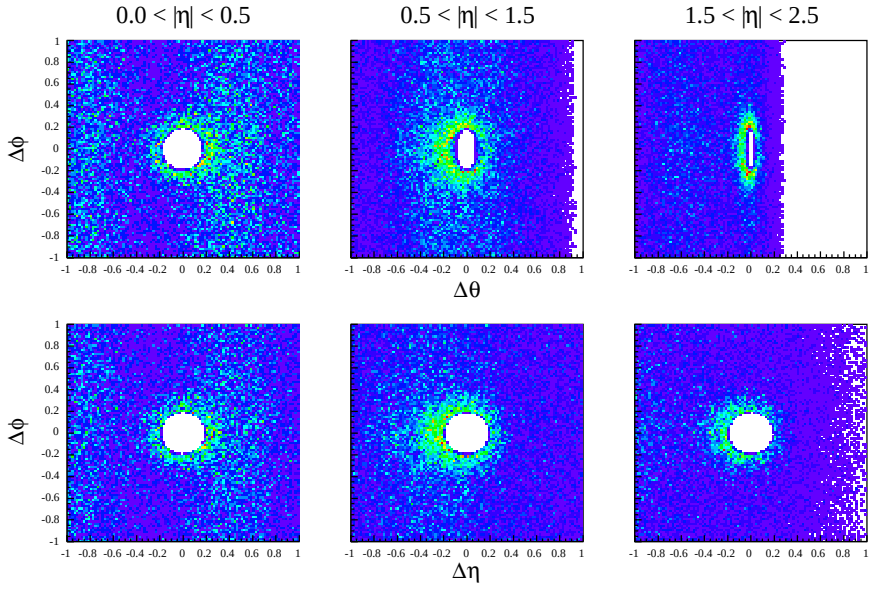

(b)

Figure 4.6: The spoiling isolation track distribution about hadronic τ leptons is shown in (a). Plot (b) provides the same distribution but for spoiling tracks associated with jets from the QCD dijet background sample.

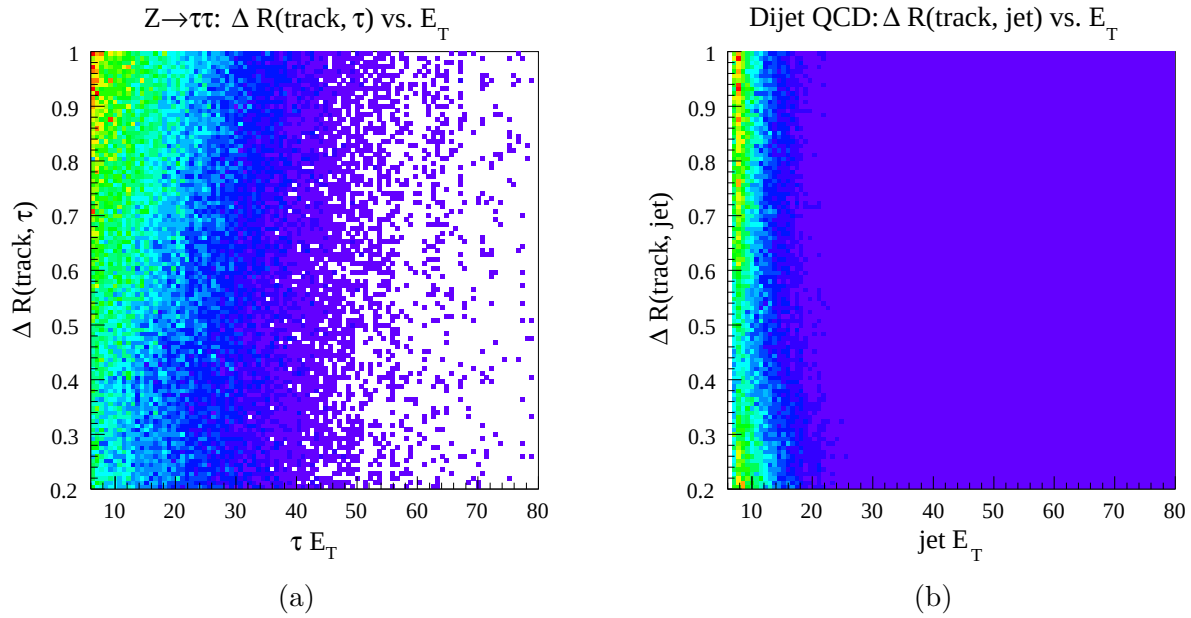

(a) (b)

Figure 4.7: The opening angle distribution between isolation cone spoiling tracks and generator level hadronic τ leptons is given in (a). The same distribution but for the QCD background is given in (b).

The same patterns do not emerge in the background plot of Figure 4.6. The distribution of the spoiling tracks is no longer coplanar, but rather circular around the center of the jet as can be best seen in the middle bin of the background plot. A slight increase in the density to the left of the center of the jet is visible in the middle bin, but in not as pronounced a manner as for the τ leptons. In all three bins the circular distribution around the center of the jet remains, providing a significant difference to the spoiling track distribution of the signal.

Just as for the signal cone, it is important to determine if the isolation cone can be parameterized with respect to variables of the τ lepton. Again the choice of E_T is the only natural choice, as the energy should be driving the kinematics of the event. Figure 4.7 provides plots of the opening angle in ΔR for the spoiling tracks with respect to the energy of the generator level τ lepton or jet.

For the signal plot all generator level hadronically decaying τ leptons with $p_T > 6$ were considered. The opening angle in ΔR with reconstructed tracks of $p_T > 1$ GeV were plotted with respect to the visible energy of the generator level τ. All tracks that fell within a signal cone of $\Delta R_S = 0.2$ were discarded. For the background plot, all generator level jets with $p_T > 6$ GeV were used. Reconstructed tracks not falling with the signal cone were plotted if their $p_T > 1$ GeV.

Unfortunately, the results of Figure 4.7 do not show a strong correlation between energy of the τ lepton or jet, and the spoiling track separation. Such a parameterization cannot be used to effectively separate signal from background. From this it is clear that there is a lack of correlation between the energy of the τ lepton or jet, and the underlying spoiling tracks. The energy of the τ lepton should significantly effect its decay products, but should have much less effect on the remaining processes occurring within the event.

This leaves only the shape of the track distributions of Figure 4.6 by which to decide the size

and shape of the isolation cone. The shape of the isolation cone can theoretically be completely arbitrary, and based on whatever shape provides the best efficiency and fake rate. However, practical limitations require that the shape can be calculated quickly and easily. Overly complex isolation cones make maintainability of the analysis software difficult and cut into valuable CPU time. As such, it would seem the simplest method for defining a cone that will utilize the previous observations regarding the track distributions is an ellipse in $\eta - \phi$ space with a center moveable along the η axis. Such a moveable center along the ϕ axis is unnecessary, as the distributions are symmetric about ϕ.

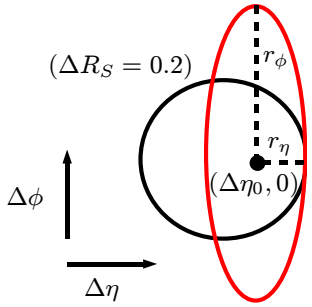

$$\left(\frac{\Delta\eta - \Delta\eta_0}{r_\eta}\right)^2 + \left(\frac{\Delta\phi}{r_\phi}\right)^2 = 1 \tag{4.6}$$

Figure 4.8: Definition of the proposed isolation cone with accompanying figure.

Figure 4.8 with Equation 4.6 define the proposed isolation cone with the three parameters $\Delta\eta_0$, r_η, and r_ϕ. These three parameters are free parameters decided by the parameter space which provides the best efficiency and fake rate. Such an optimization is signal specific; τ leptons from W decays will not have a similar signature, but as the signatures for new physics in the Higgs sector should be very similar to the Z decay, such a specific parameterization should be safe. This parameterization should not be used for general searches involving τ leptons. For such searches, a new parameterization should be obtained using relevant signal and background samples.

The parameter $\Delta\eta_0$ defines the center of the ellipse with respect to the center of the τ lepton object being reconstructed. This parameter allows for the asymmetry in the track distribution in η, as discussed earlier, to be accounted for. The parameter r_η defines the radius of the ellipse along the $\Delta\eta$ direction while the parameter r_ϕ defines the radius of the ellipse along the $\Delta\phi$ direction. Both of these parameters allow the isolation cone to take advantage of the coplanarity of the τ lepton events. All three parameters are dependent upon the η of the signal cone around which the isolation cone is being drawn. This follows from the change in the track distributions with respect to the η binning in Figure 4.6.

Ideally the parameters $\Delta\eta_0$, r_η, and r_ϕ are optimized with respect to the efficiency and fake rates of the selected signal and background respectively. However, the parameter space is defined by three variables, each potentially dependent upon η. This translates to a very large parameter space that is difficult to optimize over. Such an optimization procedure would be very time consuming, and is not within the scope of this thesis, so an alternative method by which the optimization can be approximated is taken.

Distributions for spoiling track opening angle with respect to generator level τ leptons or jets were created for η bins of size 0.5 from $\eta = 0$ to $\eta = 2.4$ with 20 overlapping bins. The range of each distribution was from -1 to 1 for both $\Delta\eta$ and $\Delta\phi$ with 100 steps in both ranges for a total of $100,000$ entries in each distribution. An optimization function f is defined as,

$$f \equiv \frac{N^S_{\text{tracks}}}{N^B_{\text{tracks}}} \tag{4.7}$$

where N^S_{tracks} is the number of spoiling tracks found within an isolation cone defined for a specific parameter set. Similarly, N^B_{tracks} is the number of spoiling tracks found within the background for the specified isolation cone. This function was chosen as it provided a relatively stable output of the minimization function and should be directly correlated with efficiency and fake rates. Other optimization functions were tested, but none yielded satisfactorily stable results.

The minimization problem to be solved is technically an unbounded optimization problem in a space of dimension three. However, from a practical viewpoint, boundings should be placed on the parameter space, as exceptionally large or small isolation cones will lead to unreasonable efficiencies not useable in a physics analysis. To impose boundings upon the function, a value of 10^{10} was returned for unnatural values. A minimum value for r_η and r_ϕ was set to 0.21 as this avoids binning ambiguities about the signal cone. Additionally, the parameter $\Delta\eta_0$ was required to remain within the signal cone, $|\Delta\eta_0| < 0.1$. This restriction ensures that the isolation cone will not be divorced from the signal cone. No upper limit was set on r_η and r_ϕ as the maximum value of the distributions is 1.

A variety of numerical methods are available for such a problem including conjugate gradient and simplex algorithms. Neither of these methods are ideal to the situation, as the function involved is neither continuous, nor necessarily convex. Due to the statistics involved, a conjugate gradient method would construct a very discontinuous gradient which would severely limit the stability and convergence of the algorithm. The simplex method is more robust for discontinuous functions such as f and provides a more stable algorithm for the problem at hand. Theoretically, the simplex method has only been shown to be convergent for convex functions of two parameters or less [60]. However, in general the algorithm has found to perform well for multidimensional problems with non-convex functions when a reasonable starting parameter space is given.

The optimization method used is the Nelder-Meade simplex algorithm outlined in Reference [61] and implemented in Reference [62]. A variety of initial parameter spaces were tried, to ensure that the algorithm was not catching on a local minima without finding the global minima for the system. As the binning and coordinate grid used were coarse, the ability of the algorithm to find a global minima was highly dependent upon the initial parameter space. Initial guesses on the parameter space showed that $\Delta\eta_0$ was a stable parameter for the system with changes of less then 0.001, indicating that creating an offset of the isolation cone does not provide a noticeable gain in the reconstruction method. The results for the most stable initial parameter space of $\Delta\eta_0 = 0$, $r_\eta = 0.3$, and $r_\phi = 0.3$ is shown in Figure 4.9.

The parameter r_η remains near the minimum allowable value of 0.21 for nearly all η. However, for $\eta > 1.75$ the optimal size of the radius in η increases. This behavior can be understood by again examining the $1.5 < |\eta| < 2.5$ bin of Figure 4.6 for the $\eta - \phi$ distributions. Within the signal sample it can be seen that a higher density of tracks is above and below the signal cone in $\Delta\phi$ than in the previous two η bins.

A similar pattern in agreement with Figure 4.6 for r_ϕ also emerges. For low η the optimal radius begins at ≈ 0.33 and slowly increases to ≈ 0.36 at $\eta = 1.55$. A sharp spike of ≈ 0.42 occurs at $\eta = 1.65$. After the spike, the optimal values of r_η remain near ≈ 0.33 again and diminish to ≈ 0.31 for the final η bin of 2.15. This drop in the radius corresponds to the increase of the η radius and the increase of the track distributions in ϕ above and below the signal cone for the signal sample.

The optimal parameters given by Figure 4.6 show that there is a dependence on η for the optimal isolation cone. However, due to the general instability of the optimizing algorithm for the input datasets, parameterizing with respect to η would involve more guess work than actual scientific rigor. For this reason, a general set of base parameters for the isolation cone definition of Equation 4.6 should be given without an η dependence.

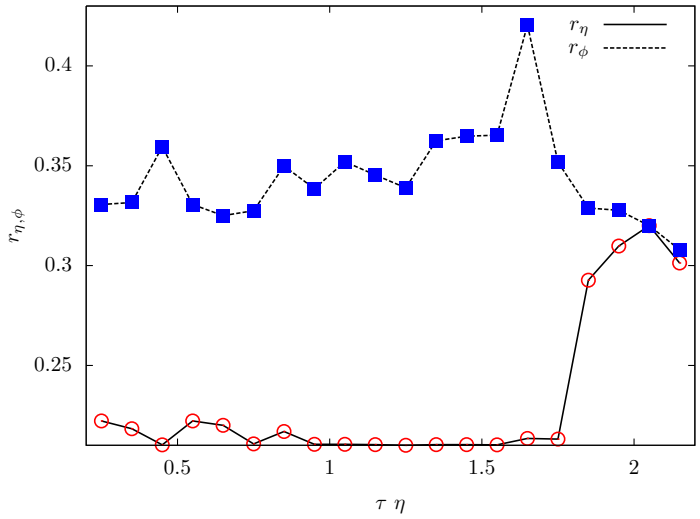

Figure 4.9: Results of optimizing the isolation cone parameters of Equation 4.6 and Figure 4.8 using the Nelder-Meade simplex algorithm with an initial parameter space of $\Delta\eta_0 = 0$, $r_\eta = 0.3$, and $r_\phi = 0.3$ and the optimizing function of Equation 4.7. The parameter $\Delta\eta_0$ is not shown as the deviation is less than 0.001 from its initial value.

Keeping this in mind the position parameter $\Delta\eta_0$ is set to zero, and removed from the definition of the isolation cone. The radius in η is best kept near 0.21 while the radius in ϕ is set near 0.34. Figure 4.10 shows the relation of the isolation cone defined by these parameters on the spoiling track distributions of the signal and background for the $0.5 < |\eta| < 1.5$ bin of Figure 4.6. These values are only set as a basis for which further exploration can be performed, and a variety of these parameters will be examined in Section 4.3.

4.2.4 Algorithm

The proposed algorithm is similar to the official ATLAS reconstruction algorithms, but uses the modified signal and isolation cones of Sections 4.2.2 and 4.2.3. All tracks within the event are sorted from highest p_T to lowest p_T into an available track list. All tracks with $p_T < 1$ GeV are discarded from the track list. The highest p_T track is chosen from the active track list as a possible τ seed candidate, and removed from the available track list. A signal cone with a radius determined by Equation 4.4, where E_T is given by the track, is drawn around the seed. The highest p_T track from the available track list that falls within the signal cone has its momentum four vector added to the momentum four vector of the seed track and is removed from the available track list. The signal cone, now using the added four vectors, is drawn again. This process, searching for the highest p_T track within the signal cone, removing the track from the available list, adding the four vectors, and recalculating the signal cone, continues until no more tracks are available within the signal cone. During this process the charge of the object being constructed and number of composite tracks is stored.

When the iterative process of combining tracks to the first seed track terminates, the process continues with the next highest p_T track in the available track list acting as the seed. The same process as before is implemented until no more tracks can be found within the signal cone. This process continues, seeding possible τ lepton objects from the available track list. If no tracks

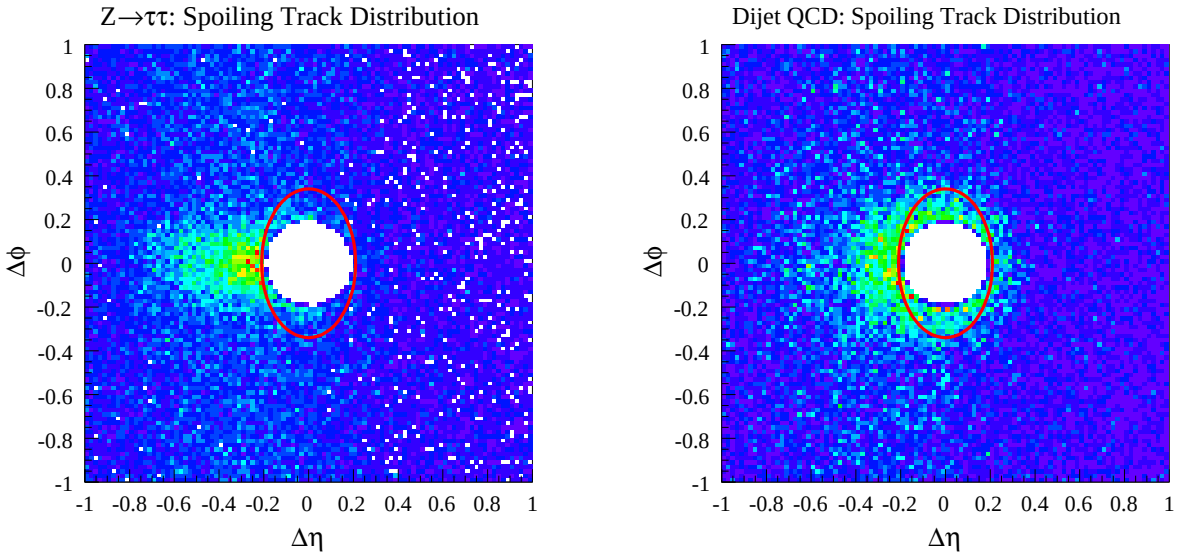

(a) (b)

Figure 4.10: Shape of the isolation cone defined by Equation 4.6 with optimal parameters determined from Figure 4.9.

with a p_T of greater than 6 GeV are available, the seeding process terminates.

After all possible τ lepton candidates have been reconstructed, the isolation cone criteria is applied. The τ lepton candidates are sorted by p_T from high to low, and an isolation cone of the form of Equation 4.6 is drawn around the highest p_T τ lepton candidate. If no tracks from the available track list fall within the isolation cone, the candidate is considered to be a τ lepton. Another signal cone of $\Delta R_S = 0.2$ is drawn around the center of the τ lepton candidate. If any topological calorimeter clusters are found within this cone, they are attached to the τ lepton.

This algorithm ensures that identifying properties of the τ lepton discussed at the beginning of this chapter are utilized to the fullest. Further identification cuts can be made on a variety of variables associated to the reconstructed hadronic τ lepton, and are discussed in further detail in the following chapter.

4.3 Results

To judge the viability of a reconstruction method, a metric must be defined by which to measure the quality of the method. For particle reconstruction and identification, two metrics are used: efficiency and fake rate. The efficiency for hadronic τ lepton identification is defined in Equation 4.8,

$$\varepsilon_S \equiv \frac{N^{\text{rec}}_{\tau_h}}{N^{\text{gen}}_{\tau_h}} \tag{4.8}$$

where $N^{\text{rec}}_{\tau_h}$ is the number of reconstructed τ leptons passing a specific identification method criteria. Additionally each reconstructed hadronic τ lepton must be matched against a generator level hadronic τ lepton by a matching cone with radius $\Delta R < 0.2$. The quantity $N^{\text{gen}}_{\tau_h}$ is the number of generator level hadronic τ leptons in the sample. Each generator τ lepton must be within a fiducial region of $|\eta| < 2.5$ corresponding to the coverage of the tracker. The signal

sample used for the efficiency is $Z \rightarrow \tau^+\tau^-$ with full details given in Appendix A. As explained in Section 4.2, a $Z \rightarrow \tau^+\tau^-$ sample is used as this signal will be very similar to light neutral Higgs decays.

The fake rate is defined by Equation 4.9,

$$\varepsilon_B \equiv \frac{N^{\text{rec}}_{\tau_h}}{N^{\text{gen}}_{\text{jets}}} \tag{4.9}$$

where $N^{\text{rec}}_{\tau_h}$ now is the number of reconstructed τ leptons passing a specific identification criteria, matched against generator level non τ lepton jets, using $\Delta R < 0.2$. The quantity $N^{\text{gen}}_{\text{jets}}$ is the number of generator level jets within the sample that fulfill the criteria $|\eta| < 2.5$. The background samples used are QCD dijets, explained in Section 4.2 with additional details in Appendix A.

To fully understand the effects caused by the proposals for signal and isolation cone, a standard for an identified τ lepton candidate is defined to allow comparison between the methods being explored. Here, a τ lepton candidate is considered identified as a τ lepton if the candidate has a charge of ± 1, has 1, 3, or 5 tracks within the signal cone, and has 0 tracks within the isolation cone. This standard is not optimized and utilizes very few discriminating variables as it is not meant to provide the best possible signal to background ratio, but rather to demonstrate the effects of the signal and isolation cone definitions. By imposing strict requirements on isolation and signal cones these cuts ensure that the effects of the varying definitions are seen.

When providing efficiency and fakerate distributions with respect to parameters such as p_T and η it is important to remember these plots are only projections. While it is clear the range of η should be kept within the fiducial region of the detector, the parameter space to which p_T should be limited is not readily apparent. For efficiency and fakerate plots given with respect to p_T this is not a problem as it is a profile of p_T within the fiducial region of the detector. However, for distributions with respect to η or integrated efficiency over p_T this does pose a problem. As such, it is important to understand the underlying p_T distribution of the decay products at the generator level.

Figure 4.11 gives the p_T probability density function of the visible hadronic τ lepton products of a Z in the left plot. This process is a two body decay, and so using simple probability and a few basic assumptions regarding the physics behind the decay process in question, it is possible to hypothesize a general shape for the distribution of the Z decay products, or of a particle X with a mass greater than the Z. This shape is important as it plays a critical role in the ability of finding SM and MSSM Higgs signals as discussed in Section 2.2.2.

First, assume the Z boson is at rest in the lab frame. This assumption is not valid, as will be seen shortly, but is used as a starting point. From conservation of energy and momentum it is then possible to write the transverse momentum in terms of the Z mass, τ lepton mass, and z component of momentum as is done in Equation 4.10.

$$p_T^2 = \left(\frac{m_Z}{2}\right)^2 - m_\tau^2 - p_z^2 \tag{4.10}$$

Note from above that if the p_T for the system is chosen, then p_z is no longer a free parameter and is uniquely determined. Subsequently, p_z does not play a role in the probability density function of p_T. However, when a specific p_T is chosen, p_x and p_y remain as free parameters of the system. When one of these free parameters is chosen, the other is then uniquely determined, as $p_T^2 = p_x^2 + p_y^2$. It is from this probabilistic choice that the distribution for the p_T is determined.

Assume that the probability density functions for p_i are dependent uniform distributions. Then, without loss of generality, the uniform probability distribution function for p_x can be chosen to determine the probability for a specific p_T value. If a p_T of 20 GeV is chosen, then

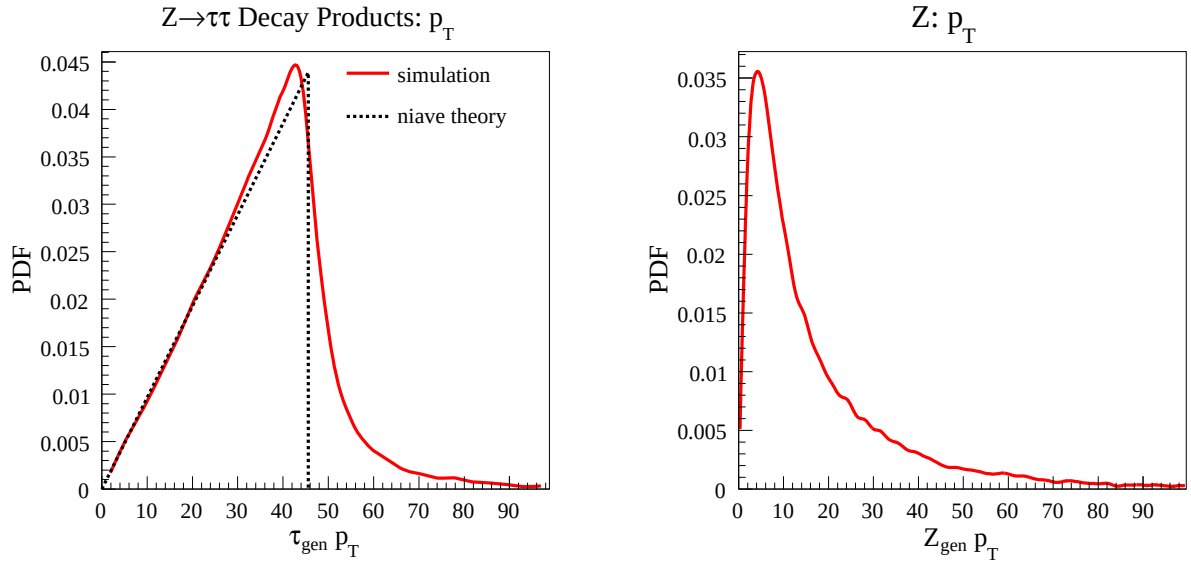

(a) (b)

Figure 4.11: Transverse momentum probability density function for the visible portion of hadronic τ lepton decays from a parent Z is given in (a) with naive theory given in black and Monte Carlo given in red. The subsequent transverse boost of the parent Z, due to the partons of the proton is given in (b) from Monte Carlo.

the probability of this event is determined by the probability of choosing a $p_x \leq 20$ GeV. Hence, the probability density function of the p_T is the cumulative probability density function of p_x. However, this PDF does not take into account the probability that the energy is available for that specific p_T. For energies less than $\sqrt{(m_Z/2)^2 - m_\tau^2}$ this probability is one, and for energies greater than $\sqrt{(m_Z/2)^2 - m_\tau^2}$ this probability is zero. Equation 4.11 gives the probability density function for the decay products of the Z where P_a is the probability of the specific p_T being energetically available.

$$P_{p_T} = \frac{P_\text{a} \int_0^{p_T} \frac{1}{\sqrt{(m_Z/2)^2 - m_\tau^2}}\, dp_x}{\int_0^\infty P_\text{a} \int_0^{p_T} \frac{1}{\sqrt{(m_Z/2)^2 - m_\tau^2}}\, dp_x\, dp_T} \tag{4.11}$$

The shape of Equation 4.11 is just a right triangle terminating at a maximum of $\sqrt{(m_Z/2)^2 - m_\tau^2}$ and is shown by the dotted black line in the left plot of Figure 4.11. However, this shape is dependent upon no boosting of the Z boson in either the z-direction or transverse plane, which is not the case as can be seen in the right plot of Figure 4.11. This boosting, caused by the underlying parton structure of the protons, causes the uniform distribution of p_x to spread into an asymmetric sigmoid. The entire system becomes more complex, but for minor boosting in the transverse plane, the dominant shape of the distribution is still given by Equation 4.11. Note that boosting along the z-axis also effects the distribution as this provides more energy for the system, and changes the distribution of both P_a and p_x. The boosting of the Z along the transverse direction is shown in the right plot of Figure 4.11.

The loss of efficiency from applying a strict p_T range can now be estimated for a worse case scenario by assuming the Z boson has no boost. This is a worst case scenario as the Z boson

will be boosted. Additionally, $\sqrt{(m_Z/2)^2 - m_\tau^2}$ is approximated to be $m_Z/2$ as $m_\tau \ll m_Z$.

$$\varepsilon_S^{\max} \approx 1 - \left(\frac{2p_T^{\text{turn}}}{M_X}\right)^2 \tag{4.12}$$

Equation 4.12 approximates a worst case estimate for the maximum efficiency available for a two body decay into τ leptons from a particle X with a mass M_X. As a minimum p_T of 6 GeV is required for seeding tracks in the track reconstruction method for hadronic τ leptons from Equation 4.12 14% of efficiency for τ lepton reconstruction is already lost for τ leptons originating from a Z boson decay.

This behavior decreases as M_X increases as the form is quadratic and not linear. Subsequently for a light Higgs mass of $M_H = 120$ GeV, just above current experimental exclusion, a 10% loss of efficiency occurs from the turn on. It is also important to note the cross section of the dijet QCD background within this p_T space. A full list of the estimated cross sections for the dijet QCD sample used is given in Appendix A, however the general estimation is for very high cross sections in low p_T ranges while higher p_T ranges have lower cross sections. Specifically the cross section for the range of $8 < p_T < 17$ GeV is $\sigma \approx 1.2 \times 10^{10}$ pb, while for $17 < p_T < 35$ GeV the cross section drops by an order of magnitude to $\sigma \approx 8.7 \times 10^8$ pb.

In the following efficiency and fakerate plots with respect to η and for the significance plots, the reconstructed hadronic τ leptons were required to have a p_T greater than 20 GeV and less than 140 GeV. This immediately cuts the signal efficiency by nearly 20% but provides a realistic p_T range that could be used in an analysis. The lower cut is made to eliminate the large QCD background for low p_T which swamps the signal in this range while the upper cut is used to limit the range to the maximum p_T of the available background samples. For analyses using hadronic τ leptons a variety of lower p_T cuts are used ranging from $p_T > 15$ GeV to $p_T > 60$ GeV [63].

4.3.1 Signal Cone

Candidates were reconstructed using the algorithm described in Section 4.2.4 but with an isolation cone described by $\Delta R_I = 0.4$ and a signal cone defined by both $\Delta R_S = 0.2$ and Equation 4.4. The results using the different signal cone definitions is shown in Figure 4.12 with respect to the transverse momentum and η of the generated τ lepton. For $E_T \gg m_\tau$ the transverse momentum and energy approach each other, and so for $p_T < 25$ GeV it is expected that both methods should produce similar results as is the case. However, for $25 < p_T < 45$ GeV the signal cone definition of Equation 4.4 is outperformed by the constant signal cone definition. The efficiency in this p_T range for the variable signal cone significantly underperforms the constant signal cone while maintaining approximately equal fakerate levels.

By using a variable signal cone, specifically one that shrinks for higher E_T, the isolation cone is simultaneously enlarged, and subsequently all reconstructed hadronic τ leptons are affected, not just three prong decays. Keeping the enlarged isolation cone in mind the efficiency drop can be understood by again considering Figure 4.7. Notice that the density of spoiling tracks appears relatively constant in ΔR up to the limit of ΔR_S and a sharp drop off is not expected for $\Delta R < 0.2$. As such, a large number of spoiling tracks will enter the enlarged isolation cone for lower E_T and an efficiency drop is expected.

However, for transverse momentum greater than approximately 45 GeV the variable size signal cone outperforms the constant size signal cone for signal efficiency while maintaining a similar fakerate. Accounting for the strengths of both the variable and constant size signal cones, a new definition is proposed for the signal cone in Equation 4.13. Here the signal cone remains

at $\Delta R_S = 0.2$ for reconstructed τ leptons with $p_T < 45$ GeV, but for transverse momentum greater than becomes $\Delta R_S = 5/E_T$.

$$\Delta R_S = \begin{cases} 0.2 \text{ for } p_T < 45 \text{ GeV} \\ \\ 5/E_T \text{ for } p_T \geq 45 \text{ GeV} \end{cases} \tag{4.13}$$

Notice that such a definition is advantageous for Z identification but could have significantly different effects for other signals. However for Higgs searches, the signal should be similar to that of the Z and such a reconstruction might prove to be advantageous.

The efficiency and fakerate distributions in η given by plots (c) and (d) of Figure 4.12 do have a distinct shape, but this is expected from detector effects since the detector is not uniform in η. Because the algorithm implemented is only track based with a minimum quality cut it is expected that a higher efficiency will be present in the well covered central region of the detector, and again in the end cap regions of the inner detector. Such a shape is expected in all η distributions, although for the multivariate identification methods described in Chapter 5 these effects are expected to be washed out as sharp cuts such as those used for this section are not used.

4.3.2 Isolation Cone

Having eliminated the moveable center from the definition of the isolation cone given by Equation 4.6 using the simplex algorithm and the spoiling track densities, the parameter space for the optimization problem of the isolation cone is reduced to two variables, r_ϕ and r_η. This is a much more manageable problem and can be optimized using significance defined by $N_S/\sqrt{N_B}$ where N_S is number of passing signal events and N_B is number of passing background events. Using the strict cuts described above and the same reconstruction method as before but with only a constant signal cone, the number of passing signal and background events was calculated and normalized with respect to each other by cross section for an r_ϕ and r_η space from 0.2 to 0.6.

Figure 4.13 shows a contour plot of the significance with respect to r_η and r_ϕ. Similar plots showing profiles for specific r_ϕ and r_η values are given in Figure 4.14 to provide a more intuitive feel for the situation. In these plots however, the relative efficiency versus fakerate is plotted such that highest value for both efficiency and fakerate is normalized to one.

From both Figures 4.13 and 4.14 it can be seen that there is no optimal maximum within the parameter space provided for r_η and r_ϕ. This is expected as for a clean $Z \rightarrow \tau\tau$ event there should be very few spoiling tracks besides the associated τ lepton, and as such the isolation cone could be expanded to the signal cone of the associated τ lepton within the event with very little efficiency cost. However, within the QCD dijet sample a large number of spoiling tracks will fall within these regions, and such an expansion of the isolation cone will cause a large drop in fakerate.

In Figure 4.13 it can be seen that the contour lines become more and more separated for high r_ϕ and r_η representing a significance plateau of approximately 0.07. Whether this plateau is a maximum significance for the size of the isolation cone is unknown, as larger values could yield higher significance. However, as mentioned previously, in actual data large isolation cones are not possible as pile up will degrade the purity of the isolation region within the signal events. Making a compromise between optimizing significance and realizing practical limitations, the isolation cone size can be enlarged to $\Delta R_I = 0.47$, corresponding to the largest contour line of Figure 4.13 with a significance of ≈ 0.068 in comparison to the significance at $\Delta R_I = 0.40$ of

0.064. Such a definition of the isolation cone is still practical for real data, but takes advantage of the plateau observed in Figure 4.13.

Another feature that can be taken from Figure 4.13 is that an increase of r_ϕ or r_η does not provide an advantage in significance. Using the isolines of the plot it is possible to pick a significance and r_ϕ, and from this uniquely determine r_η. Choosing the standard definition of $r_\phi = r_\eta = 0.4$ yields a significance of ≈ 0.064. Following the isoline of this significance yields that for $r_\phi = 0.60$ a value of $r_\eta \approx 0.30$ must be used to maintain the significance. Equivalently, for a value of $r_\eta = 0.60$ a value of $r_\phi \approx 0.34$ must be used.

It could be expected that by varying the shape of the isolation cone, while maintaining the same significance, the efficiencies and fakerates with respect to both η and p_T might change for the different cone shapes. Such a property could provide advantages for identification of specific signals, as efficiencies in certain ranges where the signal is expected could be boosted using such a method. Unfortunately, such a behavior is not exhibited by changing the isolation cone shape while maintaining significance as is demonstrated in the plots of Figure 4.15. Here the previous example of maintaining a significance of ≈ 0.064 for $\Delta R_I = 0.4$, $r_\eta = 0.6$, and $r_\phi = 0.6$ is used. As can be seen, the distributions of efficiency and fakerate in both p_T and η space show only minor differences.

4.3.3 Combined

From the above it is clear that neither the variable signal cone as proposed in Equation 4.4, nor the rough estimate for the isolation cone shape should be used. The variable signal cone could provide an advantage in reconstruction of high p_T hadronic τ leptons using a definition similar to Equation 4.13 but must be treated with care, as it significantly impacts the isolation cone of both single prong and multi prong hadronic τ lepton decays.

The isolation cone, which is used for reconstruction on the trigger level, but only for identification in offline analysis, has no apparent parameterization or shape. Because it is simplest to define the isolation cone as a circle rather than an ellipse, maintaining the current definition would be prudent. Increasing the size of the cone to $\Delta R_I = 0.47$ provides a significance within the plateau observed in Figure 4.13 but may not be useful in reconstruction on the trigger level as it would provide too high of a rejection rate of real τ leptons. For offline reconstruction the isolation cone is not used, but is used for identification as is shown in the following chapter. Using a larger isolation cone than the current definition might prove to be an advantage while using multivariate techniques that do not apply a strict cut on the number of tracks within the isolation cone.

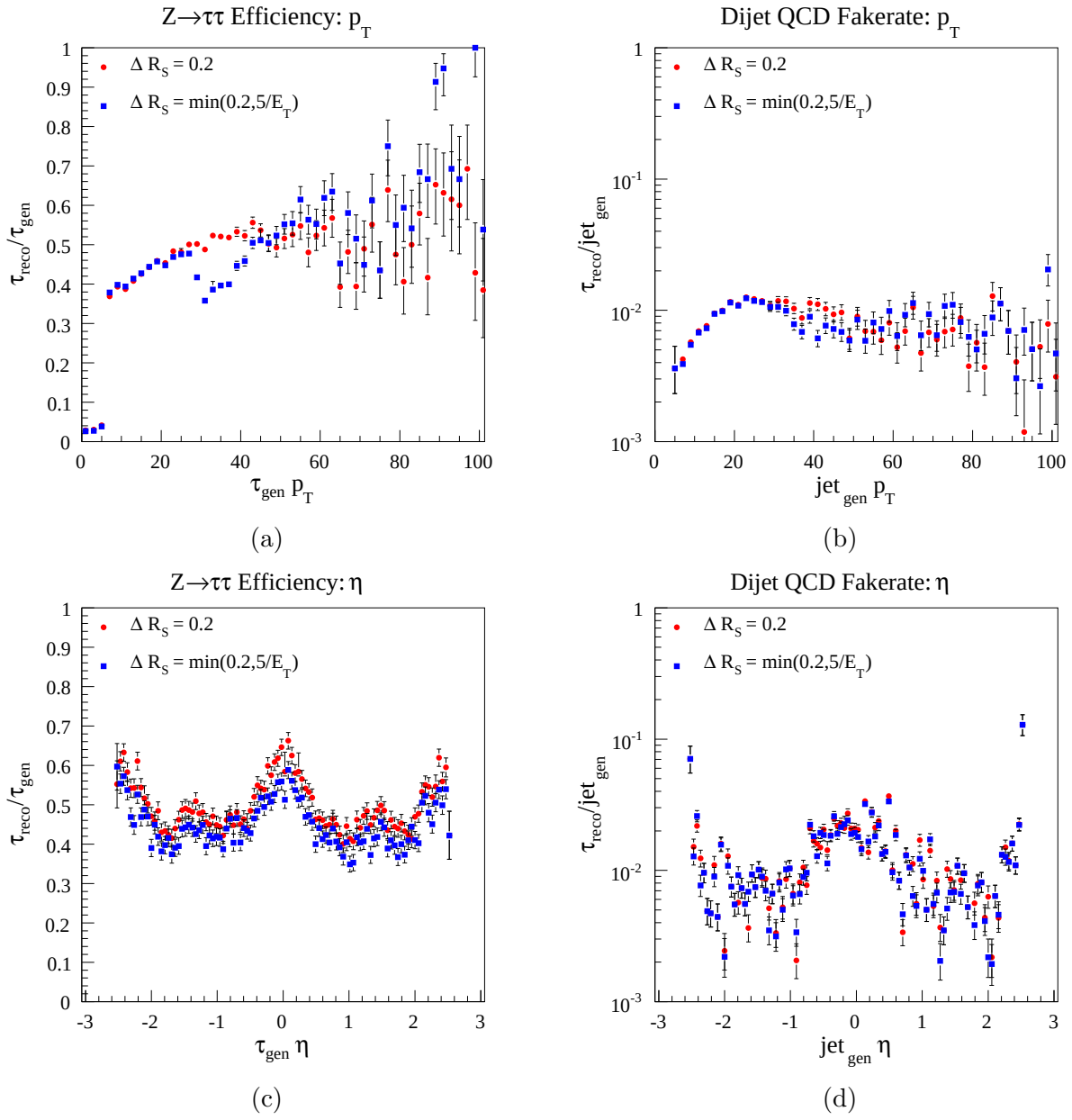

Figure 4.12: Efficiency for τ lepton reconstruction using $\Delta R_S = 0.2$ and the definition of Equation 4.4 is given in (a) and (c). The fakerate using the same methods is given in (b) and (d). Errors were assigned using the methods described in Appendix B.

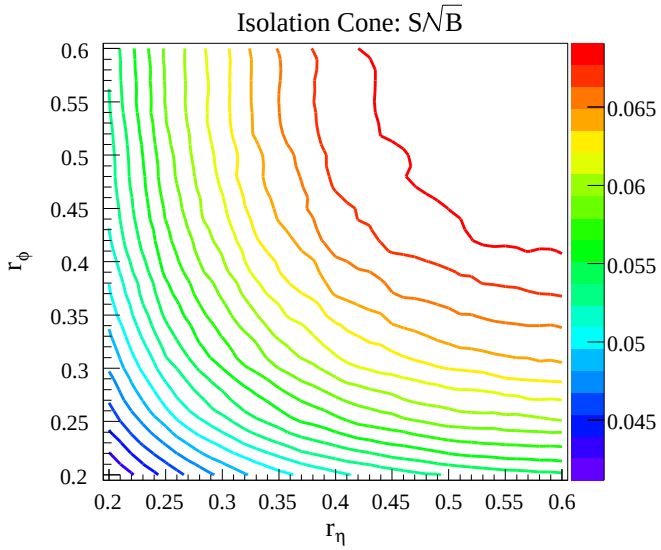

Figure 4.13: Significance of $N_S/\sqrt{N_B}$ for isolation cones of varying shape with $0.20 \leq r_\phi, r_\eta \leq 0.60$.

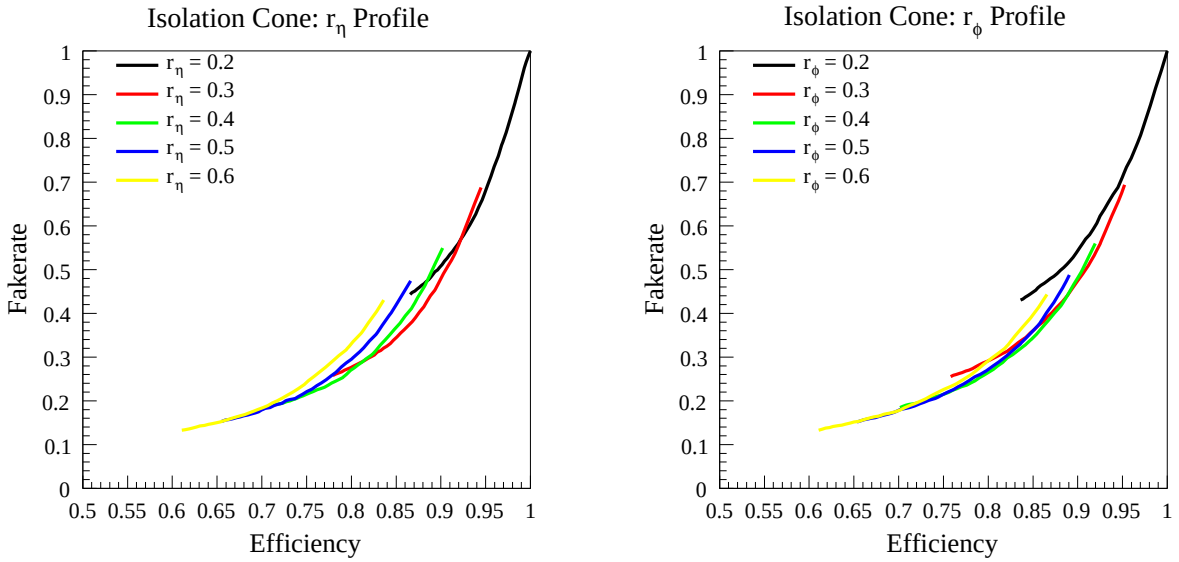

(a) (b)

Figure 4.14: Profiles of efficiency versus fakerate for constant r_η (a) and r_ϕ (b). The efficiencies and fakerates are normalized such that the largest efficiency and fakerate is one.

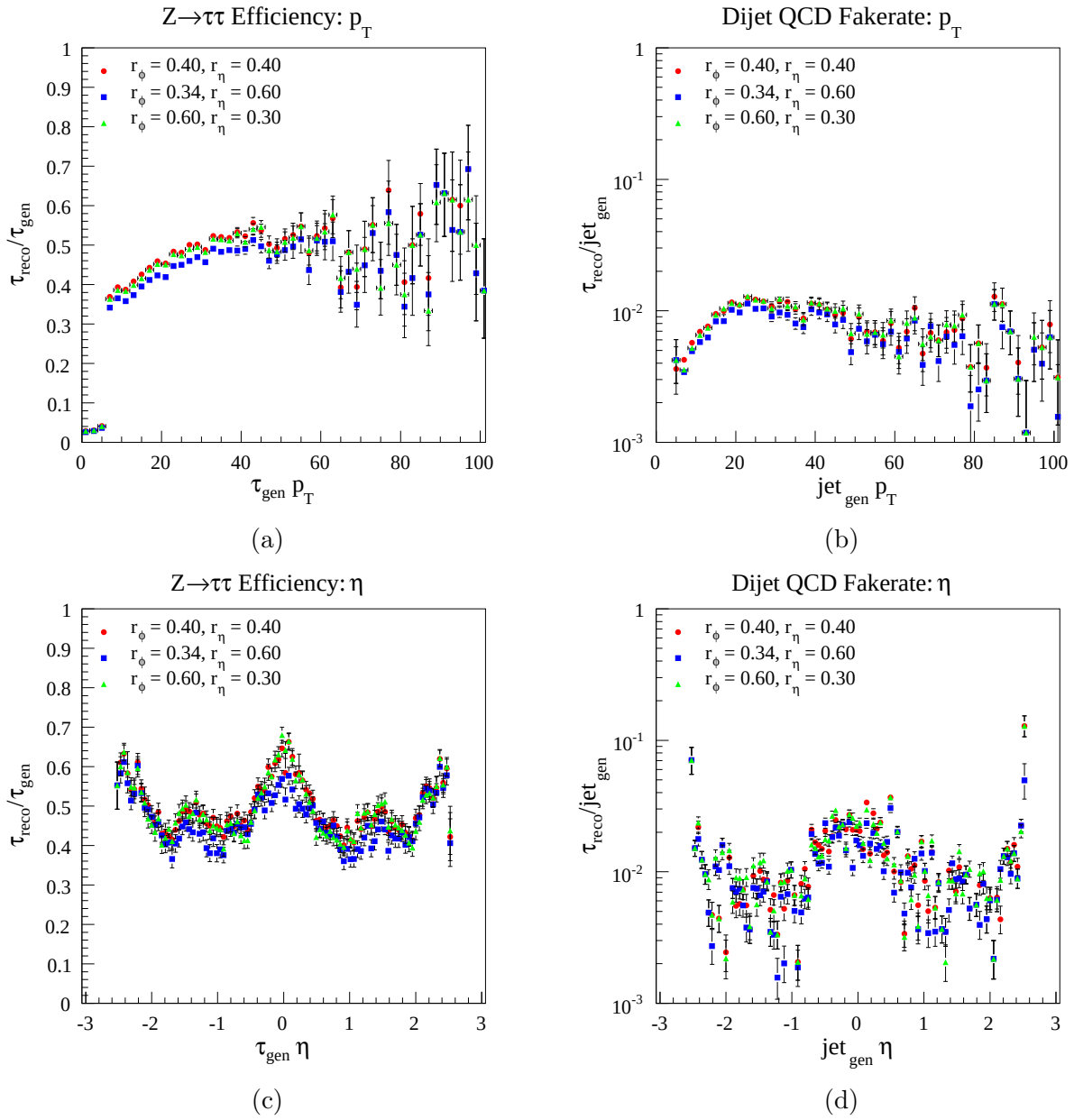

Figure 4.15: Efficiency for hadronic τ lepton reconstruction using varying isolation cone shapes with equivalent significance is given in plots (a) and (c). The same plots for the QCD dijet background fakerates are given in plots (b) and (d).

5 Tau Lepton Identification

Identification of signals within high energy particle physics has changed drastically over the years. What was once done by hand, pouring over photographs from bubble chambers, is now accomplished *en masse* by machines. Computer science has also evolved significantly over the years, and many fast and stable machine learning algorithms have been developed. While cut based analyses provide a simple, stable, and easily controlled method by which to identify particles, more advanced techniques using machine learning algorithms can provide a distinct advantage. In the case of τ lepton identification, a large group of variables are available on which to perform a cut based analysis. However, each of these variables is weak, and provides only slight signal and background separation. Due to the weak nature of the variables, performing a τ lepton identification analysis by hand can be difficult, and have less than optimal results. The following sections outline the variables and various methods currently available for τ lepton identification by the ATLAS collaboration.

5.1 General Variables

A variety of general variables are used by official ATLAS identification to determine the quality of a hadronic τ lepton candidate. These variables can either be used in a cut based analysis, or with more advanced multivariate techniques, as will be described in the following section. The variables can be divided into three categories: inner detector, calorimeter, and combined.

The following provides a brief description of each variable, how it is pertinent to hadronic τ lepton identification, and plots comparing the variable in both signal and background. The same $Z \rightarrow \tau\tau$ signal sample of Section 4.2 is used along with the dijet QCD background. Signal is always given in blue while background is given in red. The number of events for both signal and background are normalized such that the area under the curve is one. This allows the shapes of both signal and background to be easily compared.

All signal plots were made matching reconstructed hadronic τ leptons against visible generator level hadronic τ leptons with a cone of $\Delta R = 0.2$. This matching ensures that the signal variables seen match actual τ leptons opposed to false candidates. No matching requirement were made on the background except to ensure that the faking τ lepton candidate did not come from an actual generator level τ lepton.

5.1.1 Inner Detector

The inner detector provides a variety of important variables for hadronic τ lepton identification. Specifically, the inner detector provides the number of signal tracks, number of isolation tracks, track width for three or five prong decays, charge, and partial or full mass.

Number of Signal Tracks

From Section 2.2.1 it is apparent that hadronic τ leptons should have either one, three, or, on the rare occasion, five tracks within the signal cone. This of course does not always occur, as

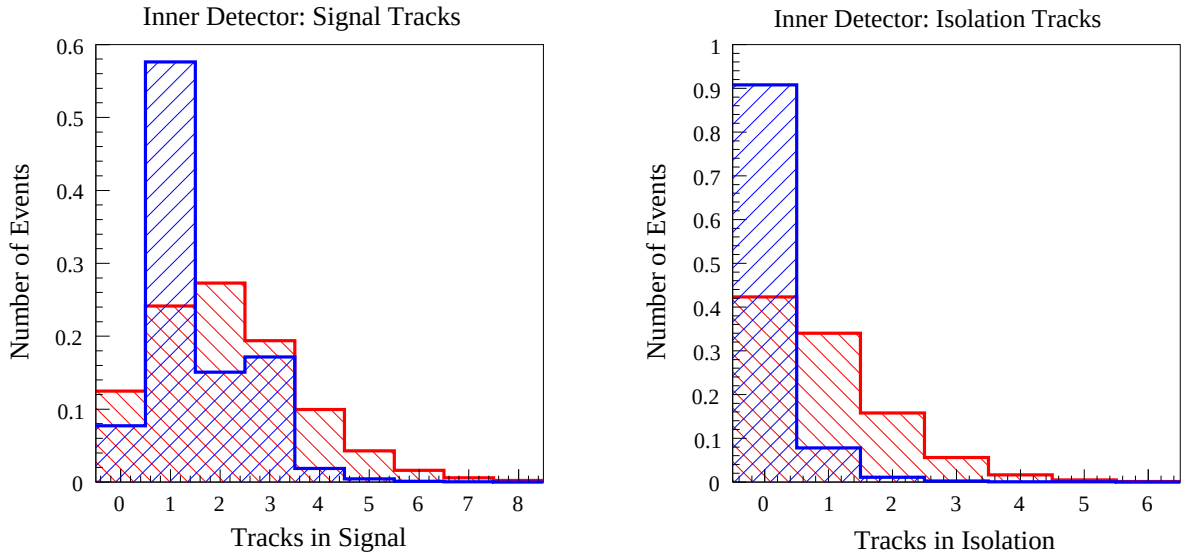

(a) (b)

Figure 5.1: Plot (a) shows the number of signal tracks associated with a τ lepton candidate from the signal (blue) and the background (red). Plot (b) shows the number of tracks spoiling the isolation cone.

spoiling tracks not associated to the τ lepton decay may enter the signal cone and create a reconstructed τ lepton object with two tracks from what was a one prong decay. Similarly, a track from the τ lepton decay may not be reconstructed from a three or five prong decay, causing a τ lepton object with two or four associated tracks.

The left plot of Figure 5.1 shows the number of signal tracks for the $Z \rightarrow \tau\tau$ process in blue and the dijet QCD sample in red. A maximum for the signal sample occurs at one associated signal track, as it should. However, signal candidates with two signal tracks are identified at approximately the same rate at which candidates with three signal tracks are identified. The background candidates peak at two signal tracks, and as such the number of signal tracks provide a possible cut to eliminate a large portion of the background without eliminating a significant portion of the signal.

Number of Isolation Tracks

The number of tracks within the isolation cone of a τ lepton candidate provides an important handle for identification as previously discussed in Section 4.2.3. The right plot of Figure 5.1 demonstrates that the isolation cone does indeed play an important role in identification. Nearly 90% of all signal candidates have no spoiling tracks within their isolation cone. In direct contrast, the majority of background candidates have one or more spoiling tracks within their isolation cones. By providing an optimized isolation cone shape, this stark contrast between signal and background can be improved upon even more.

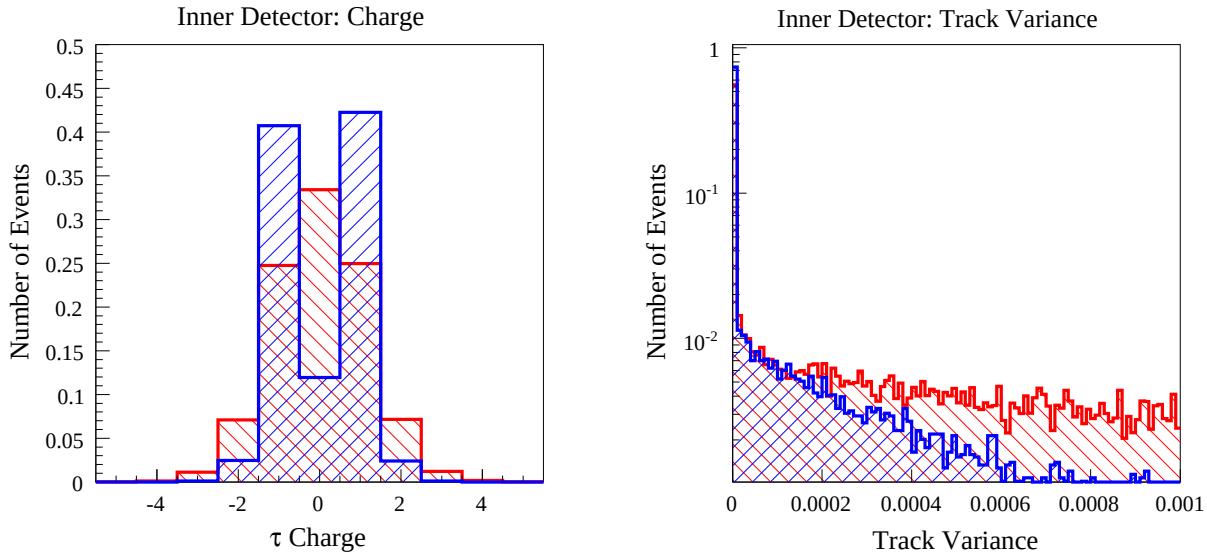

(a) (b)

Figure 5.2: Plot (a) gives the charge for τ lepton candidates from signal and background. Plot (b) gives the track variance as defined in Equation 5.1.

Charge

Theoretically, the charge of a τ lepton candidate should be ± 1 as these are the only physical values. However, due to tracks not being properly added to the signal cone, or extra tracks being added to the signal cone, oftentimes the charge of a τ lepton candidate can be zero. The left plot of Figure 5.2 shows that this misidentification of charge does not occur very often, but is not negligible. For the QCD dijet background the charge distribution appears to be normally distributed about a mean charge of zero. The charge variable is highly correlated to the number of signal tracks variable, and provides an excellent method by which to separate signal and background.

Track Variance

The track variance is only defined for multi prong candidates, and subsequently this parameter cannot be utilized for a large number of possible τ lepton candidates. The variance is defined by Equation 5.1 where $\Delta\eta$ is taken between the center of the τ lepton candidate and the composite tracks [26].

$$\text{Track Variance} \equiv \frac{\sum_i \Delta\eta^2(\tau, \text{track}_i) p_T^{\text{track}_i}}{\sum_i p_T^{\text{track}_i}} - \left(\frac{\sum_i \Delta\eta(\tau, \text{track}_i) p_T^{\text{track}_i}}{\sum_i p_T^{\text{track}_i}} \right)^2 \tag{5.1}$$

The track variance, as shown in the right plot of Figure 5.2 does not provide a very strong separation variable, but can be used in multivariate techniques where weak separation variables can provide performance boosts. Note that the the peak at zero is from single prong decays or candidates without associated tracks, where the track variance is not defined.

Impact Parameter Significance

The impact parameter significance is given by the lateral impact parameter d_0 over the error assigned to the measurement, $d_0/\sigma(d_0)$. The impact parameter of a τ lepton is 87.11 μm so for the majority of τ leptons the error on the impact parameter measurement will be well over the value of the actual parameter. However, as shown in the left plot of Figure 5.3 this parameter does vary slightly between signal and background. As expected, the tail of the distribution for signal τ lepton candidates falls off less quickly than the tail for the background. This is because the jets are expected to be from the primary vertex, while the τ leptons are produced from a secondary vertex, albeit a small distance from the primary vertex. Again this variable is too weak to be used in a standard cut based analysis, but can be used in multivariate techniques.

5.1.2 Calorimeter

While the calorimeter cannot easily differentiate between the number of prongs from a τ lepton decay, variables from the calorimeter can help determine the collimation and isolation of the decay jet. This is especially important for collimation, as the possible neutral particles of a hadronic τ lepton decay will not be measured within the inner detector.

Electromagnetic Calorimeter Radius

The electromagnetic calorimeter radius is a critical quantity used in the hadronic τ lepton triggers as discussed in Section 4.1.1 with the quantity defined in Equation 4.1. This variable exploits the collimation of the τ lepton, just as the signal track variance and number does, and is expected to be a stronger variable for separation. This is the case, as can be seen in the right plot of Figure 5.3. Here there is a clear separation between signal and background with the radius for the background having a peak at ≈ 0.17 and the radius for the signal having a peak near ≈ 0.05. This variable can be used both in a direct cut based analysis and a multivariate approach.

Isolation Fraction

The isolation fraction is the normalized difference between a region of size $\Delta\eta \times \Delta\phi = 0.1 \times 0.1$ over a region of size $\Delta\eta \times \Delta\phi = 0.2 \times 0.2$ as given by Equation 5.2 [64].

$$\text{Isolation Fraction} \equiv \frac{\sum_{0.2} E_{\text{cell}} - \sum_{0.1} E_{\text{cell}}}{\sum_{0.2} E_{\text{cell}}} \tag{5.2}$$

Here a sum is performed over all calorimeter cells within the larger 0.2×0.2 region, less the sum of the cells within the smaller region. This quantity is normalized by the sum over the cells within the larger region.

From Equation 5.2, the isolation fraction is expected to be small for well isolated events, such as actual τ leptons, and larger for less isolated QCD events. The left plot of Figure 5.4 shows this is the case with the isolation fraction for the signal peaking near ≈ 0.01 and the isolation fraction for the background peaking at ≈ 0.03. Isolation fraction, just like number of spoiling isolation tracks is a strong separation variable and can be used in cut based analyses.

Number of Hits within Strip Cells

The number of hits within the strip cells is defined to be the number of hits within the η strip of the topological cluster associated with the τ lepton candidate with an energy of $E_T > 200$

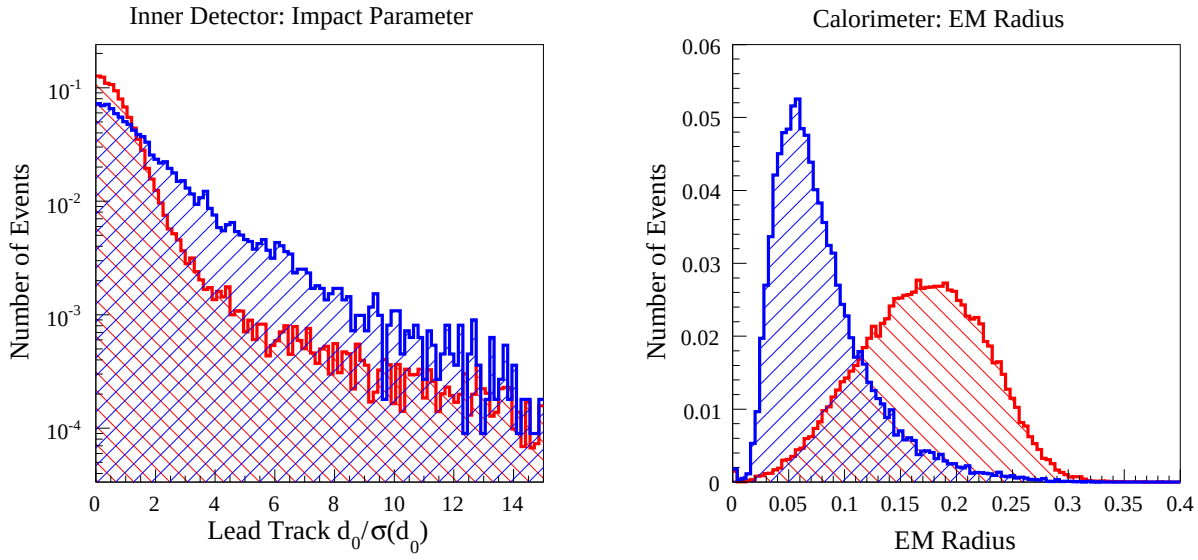

(a) (b)

Figure 5.3: Plot (a) shows the lateral impact parameter significance while plot (b) shows size of the τ lepton candidate within the EM calorimeter as defined in Equation 4.1.

MeV. For τ leptons this number is expected to be near the number of particles within the decay, so ranging anywhere from one to greater than eight. For background jets this number should be less, as the number of highly boosted particles within the jet will be limited. This behavior can be seen in the right plot of Figure 5.4 with the tail of the background distribution falling off much faster than the signal distribution.

Weighted Strip Width

The weighted strip width provides a variable that describes the shape of the energy deposited within the calorimeter with respect to the η of the calorimeter cells. The variable is defined by Equation 5.3, where summations are performed over cells within a block of size $\Delta\eta \times \Delta\phi = 0.3 \times 0.3$ [64].

$$\text{Strip Width} \equiv \sqrt{\frac{\sum_{0.3} \eta_{\text{cell}}^2 E_{\text{cell}}}{\sum_{0.3} E_{\text{cell}}} - \left(\frac{\sum_{0.3} \eta_{\text{cell}} E_{\text{cell}}}{\sum_{0.3} E_{\text{cell}}}\right)^2} \tag{5.3}$$

This definition is synonymous with the variance of the track width for multi prong decays defined in Equation 5.1 but for the calorimeter. As the τ leptons should be highly collimated, the variance on the strip width should remain low. For the background jets however, collimation is not as delineated and so the variance should vary over a much larger range. This behavior is shown in the left plot of Figure 5.5. Unfortunately this variable is not a strongly separating variable and can only be used effectively in multivariate techniques.

5.1.3 Combined

Combined variables are able to provide values from both the inner detector and calorimeter in a single variable with discriminating power. As most reconstructed τ lepton objects have both

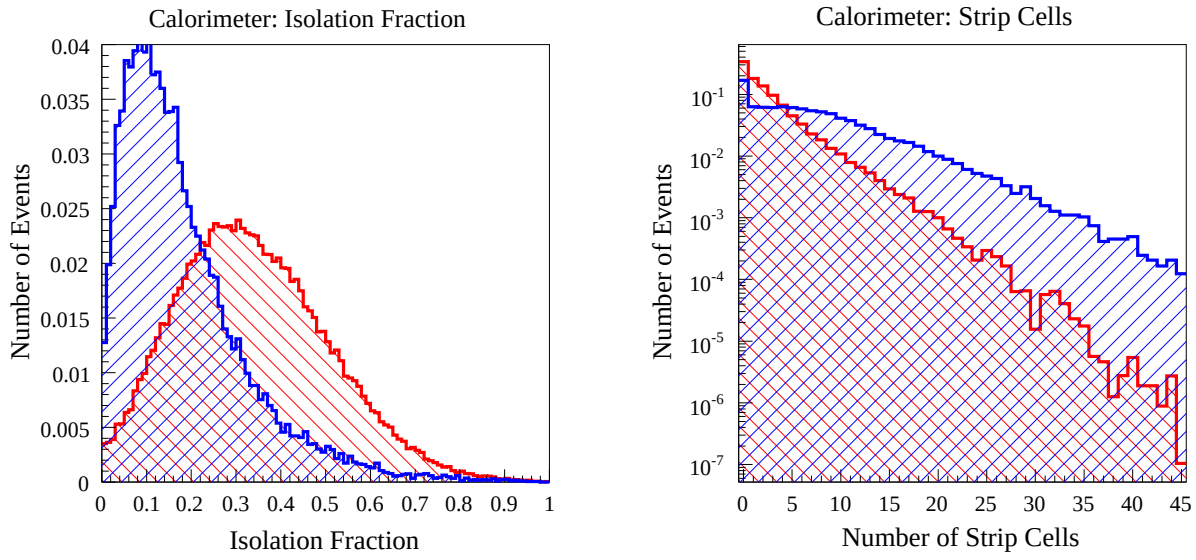

(a) (b)

Figure 5.4: Plot (a) shows the isolation fraction of the topological calorimeter cluster associated with the τ lepton candidate as defined by Equation 5.2. Plot (b) gives the number of hits with $E_T > 200$ MeV within the η strip associated with a τ lepton candidate.

tracks and topological calorimeter clusters associated with them, these variables are available for most reconstructed τ lepton candidates.

Tau Lepton E_T over p_T

This value is the total transverse energy of the τ lepton candidate over the p_T of the lead track used to reconstruct the candidate. The majority of τ leptons have one prong decays and subsequently have the majority of their energy concentrated within one or two particles. The ratio from the signal is expected to be near one. The background jets however have a larger number of tracks, as shown in Figure 5.1 and so the ratio is expected to be higher for the background. The right plot of Figure 5.5 demonstrates this behavior.

Mass

While traditionally the mass of the τ lepton candidate is calculated directly from the momenta vector of the associated tracks, this method produces masses well below the mass of the τ lepton due to $\not{E}_T$ from neutrinos and not accounting for the energy from neutral particles. Within the ATLAS collaboration energy flow techniques are used to correct the energy of the reconstructed τ lepton using both calorimetry information and $\not{E}_T$ information from the event. This technique is apparent in Figure 5.6, as the number of events with a mass corresponding nearly exactly to that of the full τ lepton is very large. This technique has great promise, but still requires significant work. As of now the discriminating ability of the object mass is minimal.

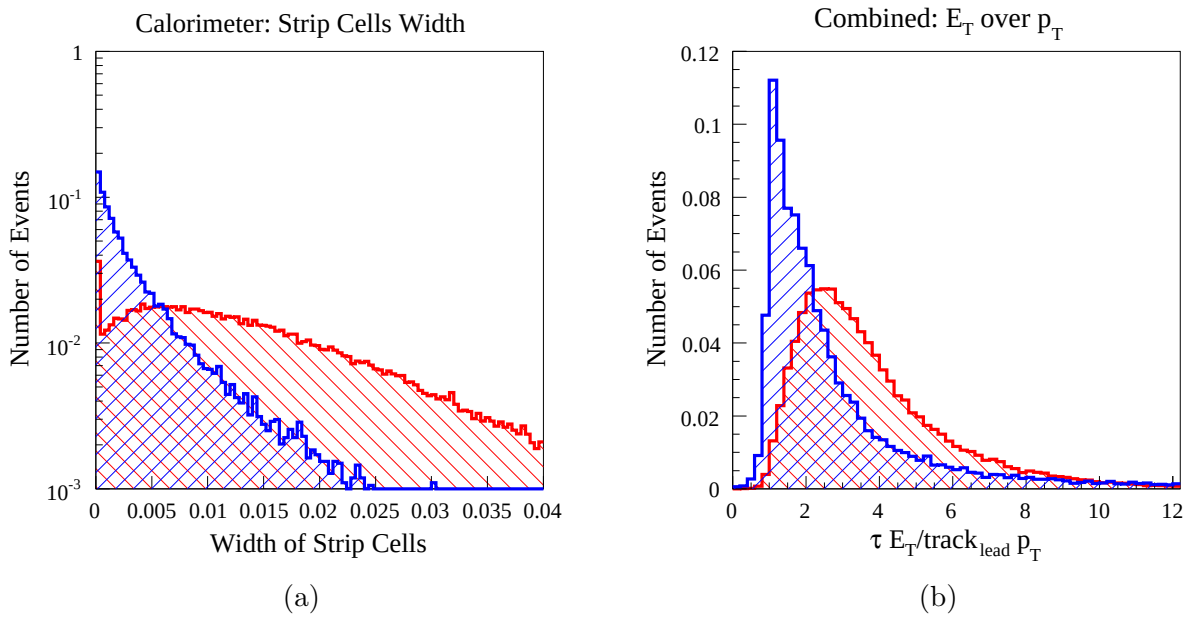

(a) (b)

Figure 5.5: Plot (a) shows the weighted width of strip cells as defined by Equation 5.3. Plot (b) shows the ratio of the total E_T of the τ candidate over the p_T of the lead track.

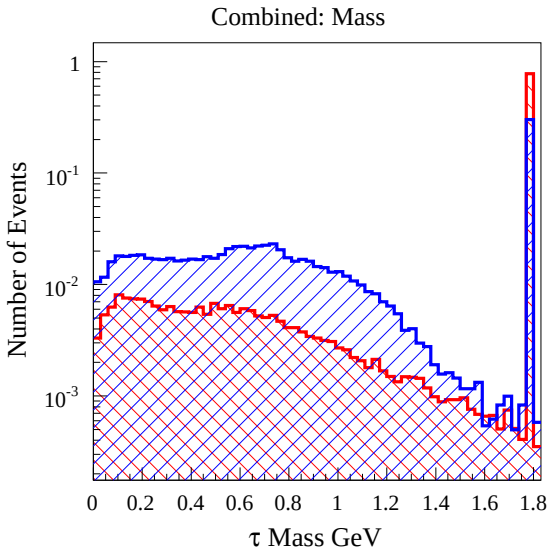

Figure 5.6: Mass of the reconstructed τ lepton candidate using energy flow techniques for signal and background.

Hadronic over Track Energy

An additional variable combining both inner detector and calorimeter information is the hadronic energy within the calorimeter over the total energy of the associated tracks. Unfortunately this current variable was not available in the samples used for this study, and plots could not be made.

5.2 Methods

ATLAS uses a variety of multivariate techniques along with standardized cut based definitions for hadronic τ lepton identification. The four techniques used in current analyses are described and compared: standardized cut flow analysis, the likelihood method, artificial neural nets, and boosted decision trees.

5.2.1 Cut Flow

Because multivariate methods rely heavily upon Monte Carlo or previous data with separated signal and background, it is necessary to develop a safe cut based identification method. Within large collaborations such as ATLAS it is important to have standard definitions so that common physics objects such as the hadronic τ lepton remain consistent amongst the working groups.

Within ATLAS three standard cut flow definitions of "tight", "medium", and "loose" are defined corresponding to 70%, 50%, and 30% efficiencies with respect to all reconstructed τ lepton candidates. The cut flows for these definitions are given in Table 5.1 for one and multi prong τ lepton candidates from the merged calorimeter and inner detector seeded algorithms. The cut flow for one and multi prong candidates are given in separate tables, as the optimal cut values depend upon the kinematics of the event. The values of Table 5.1 can be compared to Figures 5.1 through 5.6 for a rough estimate of the efficiency drop for each cut.

As the number of reconstructed τ lepton candidates is usually larger than the number of generator level τ leptons within a sample, these numbers are lower than the actual efficiency. Figure 5.7 shows the efficiencies and fakerates of the three standard cut flow definitions using the same method as described in Section 4.3 for calculating efficiencies and fakerates. As can be seen, there are large turn on's in both the efficiency and fakerate with respect to low p_T especially for the "tight" cut flow. Unlike the simpler cut based analysis of Chapter 4 the tails of the distributions in p_T also fall with respect to p_T except for the "loose" efficiency.

Structure can also be seen in the η distributions, again expected as the detector is not uniform in η. The structure however is much less noticeable than in Chapter 4 as now both calorimetry and inner detector variables are being used to reconstruct and identify the τ leptons. Contributions from both the calorimeter and inner detector still lend structure to the distribution but wash each other out.

Similar standard definitions of "loose", "medium", and "tight" are also provided for the likelihood method but are not used for the artificial neural net and boosted decision tree methods. However, for the purposes of comparison, the efficiencies for the artificial neural net and boosted decision tree methods were matched such that the total efficiency of the "tight" cut for the cut flow method corresponds to the same total efficiencies for both the artificial neural net and boosted decision trees. Similar matching was applied for "medium" and "loose".

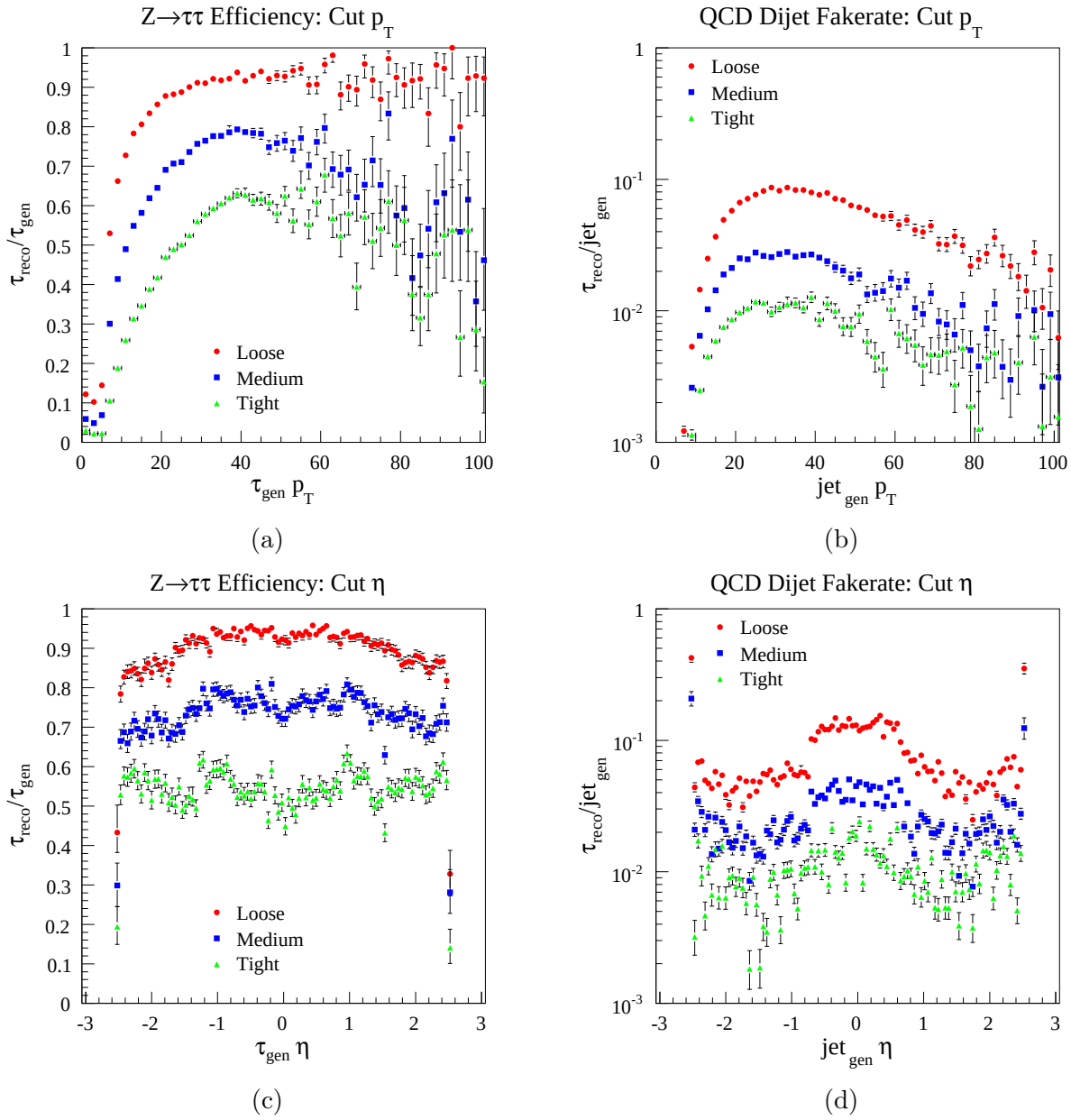

Figure 5.7: Plots (a) and (c) give the efficiency in p_T and η for the three standardized cut flow defintions corresponding to a 70%, 50%, and 30% efficiency with respect to reconstructed candidates. The equivalent fakerate plots are given by (b) and (d).

Signal Tracks = 1

Variable	Loose Value	Medium Value	Tight Value
Isolation Tracks	< 1000	< 1	< 1
Bad Signal Tracks	< 1000	< 1	< 1
Mass [GeV]	< 1000	< 1.8	< 1.6
Strip Cell Hits	< 1000	< 10	< 8
EM Radius	< 0.12	< 0.12	< 0.08
Strip Width	< 1000	< 0.0012	< 0.0008
Isolation Fraction	< 0.9	< 0.6	< 0.4
EM Isolation	< 0.9	< 0.15	< 0.1
E_T over p_T	< 6	< 6	< 5

Signal Tracks ≥ 2

Variable	Loose Value	Medium Value	Tight Value
Isolation Tracks	< 1000	< 1	< 1
Bad Signal Tracks	< 1000	< 1	< 1
Mass [GeV]	< 1000	< 1.8	< 1.6
Track Mass [GeV]	< 1.8	< 1.8	< 1.5
Strip Cell Hits	< 1000	< 10	< 8
EM Radius	< 0.15	< 0.15	< 0.10
Strip Width	< 1000	< 0.002	< 0.0015
Isolation Fraction	< 0.9	< 0.6	< 0.4
EM Isolation	< 0.9	< 0.3	< 0.2
Track Width	< 0.002	< 0.002	< 0.0015
E_T over p_T	< 10	< 10	< 8

Table 5.1: "Loose", "medium", and "tight" cut flow definitions as taken from `TauCommonSetIsTau.py` version 1.1 for merged τ lepton one and multi prong candidates are given in the upper and lower tables respectively. These defintions fluctuate significantly between software releases and the values listed above are meant only as a guide. The most current values, at the time of writing, are given in Reference [65].

5.2.2 Likelihood

The method of maximum likelihood was first proposed in a rudimentary form by Ronald Fisher in 1912, and has since become one of the most widely used statistical tools for determining optimal free parameters of a system [66]. Likelihoods have now become a common standard in high energy particle physics analysis, being currently used by DØ, CDF, CMS, and ATLAS for various identification techniques. The ATLAS reconstruction software Athena uses a logarithmic likelihood method in its current software releases for hadronic τ lepton identification [67].

The likelihood for a signal or background is given by Equation 5.4,

$$L \equiv \prod_i P_i(x_i) \tag{5.4}$$

where a product is performed over the probability distribution functions, $P_i(x_i)$, for each variable

x_i with which the likelihood is being calculated. The likelihood discriminant is then given by,

$$D \equiv \frac{L_S}{L_S + L_B} \tag{5.5}$$

where L is the likelihood for either signal or background as given by Equation 5.4. This discriminant by definition must be contained within the range of zero to one. However, due to the weak nature of the variables available for τ lepton identification, the discriminant as defined by Equation 5.5 has large peaks at both zero and one. To provide a discriminant that yields a more linearly varying efficiency, a transformed discriminant is used, defined by Equation 5.6.

$$D_{\ln} \equiv -\ln\left(\frac{1}{D} - 1\right). \tag{5.6}$$

This definition of the discriminant with a logarithmic scale allows for a more linear response of the efficiencies based on the discriminant value specified [68].

The likelihood discriminant for ATLAS hadronic τ identification was trained on a $W \rightarrow \tau\nu_\tau$ signal sample and dijet QCD sample. As such, the resulting performance for a $Z \rightarrow \tau\tau$ signal is expected to be less than optimal. The probability distribution functions generated for the signal sample were binned according to p_T and whether the τ lepton decay was one prong or multi prong. One prong decays were further split into two groups, one with no identified π^0 clusters within the EM calorimeter, and one with multiple π^0 clusters identified.

For the one prong samples, probability distribution functions were made for all the variables of Section 5.1 excluding track width, charge, number of tracks in the signal cone, and number of tracks in the isolation cone. Additionally ratios of energy deposited in the calorimeter over energy in associated signal tracks were used along with the significance of the longitudinal impact parameter, $z_0/\sigma(z_0)$. For the multi prong samples all of the above variables were used, excluding the longitudinal impact parameter significance. Additional tracking variables were used including number of signal tracks, and signal track separation [67].

The left plot of Figure 5.8 shows the likelihood distribution of the hadronic τ candidates for both the signal in blue and the background in red. Both sets of events are normalized to an integral of one. Significant separation between the signal and background distributions can be seen, with the background distribution centered around -20 and the signal distribution centered around 0.

The right plot of Figure 5.8 gives the significance, again defined by $N_S/\sqrt{N_B}$ as is done in Section 4.3. The significance is better than the maximum significance of Figure 4.13 for likelihood discriminant values greater than -2 as expected. A peak significance of 0.16 is reached at $D \approx 10$. This is nearly double the significance of the simple cut based analysis of Section 4.3 and demonstrates the simplicity yet power of using the likelihood method.

Figure 5.9 gives the efficiencies and fakerates for the likelihood method with respect to η and p_T for the likelihood method. The efficiency with respect to p_T has an even more pronounced turn on than for the cut flow method, but does not drop for higher p_T. The structure within the efficiency plot with respect to η, specifically for the "loose" likelihood indicates that the likelihood method requires more stringent cuts on inner detector variables. Note that by just using a simple likelihood the same efficiency as the cut flow technique can be maintained while decreasing the fakerate by nearly an order of magnitude.

5.2.3 Artificial Neural Net

The artificial neural net was first conceived by Frank Rosenblatt in 1957 as a method by which to approximate any given function using a weighted series of units in a network closely modeling

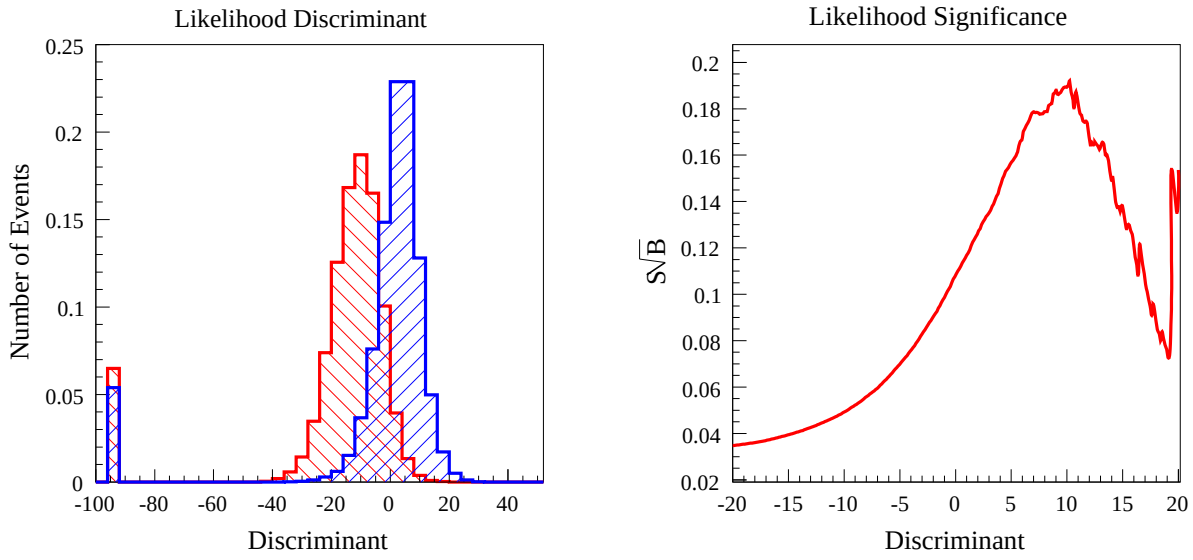

(a) (b)

Figure 5.8: Distributions of the normalized number of events and significance with respect to the log discriminant given by Equation 5.6 for the likelihood method.

the neural networks of the human mind [69]. However, the method proposed by Rosenblatt was a single layer feed-forward network, or perceptron, which was capable of only separating linearly dependent variables. It was hypothesized by Minsky and Papert that such a property would hold for multi layer perceptrons, dimming interest in artificial neural networks [70]. During the 1980's interest was renewed in artificial neural networks, and in 1989 Cybenko proved: "finite linear combinations of compositions of a fixed, univariate function and a set of affine functionals can uniformly approximate any continuous function of n real variables with support in the unit hypercube" [71]. Further proofs have practically shown that a multi-layer perceptron with a finite number of units can arbitrarily approximate a universal Turing Machine [72].

A wide variety of artificial neural network techniques are currently available. However, as current τ lepton identification within the ATLAS collaboration is performed by a two layer perceptron implemented with the Stuttgart Neural Network Simulator [73], this particular method will be described.

The building blocks of a neural net are units and links. The units may be of three types: input, hidden, and output. These types correspond to the input variables, the two hidden layers, and the output discriminant respectively, of which a basic schematic is given in Figure 5.10. Each unit is connected by a weighted directed link. As the neural net used is a perceptron or feed-forward network, only forward directed links are allowed as seen in Figure 5.10. Each unit has an associated activation value $a_j(t)$, activation function f_a, output function f_o, bias θ_j, output $o_i(t)$, and net input $n_j(t)$. Here the indices i, j represent a unit index and t designates the iteration step. Each link has a weight $w_{ij}(t)$ connecting the unit i to the unit j where $i < j$, by the necessity of a feed-forward mechanism.

The net input for a unit is defined by Equation 5.7,

$$n_j(t) \equiv \sum_i w_{ij} o_i(t) \tag{5.7}$$

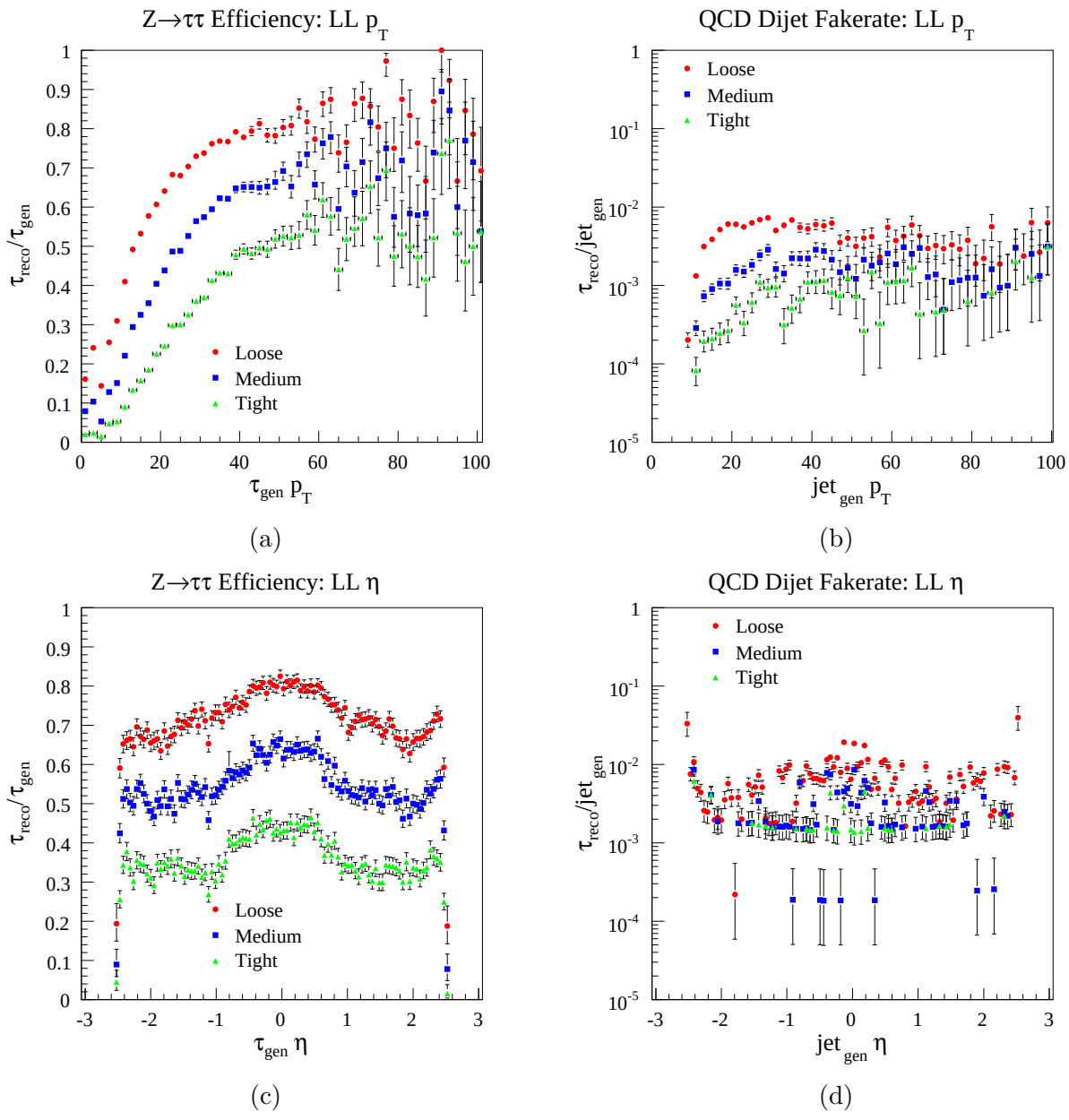

Figure 5.9: Efficiencies for the likelihood method are given in (a) and (c). The equivalent fakerate plots are given by (b) and (d).

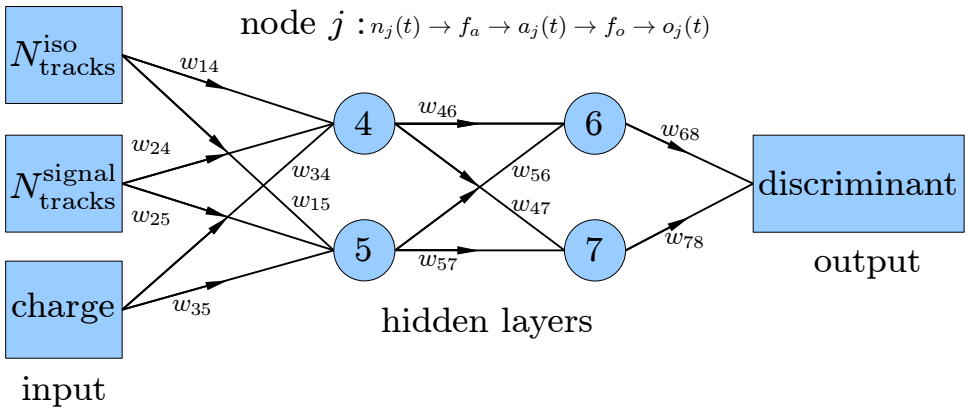

Figure 5.10: Schematic of a simple multi layer perceptron for τ lepton identification. Three input nodes: number of signal tracks, number of isolation tracks, and charge are provided. Each node feeds forward to a hidden layer of two nodes, which feeds into another hidden layer of two nodes, terminating in the output node or discriminant of the network. A signal input training event has a theoretical discriminant of one, while a background training event has a theoretical discriminant of zero. Error from backward propagation is calculated using these values. An example chain of calculations is given for an example node j.

where the sum of all connecting units outputs is taken, with the corresponding weight of each connecting link. The activation function used is the common logistic activation function,

$$f_a(n_j(t), \theta_j) = \left(1 + e^{\theta_j - n_j(t)}\right)^{-1} \tag{5.8}$$

from which the next iterative activation value is calculated by Equation 5.9.

$$a_j(t+1) = f_a(n_j(t), \theta_j) \tag{5.9}$$

The output value $o_j(t)$ is then calculated using the output function $f_o(a_j(t))$, where in general $f_o(a_j(t)) = a_j(t)$.

A neural net is trained by providing a signal sample and background with inputs from a variety of variables. The net is iterated over, computing the activation and output of units for some predefined iterative method ranging from serial to random. After the completion of an iterative cycle or forward propagation, backward propagation is performed, where the weights of the links are adjusted according to the errors between the output value and the input values of each layer. After backward propagation, the cycle repeats until relative stability is reached. After the network has been trained, a validation set of background and signal is used to evaluate the effectiveness of the training.

In many cases neural nets can be over trained, picking out patterns that are specific to the training samples, rather than general patterns of the process itself. When over training occurs, the signal sample shows an excellent discriminate distribution, with signal easily distinguishable from background. However, when the neural net is applied to a new sample of signal and background, a large number of events are found to have a discriminant of one or zero. Such training of a neural net can be avoided by using large samples, or validating the training often, taking care to avoid the discriminant behavior described above.

Currently, within ATLAS, neural networks have been only trained for inner detector seeded τ leptons associated with one or three tracks. The network is a two layer perceptron with nine,

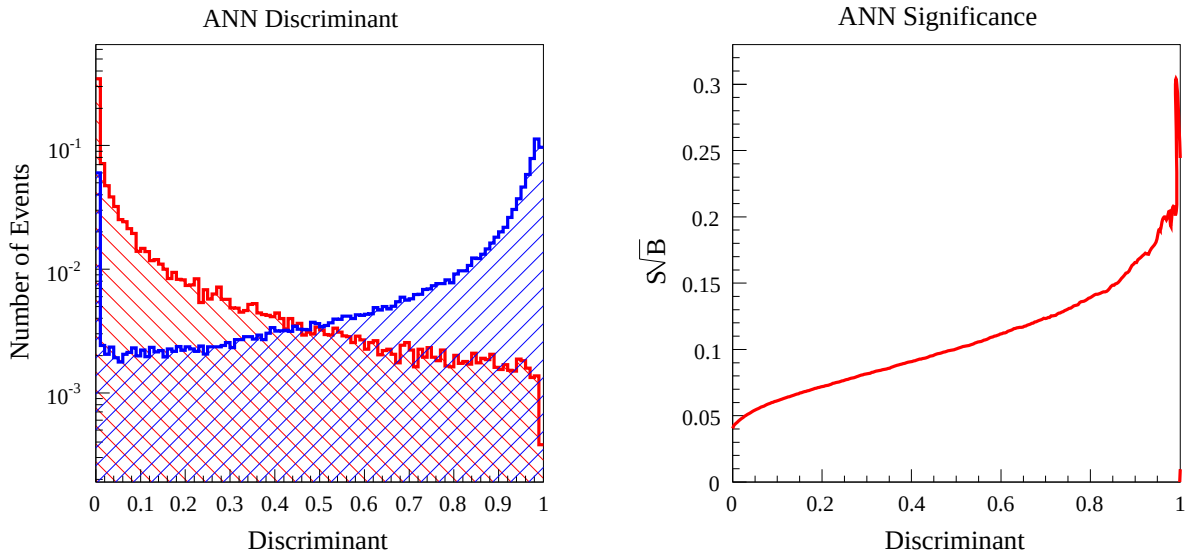

(a) (b)

Figure 5.11: Distributions of the normalized number of events and significance with respect to the discriminant for the artificial neural net identification method.

ten, or eleven inputs, thirty nodes per hidden layer, and one output node. The inputs used are the same as described in Section 5.1 when such parameters are available for the reconstructed τ lepton candidate with an additional parameter of lateral impact parameter significance when available.

Figure 5.11 gives the discriminant distributions for the signal and background along with the significance. Unlike the likelihood significance no local maximum gives the best significance. This behavior is to be expected as the neural net is trained to provide the best significance for a discriminant of one. If such a behavior does not occur the neural net is not trained to significance but rather some other metric.

From the left plot of Figure 5.11 it appears as if the neural net is over trained, as a large number of events are assigned a value of zero. This however is not the case, as many of these events have no associated tracks and were reconstructed using only calorimetry information. Candidates with only calorimetric information cannot have a discriminant assigned and are assigned a default value of zero. This behavior is verified in the background distribution where few events are assigned a discriminant value over 0.4.

Using the "loose", "medium", and "tight" discriminant cuts previously discussed, efficiency and fakerate plots are given in Figure 5.12. Note that the "loose" total efficiency is slightly lower than the "loose" efficiency for the cut flow method as all candidates reconstructed with only calorimetry information are necessarily discarded. Consequently the maximum efficiency attainable using the neural net method is slightly below the total efficiency of the likelihood method for a discriminant of "loose".

The neural net has a stronger immediate turn on than the likelihood, but then gradually increases to a peak efficiency near 40 GeV. For high p_T the efficiency drops significantly more than in the case of the likelihood. Such a behavior could prove problematic for massive Higgs searches with a di-τ lepton decay product, where the two τ leptons have large p_T. The efficiency

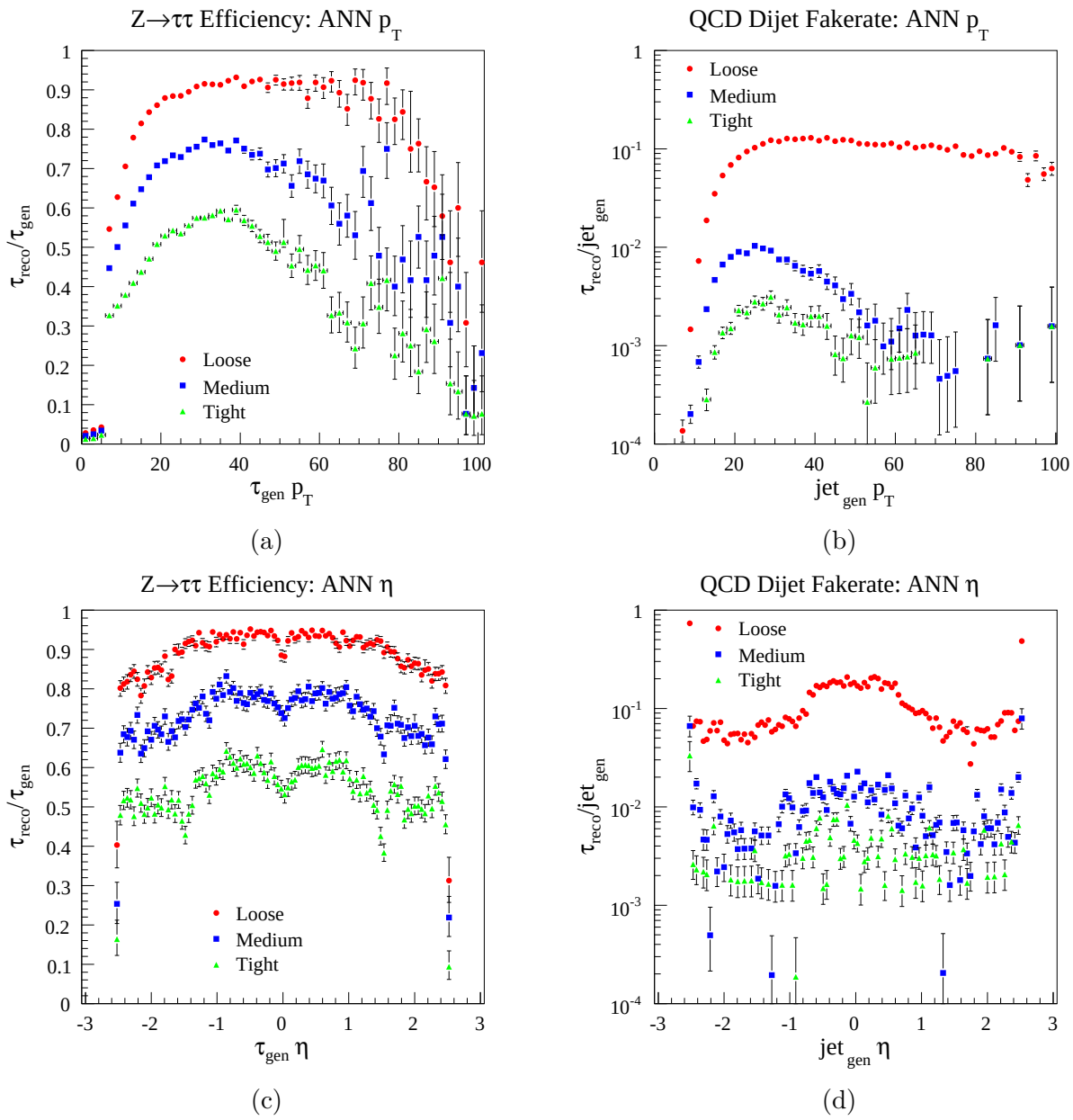

Figure 5.12: Efficiencies for the artificial neural net identification method are given in (a) and (c) while equivalent fakerates are given in (b) and (d).

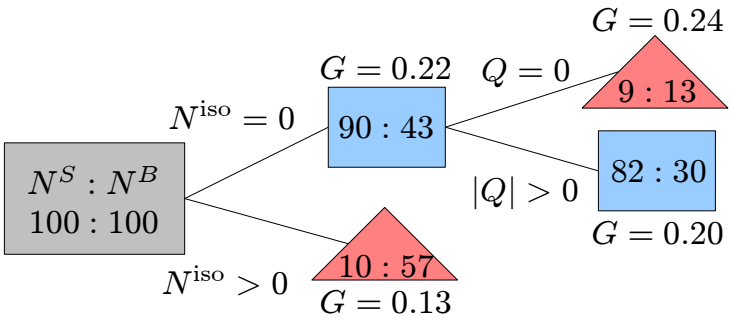

Figure 5.13: Schematic of a simple decision tree. Blue indicates a signal dominated branch/leaf while red indicates background. Rectangles represent branches, triangles represent terminating leaves. For this tree branches were terminated for $G < 0.16$ corresponding to an 80% purity and when less than 25 events were remaining in the sample. The first discriminating variable is number of isolation tracks and the optimal value is found to be 0. The second variable is charge with a value of 0 chosen for separation.

and fakerate both have structure in η, again corresponding to a combination of various detector effects. The sharp drop in efficiency for $\eta = 0$ most probably indicates that in this region the electromagnetic calorimeter variables are more heavily weighted than the inner detector variables.

5.2.4 Boosted Decision Tree

Boosted decision trees provide yet another method with which to discriminate signal from background, but are particularly well suited to the type of problem presented by τ lepton identification. In general, boosted decision trees perform well on discriminating signal from background in cases where the variables are weak, and no single cut has a clear advantage. This is the case for τ lepton identification; certain variables clearly have greater discriminating power such as the isolation fraction, but no single variable provides a definitive separation.

Not only do boosted decision trees perform well on weakly discriminating variables but they can be trained quickly without the danger of over training, as is the case with neural nets. The addition of variables does not destabilize the method, unlike neural nets where additional input nodes can cause a destabilized algorithm. In general, boosted decision trees provide a stable, fast, and transparent method by which to determine the optimal weighting of weakly discriminating variables. Further details on the mathematical framework of boosted decision trees can be found in References [74] and [75].

Using a boosted decision tree consists of two steps which are iterated over until stability for the tree is achieved. First a decision tree is built as shown in Figure 5.13. This process begins with a sample of background and signal with a specified number of discriminating variables. The discriminating variables are arbitrarily ordered, although changing the order can cause instability if boosting is not convergent. A decision is then made on which value to cut for the first variable. This decision can be through a variety of methods, but for ATLAS, the value selected minimizes the sum of the Gini index, as defined in Equation 5.10, of the two daughter branches [76].

$$G \equiv P(1 - P) \tag{5.10}$$

The Gini index reflects the separation of the sample and is based on the purity of the sample, given by Equation 5.11 where the sum of each weighted signal event is divided by the weighted sum of all events.

$$P \equiv \frac{\sum_S w_i N_i}{\sum_S w_i N_i + \sum_B w_i N_i} \tag{5.11}$$

In the initial decision tree the weight for each event, w_i, is set to one over the number of events, as no boosting has yet occurred and this normalizes the total number of events. A Gini index of zero corresponds to a sample that is either all signal or background, while a maximum index of one quarter corresponds to a sample of equally mixed signal and background [77].

After a value has been chosen, the sample is split into two branches, one that passes the cut and one that fails. A value for the next discriminating value is then determined for each branch again by using the Gini index. This process continues, with the number of branches doubling for each discriminating value assuming no terminating branches. A branch terminates with a leaf if the number of events left within the sample is below a threshold value, or if the Gini index calculated for that particular sample is below a cutoff. The building of the decision tree is terminated when all branches have reached one of the two thresholds, number of events or Gini index, or when no more discriminating variables are available.

After the decision tree has been built, the tree is boosted. This boosting can be performed through a variety of techniques, but ATLAS employs adaptive boosting (AdaBoost) [76]. For this method a weight is assigned to each event, with the weight increasing for misplaced events, signal events placed on a background leaf or background events placed on a signal leaf. Assume a sample of N events with a vector of discriminating variables $\vec{d_i}$ for the ith event. The type of the event is given by t_i where a value of 1 indicates signal and a value of -1 indicates background. If the set of discriminating variables $\vec{d_i}$ for the ith event place the event on a signal leaf the classifier $T_m(\vec{d_i})$ is defined to equal 1 where m indicates the mth tree built. Similarly, if $\vec{d_i}$ places the event on a background leaf, $T_m(\vec{d_i}) = -1$.

The misclassification rate ϵ_m for the mth tree built is given by Equation 5.12 where $\delta(t_i, T_m(\vec{d_i}))$ is a Dirac delta function such that it is zero when $t_i = T_m(\vec{d_i})$ and one when $t_i \neq T_m(\vec{d_i})$ [77]. Effectively this delta function assigns a value of zero for properly placed events, and a value of one for misplaced events. The misclassification rate is required to be less than 0.5 as this prevents the decision tree weighting from diverging.

$$\epsilon_m \equiv \frac{\sum_i w_i \delta(t_i, T_m(\vec{d_i}))}{\sum_i w_i} < 0.5 \tag{5.12}$$

The weighting for the mth decision tree, α_m, is defined by Equation 5.13 where β is a constant parameter for all events and trees. Traditionally β is set to 0.5 as is done within the original proposal of AdaBoost [75].

$$\alpha_m \equiv \beta \ln\left(\frac{1-\epsilon_m}{\epsilon_m}\right) \tag{5.13}$$

The weight of the ith event for the mth decision tree is then given by Equation 5.14.

$$w_{i,m+1} = w_{i,m} e^{\alpha_m \delta(t_i, T_m(\vec{d_i}))} \tag{5.14}$$

All events that are properly placed do not have their weights from the previous decision tree altered while misplaced events have their weights increased. From the logarithmic form of ϵ_m it can be seen that the relative weighting of misclassified events with respect to properly classified events increases to infinity for the limit of zero misclassified events. The parameter β decreases the slope for the asymptotic behavior of α_m with respect to ϵ_m and can be adjusted to control

the relative weighting scheme. After the weighting for the mth event is determined the weights are all renormalized.

The classifier for an event with discriminating variables $\vec{d}$ is given by the sum of the classifiers $T_m(\vec{d})$ multiplied by the corresponding weight, α_m, for each decision tree and normalized [77].

$$T(\vec{d}) = \frac{\sum_m \alpha_m T_m(\vec{d})}{\sum_m \alpha_m} \tag{5.15}$$

The classifier of Equation 5.15 can range from a value of -1 corresponding to a background event, to a value of 1 corresponding to a signal event. A value of 0 is an event that is equally likely to be signal or background. Oftentimes the classifier is adjusted to range from 0 to 1 as this format is similar to the discriminants of ANN's and likelihoods.

From the nature of decision trees, as can be seen in Figure 5.13, the boosted decision tree method suffers from inherent limitations, which while somewhat avoidable, do diminish the effectiveness of the method. This arises from the necessary binary decisions at the splitting of a branch. The problem arising from this can be seen in the example of number of tracks within the signal cone of a τ lepton candidate. From Section 2.2.1 it is clear that for an actual τ lepton this discriminating variable is physically required to be 1, 3, or 5. This causes a problem for the decision tree as it cannot take advantage of this kinematic reality. The user can specify that such a decision should be made on whether the number of signal tracks is within this kinematic basis. However, the automation of the entire system is destroyed by such a choice on the part of the user and introduces further complications. Another possible workaround would be to allow multiple decisions on the same variable, but again, this introduces complications.

Such complications require that the user carefully choose the discriminating variables used for the decision tree. Oftentimes issues such as the one described above can be avoided by mapping the discriminating variables to a new value. Such re-mapping of variables must be done with care, as this can introduce user bias into the optimization process. The parameter space of discriminating variables used by ATLAS for the τ lepton identification boosted decision trees is very complex, and as such is not reported here. A full description can be found in Reference [76].

Unlike ANN's, boosted decision trees are not susceptible to over training, assuming the method described above without multiple splittings on a signal discriminating variable. This provides a distinct advantage of the boosted decision tree over ANN's. Additionally, the cuts applied through the decision tree are very transparent and the behavior of the tree can be easily traced in direct contrast to the convolution of sigmoid functions used by ANN's. Boosted decision trees, however, do take into account the correlation of variables, and as such, can provide an advantage over the likelihood method.

The distribution of signal and background events along with the significance is given with respect to the discriminant for the boosted decision tree method in Figure 5.14. Neither of the distributions are smooth, but have distinct structures. These occur as the method is not continuous like the ANN or likelihood methods, but rather made from a series of binary decisions represented by the trees. These individual decisions are washed out by the boosting, but structure still remains.

The maximum significance attained by the boosted decision tree method is ≈ 0.09 which while it outperforms a simple cut based analysis does not match the levels attained by either the likelihood method or ANN method. Whether this lack of performance is due to improper training implementation or rather an inherent mismatch of problem and method is unknown without further investigation.

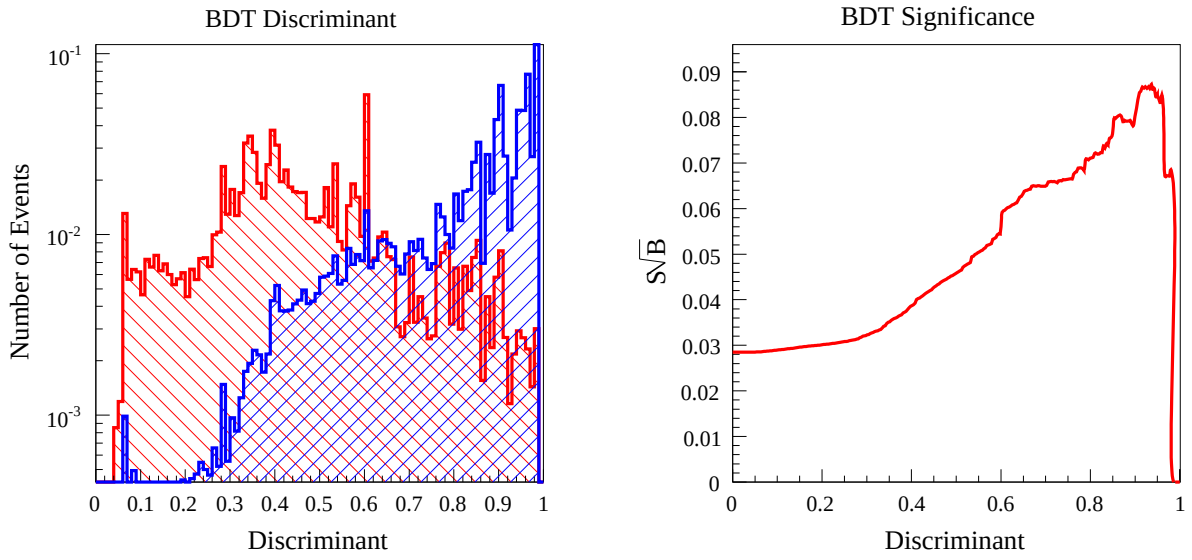

(a) (b)

Figure 5.14: Distributions of the normalized number of events and significance with respect to the discriminant for the boosted decision tree identification method.

The efficiency and fakerate plots for the boosted decision tree method are given in Figure 5.15. Unlike both the ANN and likelihood, the efficiency increases with high p_T and the turn on is very sharp. This increase in efficiency with respect to p_T in combination with the very flat behavior of the fakerate for high p_T indicates that the boosted decision tree identification method while not optimal for Z identification could provide a better handle on high p_T regions than either the ANN or likelihood.

A distinct structure is again seen in the η distributions, as expected. Now however drops appear at $\eta \approx 1$ corresponding to gaps within the inner detector as can be see in Figure 3.6. This indicates that inner detector variables are favored over calorimeter variables.

5.3 Comparison

Before making definitive comparison statements it is important to remember that these comparisons are not global but rather very specific to the signal sample, background sample, and p_T range used within the context of this analysis. By example, switching the signal sample to a heavy SM Higgs decay and by considering a higher p_T range, the BDT method could very well perform significantly better and even outperform the likelihood and ANN methods.

Keeping the context of this analysis in mind, Figure 5.16 provide a plot of the four methods' total fakerates versus efficiencies. Note that while error is not included for clarity, these values still have significant error associated to them. For total efficiencies less than $\approx 73\%$ the ANN outperforms both the likelihood and the ANN. Notice that the ANN does not exceed efficiencies greater than $\approx 90\%$; this is again due to the ANN using only track seeded τ lepton candidates.

For values greater than 73% the likelihood outperforms the other methods. For the ANN this is expected due to the inherent properties of the algorithm used. The boosted decision tree under performs both the likelihood and ANN for nearly all efficiencies except for a very small portion

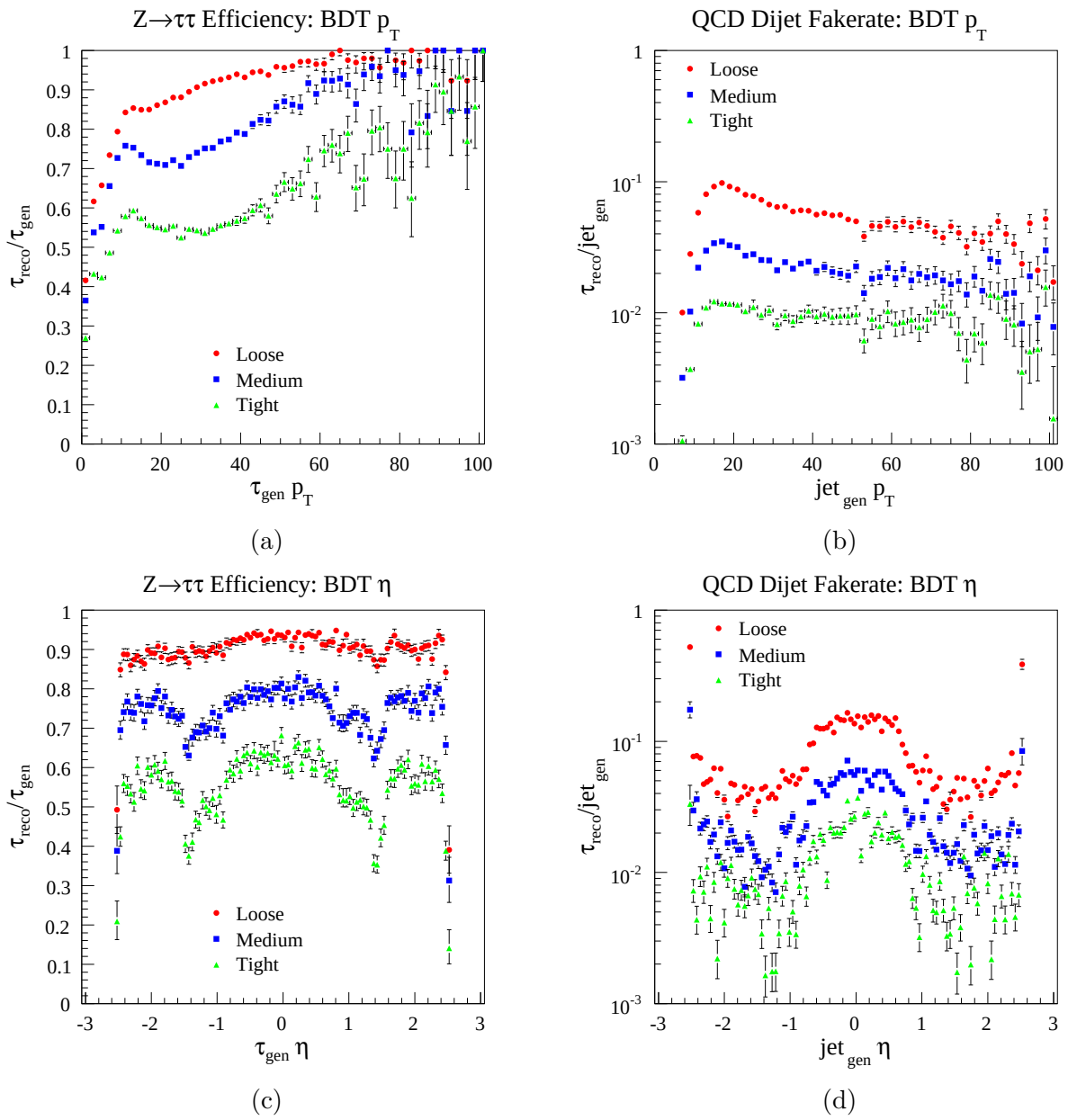

Figure 5.15: Efficiencies for the boosted decision tree identification method are given in (a) and (c) while equivalent fakerates are given in (b) and (d).

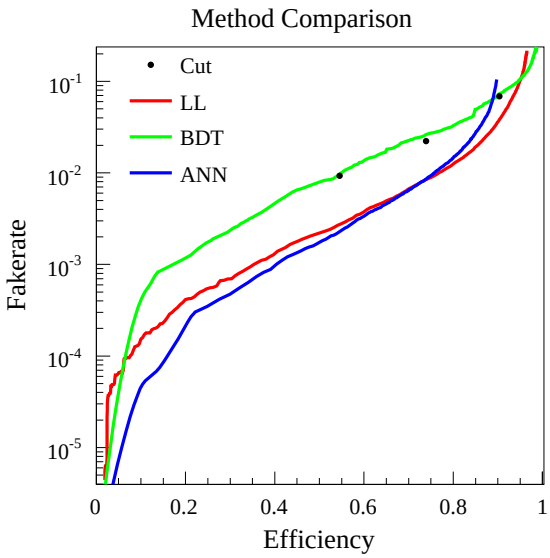

Figure 5.16: Comparison of efficiency versus fakerate for the four identification methods outlined in Section 5.2.

in the high efficiency range, and nearly matches the three discrete cut flow definitions. For a general Z analysis using hadronic τ leptons the ANN appears to provide the best identification method of the three described above.

6 Tau Lepton Efficiency in Data

Determining τ lepton identification efficiency from actual data with no generator level information available is a unique challenge but can be estimated from data using a variety of techniques. Obtaining such an efficiency measurement is important for physics searches involving the hadronic τ lepton so that accurate cross sections can be calculated. The following chapter is not intended as a comprehensive study, but rather an initial discussion of the subtleties involved in hadronic τ lepton efficiency measurement from data.

6.1 Total Efficiency

A brief outline of the method for determining a total hadronic τ lepton efficiency is given followed by a discussion of a simple implementation and the problems encountered during implementation.

6.1.1 Method

The proposed method is similar to that of Reference [78] and begins by assuming that the efficiency of muon identification within the detector is well known for the $Z \rightarrow \mu\mu$ process. This is a reasonable assumption, as muon studies will be among the first feasible studies on preliminary data, and analyses including hadronic τ leptons will not be feasible until a full understanding of the detector is gained from preliminary studies.

Keeping this in mind the method begins by requiring a sample is gathered by triggering on an isolated muon and the integrated luminosity of the sample is known. Events are then selected where a single isolated muon is found and a single isolated hadronic τ lepton of some predetermined quality cut is also found. These events are divided into events where the muon and hadronic τ lepton both have the same sign, N^{SS}, and events where the muon and hadronic τ lepton have opposite signs, N^{OS}. In a reasonable first guess it is assumed that all events with the same sign are necessarily background events, and additionally that the background has equal likelihood to produce a same sign and opposite sign event. The efficiency for hadronic τ lepton identification is then given by Equation 6.1.

$$\varepsilon_\tau = \frac{N^{OS} - (f+1)N^{SS}}{\varepsilon_\mu A \mathscr{L}_{\text{int}} \sigma_Z BR(Z \rightarrow \tau\tau) BR(\tau \rightarrow \mu) BR(\tau \rightarrow \hbar)} \tag{6.1}$$

Here ε_μ is the total efficiency for muons from *a priori* knowledge of the $Z \rightarrow \mu\mu$ process, this includes trigger efficiencies, A is the detector acceptance, σ_Z is the cross section of the Z boson at the LHC for the specific operation conditions of the data sample, $\mathscr{L}_{\text{int}}$ is the integrated luminosity for the sample, and the BR's are the various branching ratios of the Z and τ lepton known to high precision from previous experiments. The value f is the ratio between opposite sign and same sign background events and in this first scenario is taken to be 1.

However the number of $Z \rightarrow \mu\mu$ events can be reliably measured from data and is written in Equation 6.2. Here, $BR(Z \rightarrow \tau\tau)$ is taken to taken to be equal to $BR(Z \rightarrow \mu\mu)$.

$$N^{\mu\mu} = \varepsilon_\mu^2 A \mathscr{L}_{\text{int}} \sigma_Z BR(Z \rightarrow \tau\tau) \tag{6.2}$$

Placing this expression back into Equation 6.1 provides Equation 6.3 which eliminates A, $\mathscr{L}_{\text{int}}$, σ_Z, $BR(Z \to \tau\tau)$, and their associated errors.

$$\varepsilon_\tau = \frac{\varepsilon_\mu \left(N^{OS} - (f+1)N^{SS}\right)}{N^{\mu\mu} BR(\tau \to \mu) BR(\tau \to \hbar)} \tag{6.3}$$

The first problem to note from Equation 6.3 is that taking a total efficiency directly from a $Z \to \mu\mu$ process is not the same as taking the integrated efficiency from a $Z \to \mu\bar{\nu}_\mu\nu_\tau\tau_\hbar\nu_\tau$ process as there is an average downward p_T shift in the $Z \to \mu\tau_\hbar$ distribution attributed to the difference between a two and a three-body decay.

Because the muon efficiency has a turn on, as can be seen in Figure 6.1, the average downward shift of p_T within the distribution for $Z \to \mu\tau_\hbar$ must be taken into account. This can be done by taking an efficiency distribution with respect to p_T for the $Z \to \mu\mu$ process and multiplying this by the p_T event distribution for signal muons from the $Z \to \mu\tau_\hbar$ sample from tuned Monte Carlo. The distribution is summed and then divided by the initial number of events to provide the corrected total efficiency.

The next issue of Equation 6.3 is the assumption that $f = 1$, or that there is a one to one correspondence between background events with same sign and opposite sign. To fully understand this ratio one must first understand the relevant backgrounds that provide a real or fake muon and hadronic τ lepton. From the SM, three processes provide a considerable background contribution: top pair production, W boson plus jets production, and bottom quark pair production. Table 6.1 gives the cross sections for these processes along with the $Z \to \mu\tau_\hbar$ process.

Process	Cross Section [pb]
$Z \to \mu\tau_\hbar$	302.3
W + jets	5943.17
$t\bar{t}$	373.6
$b\bar{b}$	8.85×10^4

Table 6.1: Cross sections for the signal process used and corresponding relevant backgrounds for hadronic τ lepton efficiency calculation for a pp collision with $\sqrt{s} = 10$ TeV [79].

For all of these background processes it can be hypothesized as to the correlation between same sign and opposite events, but it is simplest to extract this information from tuned Monte Carlo. As the Monte Carlo and its relation to data should be well understood by the time a τ lepton efficiency study is being performed, the extraction of a scale factor f should yield a result with low systematic error, and should provide a better factor than the assumption of a one to one ratio.

The final issue at hand regarding Equation 6.3 is the possibility of actual signal events providing a same sign event. Not only this, but the possibility of a hadronic τ lepton being faked by either muon or electron will bias the efficiency measurement and must also be considered. These issues will be explored in more detail in the following section.

A simple implementation of the method described above was performed to investigate the feasibility of such a study on real data. For this study three Monte Carlo samples were used: a $Z \to \mu\mu$ sample, a $Z \to \tau\tau$ sample, and a $b\bar{b}$ sample all described in Appendix A.

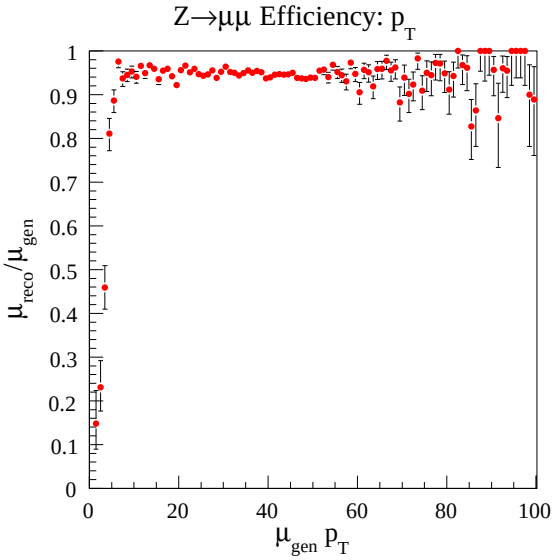

Figure 6.1: Muon efficiency using Monte Carlo generator level information and STACO reconstructed muons with a "best match" tag and isolation < 5 GeV.

6.1.2 Muon Efficiency

Within ATLAS two algorithms are used for muon reconstruction, STACO (STAtiscial COmbination) and Muid [26]. For this study STACO muons were used, as this is the default muon reconstruction choice. Muon tracks are reconstructed in the muon spectrometer and extrapolated to the vertex of the event. Tracks within the inner detector are also reconstructed and matched against the extrapolated muon tracks from the muon spectrometers. If a match passes a specified criteria the two tracks are statistically combined to provide a reconstructed muon object. If the object was the best match between muon spectrometer and inner detector tracks it is labeled as such [80].

The muon efficiency can be calculated from actual data using a variety of techniques some of which are outlined in Reference [81]. For the purpose of this implementation these studies are assumed to have already been performed, and so the muon efficiency was calculated from the $Z \rightarrow \mu\mu$ sample using generator level information. Reconstructed muons labeled as "best match" with an isolation energy of less than 5 GeV were matched against generator level muons with a cone of $\Delta R = 0.2$. All reconstructed muons that passed these cuts were considered identified and were divided by the number of generator level muons. The efficiency of the selected reconstructed muons with respect to p_T is given by Figure 6.1.

6.1.3 Charge Misreconstruction

Before implementing the method described above it is critical to validate the assumption that all signal events will necessarily have an opposite sign muon and τ lepton. Table 6.2 gives a table of the cut flow used, and the relative percentages of same sign and opposite sign reconstructed signal events. The first cut is a general cut to ensure that both the muon and hadronic τ lepton are of good quality. This is done for the muon by requiring an energy of less than 5 GeV deposited within its isolation cone. Additionally the muon is required to be a "best match" as

described previously.

Cut	Same Sign [%]	Opposite Sign [%]
Iso(μ) < 5 GeV, "μ best match", $D_{\mathrm{ANN}}(\tau_{\hbar}) > 0.9$, Charge($\tau_{\hbar}$) $= \pm 1$	$74.15^{+0.45}_{-0.45}$	$25.84^{+0.45}_{-0.45}$
$\Delta R(\mu, \tau_{\hbar}) > 0.2$	$95.06^{+0.25}_{-0.26}$	$4.94^{+0.26}_{-0.25}$
$\Delta R(\tau_{\mathrm{gen}}, \tau_{\hbar}) < 0.2$	$95.88^{+0.25}_{-0.26}$	$4.12^{+0.26}_{-0.25}$

Table 6.2: Cut flow and corresponding same/opposite sign event precentages using only the signal Monte Carlo sample described in Appendix A.

Two requirements are placed on the hadronic τ candidate. The first cut requires that the τ lepton candidate is of high quality by using the ANN method discussed in Section 5.2.3 as this provides the best signal to background signficance. The second cut placed on the τ lepton candidate is that the charge must be plus or minus one. This cut is necessary as τ lepton candidates can be reconstructed with charges of other than one, which is incompatible with the same/opposite sign method for seperating signal and background.

After the quality cut for the muon and τ lepton, along with the requirement that only one muon and hadronic τ lepton are in the event, the opposite sign percentage is 74% while the same sign percentage is 26%. This large percentage of same sign events can be accounted for by muons being reconstructed as hadronic τ leptons. To remedy this problem the second cut is applied, requiring a seperation of $\Delta R > 0.2$ between the muon and hadronic τ lepton. This cut ensures that the muon is not being misreconstructed as a hadronic τ lepton. In general this problem can be avoided by treating an event constistantly and allowing an object to be identified only once.

This does not, however, entirely solve the problem with 95% of events opposite sign and 5% of events same sign. This difference can be attributed to either faking hadronic τ leptons, which correspond to no underlying generator hadronic τ lepton, or to charge misreconstruction of the hadronic τ lepton. To determine the cause of this 5% same sign events the hadronic τ lepton candidates were required to match a generator level hadronic τ lepton using a matching cone of $\Delta R = 0.2$. As can be seen, this reduces the percentage of same sign events by less than 1% implying that the cause for the remaining 5% of same sign events is entirely from misrecontruction of the hadronic τ lepton charge.

For the above method to provide meaningful results this charge misreconstruction must be accounted for. Using Monte Carlo, as was done for this study, it is of course possible to estimate the percentage of same sign events, in this case, 4.9%. This method for accounting for charge misreconstruction requires that the Monte Carlo models the data well but also introduces another systematic error to the efficiency.

Another method to verify the same sign event percentage given by Monte Carlo is to use inner detector properties measured from data alone. The charge of the hadronic τ lepton candidate is determined from inner detector information alone and subsequently the misreconstruction can be attributed to track reconstruction and hadronic τ lepton reconstruction within the inner detector.

The left plot of Figure 6.2 demonstrates the percentage of generator level matched τ lepton candidates with a properly reconstructed charge over the total number of matched τ lepton candidates with a charge of ± 1. For very low p_T a dip can be seen that can most probably be attributed to three prong hadronic decays where two tracks of the same sign are not reconstructed. The decrease in efficiency for higher p_T is not readily apparent without further investigation.

By fully examining the track misconstruction combinations and their subsequent possibilities of charge misreconstruction discussed above it would be possible to estimate hadronic τ lepton charge misreconstruction using inner detector charge misrecontruction and track reconstruction data. Such a detailed study is not performed here, but is merely mentioned to highlight the difficulties that must be considered with respect to hadronic τ lepton charge misreconstruction.

6.1.4 Electron Misidentification

When outlining the possible background available to the $Z \rightarrow \mu\tau_h$ channel, the background $Z \rightarrow \mu e$ was not mentioned, as an electron should not be misreconstructed as a hadronic τ lepton. Unfortunately, this is not the case with ATLAS hadronic τ lepton reconstruction, where a large number of electrons are reconstructed as hadronic τ leptons. Because of this misreconstruction a cut must be applied to the cut flow of Table 6.2 to ensure that the $Z \rightarrow \mu e$ background is not included in the selection of the $Z \rightarrow \mu\tau_h$ signal.

A variety of identification methods are available for electron reconstruction similar to those outlined for hadronic τ lepton reconstruction in Section 5.2 [26]. Combining the variables from electron reconstruction with the variables from hadronic τ lepton reconstruction, an electron likelihood veto was calculated for every reconstructed hadronic τ lepton candidate after passing the first and second cuts of Table 6.2. Each candidate was then matched against generator level information to determine whether the selected candidate corresponded to an electron or hadronic τ lepton jet. The electron likelihood for both the candidates matched with electrons and matched with hadronic τ leptons is given in the left plot of Figure 6.2.

As can be seen, placing a cut requiring the electron likelihood veto to be greater than zero provides an excellent seperation between actual hadronic τ leptons and faking electrons. Table 6.3 gives the percentage of faking electrons before and after the electron likelihood veto cut for both same sign and opposite sign events. With the veto in place, the contamination from electron events is reduced to less than 1% of the entire sample. While this is much smaller than the error attributed to charge misreconstruction, faking electrons must still be taken into account.

Cut	Electron Same Sign [%]	Electron Opposite Sign [%]
No Electron Veto	$14.74^{+0.39}_{-0.39}$	$11.2^{+1.6}_{-1.5}$
Electron Veto(τ_h) > 0	$0.66^{+0.11}_{-0.10}$	$1.07^{+0.76}_{-0.51}$

Table 6.3: Cut flow for electron rejection and corresponding same/opposite sign event precentages using only the signal Monte Carlo sample described in Appendix A.

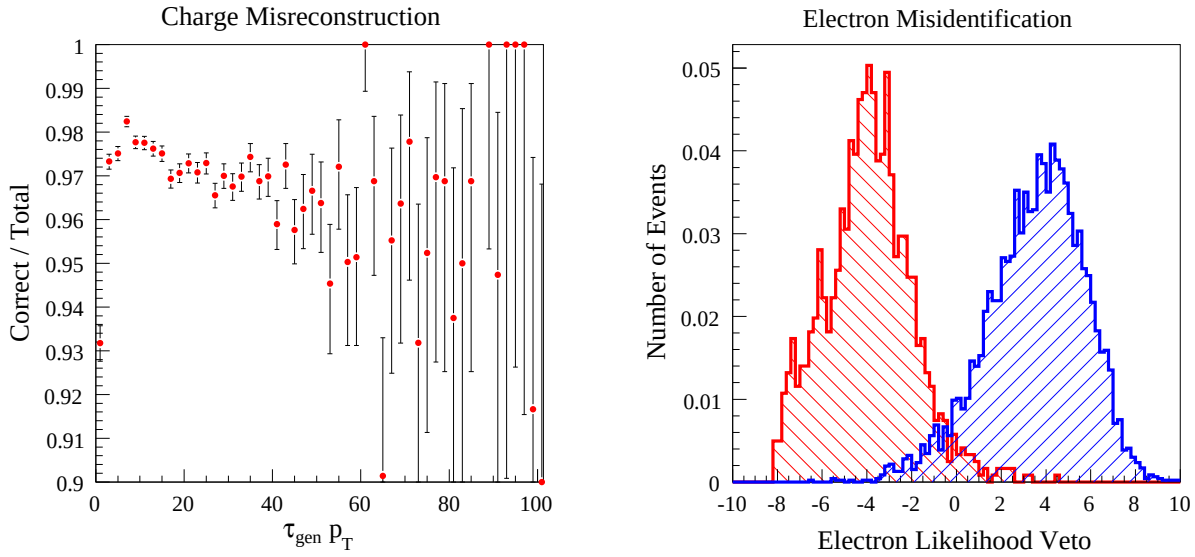

(a) (b)

Figure 6.2: Percent of matched hadronic τ lepton candidates with correct charge is given in (a). Electron likelihood veto for reconstructed hadronic τ lepton candidates passing the first cut of Table 6.2 matched against generator level hadronic τ leptons (blue) and generator level electrons (red) is given in (b). The distributions of (b) were normalized to an integral of one.

6.1.5 Background Estimation

While the correlation between same sign and opposite sign events should be calculated using an inclusive sample, such a sample was not available at the time of writing, and so only a $b\bar{b}$ sample as described in Appendix A was used. Using the first two cuts of Table 6.2 and the second cut of Table 6.3, opposite sign to same sign ratios were found. The ratio of opposite sign to same sign background events for the $b\bar{b}$ could be dependent upon p_T of the event, but as only a small background sample was available distributions for this ratio could not be made with respect to p_T. Integrating over all p_T available within the background sample an opposite sign to same sign ratio of 1.17 ± 0.12 was found.

6.1.6 Results

The integrated efficiency from the distribution of Figure 6.1 is $94.46 \pm 0.11\%$. This efficiency now needs to be scaled with respect to the p_T distribution of opposite sign signal events. While such a distribution is not available from data, it can be modeled relatively well by Monte Carlo. The left plot of Figure 6.3 shows the probability density function of reconstructed muons using the first two cuts of Table 6.2 and the last cut of Table 6.3. This distribution is then multiplied by the efficiency plot of Figure 6.1 to obtain the right plot of Figure 6.3. This distribution is integrated over to obtain the properly adjust efficiency which is $90.07 \pm 0.11\%$. The error on this adjusted efficiency only takes into account statistics of the Monte Carlo without considering systematic uncertainty.

Using Equation 6.3 the hadronic τ lepton identification efficiency can be calculated to be $\varepsilon_\tau = 17.3 \pm 2.1\%$ using the numbers from Table 6.4. Note that the error here is only from

Variable	Value
N^{OS}	5574 events
N^{SS}	379 events
f	1.17 ± 0.12
ε_μ	90.01 ± 0.11
$\mathscr{L}_{\text{int}}\sigma_{Z\to\mu\tau_h}$	32990 events

Table 6.4: Values for the variables of Equation 6.3 using the Monte Carlo samples described in Appendix A and normalized to an integrated luminosity of 200 pb^{-1}, the expected data after the $2009-2010$ data run [82].

statistical uncertainty due to the Monte Carlo size. Due to the lack of statistics in the available samples the numbers of Table 6.4 were calculated using the same Monte Carlo samples used for estimating f and ε_μ. As such, there is direct agreemant between the efficiency measured using Equation 6.3 and the actual efficiency measured from Monte Carlo. For a more detailed analysis on possible error estimation, Reference [78] provides an excellent resource. The leading systematic error term however is from calorimetery scale uncertainty and is estimated to be on the order of $\approx 8\%$.

6.2 Efficiency Versus p_T

While obtaining an overall efficiency for hadronic τ lepton reconstruction is important, it is also important to parameterize the efficiency as a function of p_T (and η) for the hadronic τ lepton. Determining this efficiency distribution however, is even more challenging than determining total efficiency. If the p_T distribution of muons from τ leptons was the same as for the visible product of hadronic τ lepton decays, calculating an efficiency with respect to p_T would just require implementing a method similar to a total efficiency calculation, but with large statistics and taking p_T into account. However, the muon and hadronic τ lepton efficiencies are not the same as can be seen in Figure 6.4. Here the p_T probability density functions are plotted for the decay products of $Z \to \mu\tau_h$ events. The following section briefly explores the physics behind momentum shift and methods by which an efficiency distribution for hadronic τ lepton identification can be made with respect to p_T.

6.2.1 Momentum Shift

The shift of the expected values from the probability density functions of Figure 6.4 are understood by taking into account that a τ lepton decay into a muon, muon neutrino, and τ lepton neutrino is a three-body decay, while hadronic τ lepton decays are a variety of N-body decays. The decay channels for the τ lepton have been measured to a relatively high precision, and so the calculation of the difference between the expected transverse momentum fraction carried by the muon, or visible hadronic decay products with respect to the total τ lepton p_T, can be calculated directly from theory. This calculation however is somewhat involved, and so calculating expected values from a large amount of Monte Carlo generator level information is simpler. The Monte Carlo results are approximated using probability theory to give the reader an intuitive feel for the underlying physics.

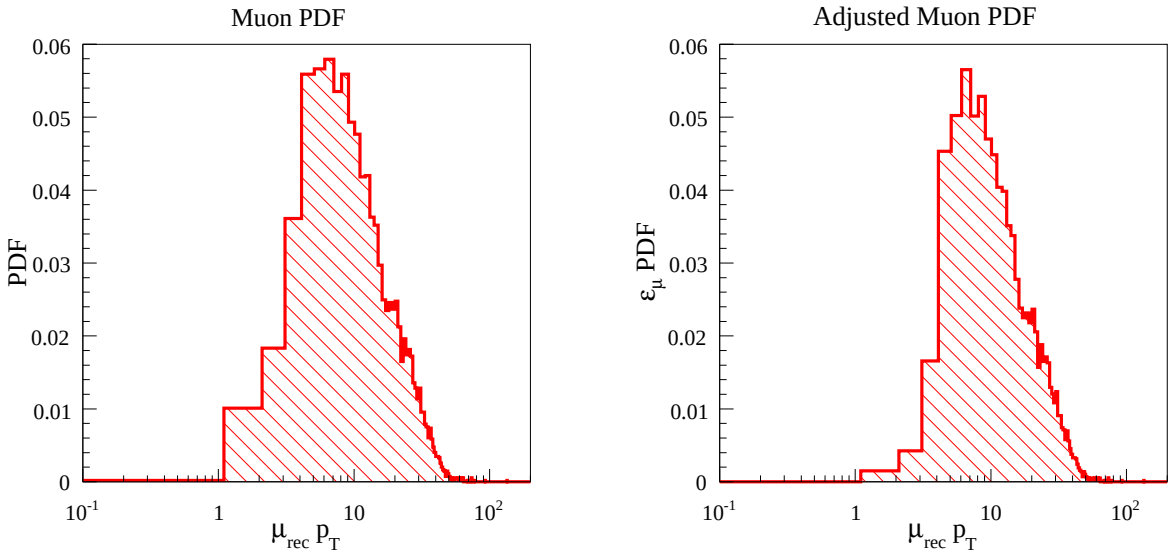

(a) (b)

Figure 6.3: The Monte Carlo p_T probability density function for reconstructed muons from a $Z \rightarrow \mu\tau_h$ event is given by (a). The distribution is adjusted by multiplying (a) by the efficiency of Figure 6.1 to obtain (b). The integral of this distrution yields the adjusted efficiency for muon reconstruction.

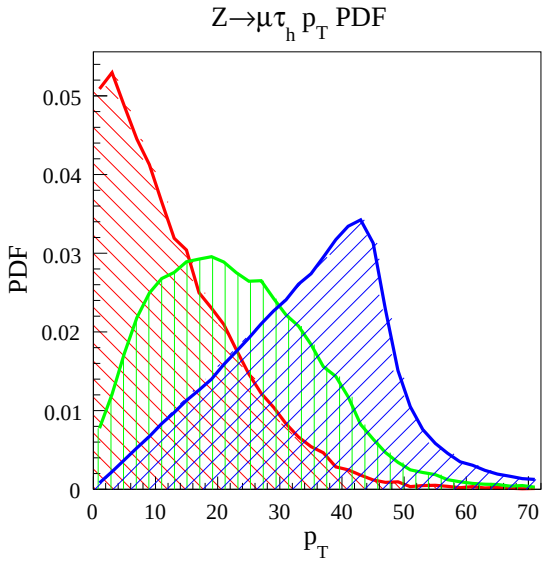

Figure 6.4: Probability density functions with respect to p_T are given for the intermediate τ lepton (blue), the visible hadronic τ lepton (green), and the muon (red) for a $Z \rightarrow \mu\tau_h$ event.

This problem is similar to the two-body decay discussed earlier in Section 4.3, but now must be done for N-body decays. For the case of a two-body decay it is clear from intuition that the expected energy of each of the two decay products must be half the energy of the parent. This is achieved by allowing the probability density function for either decay child to be represented by a uniform distribution as given in Equation 6.4 where x is the energy of the decay child and E is the energy of the parent.

$$f_2(x) = \frac{1}{E} \tag{6.4}$$

Such a uniform distribution is properly normalized, $\int_0^E = 1$, and the expected energy for either decay product is $E/2$, $\int_0^E x f_2(x)\, dx = E/2$.

Expanding to a three-body decay a similar approach can be taken. Notice that if the energy of two of the three decay products is chosen, the third value is uniquely determined. Keeping this in mind the probability density function for the energy of a decay product from a three-body decay can be written as is done in Equation 6.5. Here the probability of finding a particle with energy x is still given by the uniform distribution. However, this probability must be multiplied by the probability that the second particle has an energy less than x, which is just one less the cumulative probability distribution up to the value x. Finally, this quantity must be multiplied by two to take into account the available permutations.

$$f_3(x) = 2\left(\frac{1}{E}\right)\left(1 - \frac{x}{E}\right) \tag{6.5}$$

Notice that the distribution is still normalized, $\int_0^E f_3(x)\, dx = 1$ and the expectation value is $E/3$, $\int_0^E x f_3(x)\, dx = E/3$. By generalizing the reasoning used for the three-body decay, it is possible to write the energy probability density function for a product of an N-body decay. The uniform distribution is still used, but now is multiplied $N-2$ times by $1 - x/E$. Furthermore, the permutation factor $N-1$ must be taken account. Combining these together yields Equation 6.6.

$$f_N(x) = \frac{N-1}{E}\left(1 - \frac{x}{E}\right)^{N-2} \tag{6.6}$$

Applying this to a p_T distribution now requires that the mass of the decay products is taken into account. Once this is done, the probability density function for E can be transformed to the variable p_T as the relation between the two variables, $m^2 = E_T^2 - p_T^2$ is known and E_T, just as E, must be conserved. However, when calculating the expected value for the p_T carried by a muon from a τ lepton decay with $p_T > 1$ GeV the mass of the muon can be neglected for a simple approximation. As such, the expected p_T is just given by Equation 6.5 which yields $p_T/3$ where p_T is the transverse momentum of the parent τ lepton.

For the case of a hadronic decay the approximation that the constituents are massless is less accurate, but still yields a reasonable result, especially for high p_T. Consider now the expected p_T of the τ lepton neutrino in a hadronic decay; the probability density function for the hadronic portion of the τ lepton is then just the normalized inverse of the τ lepton neutrino probability density function.

However, the τ lepton can decay through a variety of hadronic channels. What is important is the number of final decay products and the probability of that specific decay occurring. Table 6.5 shows a breakdown of the N-body decay percentages for one prong and three prong hadronic τ lepton decays normalized such that the total is one.

N-bodies	one prong	three prong
2	0.18	0
3	0.41	0
4	0.15	0.16
5	0.02	0.08

Table 6.5: Table demonstrating the number of decay products for one and three prong hadronic τ lepton decays [18].

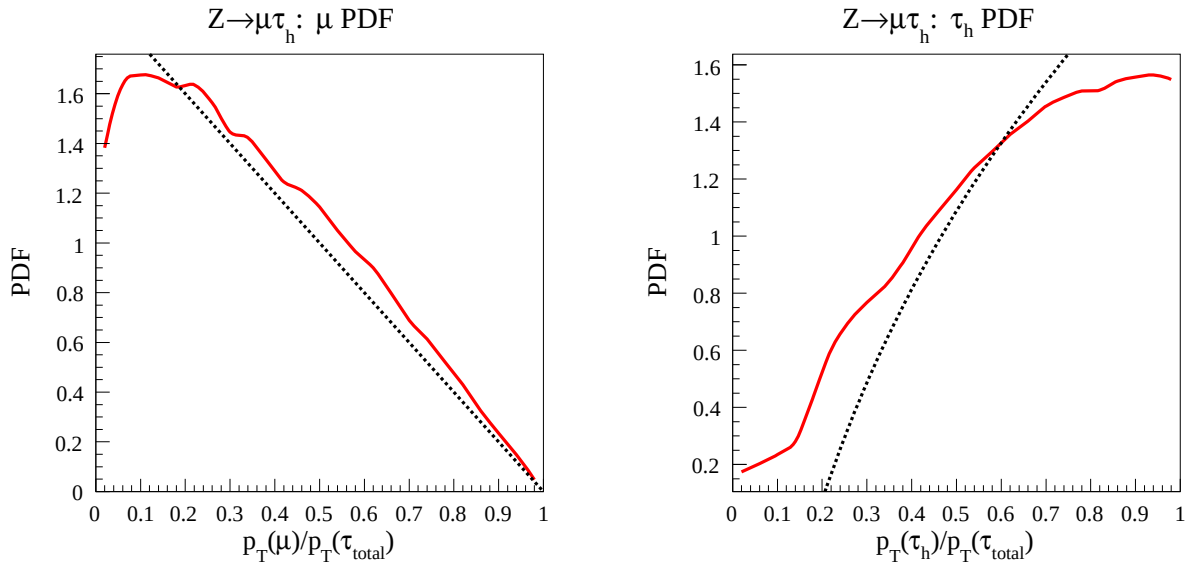

(a) (b)

Figure 6.5: Probability density functions for the p_T of a muon from a τ lepton (a), and the visible hadronic portion of a τ lepton (b) with approximate theory given in black and Monte Carlo simulation given in red.

The approximate expectation value for the τ lepton neutrino p_T is given by Equation 6.7.

$$\begin{aligned}\left\langle p_T(\nu_\tau)\right\rangle &\approx \int_0^{p_T(\tau)} x\Big(0.18 f_2(x) + 0.41 f_3(x) + 0.31 f_4(x) + 0.10 f_5(x)\Big)\, dx \\ &= p_T(\tau)\left(\frac{0.18}{2} + \frac{0.41}{3} + \frac{0.31}{4} + \frac{0.10}{5}\right) = 0.32 p_T(\tau)\end{aligned} \tag{6.7}$$

From Equation 6.7 the expected value for the visible hadronic portion of the decay is $p_T(1-0.32)$ or $0.68p_T$. Using generator level Monte Carlo which does take into account mass effects, an expected p_T fraction for the visible portion of hadronic τ leptons was found to be $0.63p_T$. For τ lepton decays to muons, an expected momentum fraction of $0.36p_T$ was found in comparison to the approximate theoretical value of $0.33p_T$. The approximate probability density functions for both the muon and the visible portion of a hadronic τ lepton decay are given in Figure 6.5 along with with the distribution obtained from Monte Carlo.

Notice that the expected momentum fractions calculated describe the shift of expected values of the probability distribution functions of Figure 6.4 very well, but do not describe the

shift in distribution shape. To understand the change in the shape of the distribution further investigation of theory and Monte Carlo is required.

6.2.2 Methods

A variety of methods do exist by which the hadronic τ lepton efficiency can be calculated with respect to p_T. However, all of these methods rely heavily on Monte Carlo, and subsequently the ability of the Monte Carlo to describe real data. The most apparent of these methods is fine tune the Monte Carlo with respect to Z production using $Z \rightarrow \mu\mu$ data. The total hadronic τ lepton efficiency can then be determined using the method of Section 6.1.1. The exact same cuts can be applied to Monte Carlo and the entire distribution is normalized such that the total efficiency between data and Monte Carlo match.

Another method is to continue the study from the previous section and accurately model the shift of the muon and hadronic τ lepton p_T distributions for the $Z \rightarrow \mu\tau_h$ processes. Using a technique similar to the total efficiency method of 6.1.1 a distribution for only signal muons and visible hadronic τ leptons can be obtained with respect to p_T. The muon distribution can be corrected with respect to efficiency and then subsequently shifted to match the visible hadronic τ lepton distribution; dividing the two histograms provides an efficiency distribution for the hadronic τ leptons with respect to p_T. Note that this method requires that not only the distribution shift can be modeled accurately but that clean signal muon and visible hadronic τ lepton distributions with respect to p_T can be obtained from data.

A final method which is currently being explored by ATLAS is embedding techniques [83]. Here $Z \rightarrow \mu\mu$ events are selected from data. The muons from the selected events are removed and replaced with a Monte Carlo τ lepton and its subsequent decay products. The event is reconstructed using the embedded τ and the efficiency can then be calculated from the embedded events. This method is possible as $Z \rightarrow \mu\mu$ and $Z \rightarrow \tau\tau$ events are kinematically identical, and the decay of the τ lepton can be well modeled using Monte Carlo. Current methods within ATLAS draw a cone around the muon and the reconstructed level and remove all tracks and calorimetry information from this cone. A simulated reconstructed τ lepton is then placed into this cone.

This method as it is in development, would not provide an accurate method by which to calculate efficiencies. However, methods being explored in CMS work directly with the raw digitized data files. Hits attributed only to the muon in the detectors are removed and then the simulated hits, attributed only to the τ lepton are overlayed. This method treats the event much more consistently and could provide an excellent method to determine efficiencies with further investigation. All of the above methods rely heavily upon Monte Carlo and require excellent agreement between Monte Carlo and data to be used effectively.

7 Conclusion

Hadronic τ lepton reconstruction and identification as can be seen from this thesis, is not a simple and straight forward task, but requires many subtleties for proper identification. In Chapter 4 both a signal cone parameterized with respect to E_T and an alternate definition of the isolation cone were explored. It was found that while CDF and CMS both use shrinking signal cones, such a definition at ATLAS is not prudent as it decreases efficiency, especially in a critical p_T region while maintaining the fake rate. Additionally, while the shape of the isolation cone can be changed, this in general does not provide any significant increase in efficiency or decrease in fakerate. This is because the space surrounding a hadronic τ lepton from a Z decay is very clean, and it is merely the absolute area of the cone that makes a difference.

Currently ATLAS has very robust methods for identifying hadronic τ leptons as is demonstrated in Chapter 5. The general variables outlined each provide a weak handle on separating hadronic τ leptons from background, but when combined using multivariate techniques, are able to provide significant discriminating power. It was found that using artificial neural nets provides the best separation between signal and background, while likelihoods provide adequate separation but with a simpler method. Boosted decision trees were also explored, and while their separation of signal and background was found to be worse than both ANN's and likelihoods, further investigation is merited.

In Chapter 6 a method for determining total hadronic τ efficiency from data was demonstrated. While further studies need to be made, the demonstration that the scale factor f cannot be naively assumed to be 1 along with the adjusting of ε_μ with respect to the p_T distribution of the measured muons are important steps in the right direction. It is clear that charge misreconstruction needs to be studied further as this will play an important role in uncertainty calculations. Additional methods for obtaining efficiency distributions with respect to η and p_T are also important, and while various methods were briefly proposed, more detailed studies need to be made.

As seen from Chapter 2 the τ lepton is critical not only for validation of SM processes but in searches for new physics. It is important that the methods used for reconstruction and identification of τ leptons are continually studied as they will provide insights and methods that can be used throughout the ATLAS experiment.

A Monte Carlo Samples

The specific samples used for this thesis are given in Table A.1. The definitions of tags listed in the dataset names of Table A.1 are given in Tables A.5 and A.4. The tag letter `g` designates a specific generator definition while `r` specifies a reconstruction definition and `s` a simulation definition. For consistency the samples used all were reconstructed using tag `r541` performed by Athena 14.2.20.3 with geometry configuration `ATLAS-GEO-02-01-00`.

Process	Dataset
$Z \rightarrow \tau\tau$	mc08.106052.PythiaZtautau.recon.AOD.e347_s462_r541
$Z \rightarrow \mu\mu$	mc08.106051.PythiaZmumu_1Lepton.recon.AOD.e347_s462_r541
QCD $b\bar{b}$	mc08.108405.PythiaB_bbmu15X.recon.AOD.e347_s462_r541
QCD Dijet	mc08.105009.J0_pythia_jetjet.recon.AOD.e344_s478_r541
	mc08.105010.J1_pythia_jetjet.recon.AOD.e344_s479_r541
	mc08.105011.J2_pythia_jetjet.recon.AOD.e344_s479_r541
	mc08.105012.J3_pythia_jetjet.recon.AOD.e344_s479_r541

Table A.1: Monte Carlo samples used for this thesis. Hyperlinks provide the PANDA monitor entry.

Two event generators were used for the samples. The $Z \rightarrow \tau\tau$ sample was generated using MC@NL0 3.1 [79] with a 10 TeV center of mass energy. The QCD dijet samples, QCD $b\bar{b}$ sample, and $Z \rightarrow \mu\mu$ sample were generated using Pythia 6.4 [84], also at a 10 TeV center of mass energy. No pile up was considered in the samples. Simulation of the detector was done using a variety of definitions, however all definitions used the same simulator and detector geometry configuration. The simulator used was GEANT 4 [85].

The cross sections for each sample are given in Table A.3. Note that the full number of events was not used for the efficiency and fakerate studies, as the full number of events for each given cross section had not been fully generated at the time this paper was written. The cross sections were calculated using MCFM [86]. The QCD dijet samples J0 through J3 each correspond to a given transverse momentum range designated in Table A.2. As discussed earlier, the cross section for low momentum dijet events is very high, while it tapers significantly for higher p_T and is of critical importance when considering optimization for reconstruction and identification algorithms.

Name	p_T Range [GeV]
J0	$8 - 17$
J1	$17 - 35$
J2	$35 - 70$
J3	$70 - 140$

Table A.2: Transverse montum bins for the QCD dijet samples.

Proccess	Cross Section [pb]	Events	Events Used
$Z \to \tau\tau$	1368.86	2×10^5	194184
$Z \to \mu\mu$	1143.96	5×10^6	31506
QCD $b\bar{b}$	8.85×10^4	5×10^4	43960
QCD J0	1.170×10^{10}	4×10^5	5000
QCD J1	8.668×10^8	4×10^5	179442
QCD J2	5.601×10^7	4×10^5	70181
QCD J3	3.280×10^6	4×10^5	23351

Table A.3: Cross sections for the samples used along with number of events corresponding to the given cross section. The final column gives number of events used for efficiency and fakerate calculations.

Tag	Date	Description	Definition
r541	2008.09.19	reconstruction tag	transfromation=csc_digi_trf.py,csc_reco_trf.py transfromation version=14.2.20.3 AddCaloDigi=False ConditionsTag=OFLCOND-SIM-00-00-03 DBRelease=5.9.1 DigiRndmSvc=AtRanluxGenSvc Geometry=ATLAS-GEO-02-01-00 JobConfig=NONE NoiseControl=NONE SamplingFractionDbTag=QGSP_BERT TriggerConfig=lumi1E31_no_Bphysics_no_prescale beamGasHits=NONE beamHaloHits=NONE cavernHits=NONE minbiasHits;ConditionsTag=NONE;OFLCOND-SIM-00-00-03 DBRelease=5.9.1 Geometry=ATLAS-GEO-02-01-00 JobConfig=SetJetConstants-02-000.py TriggerConfig=lumi1E31_no_Bphysics_no_prescale formats=RDO.AOD.ESD.NTUP cpu per event=800 memory=2000 priority =400 events per job=250

Table A.4: Reconstruction tag for samples used with detailed definition, creation date, and hyperlink to ATLAS production group page.

Tag	Date	Description	Definition
e344	2008.07.04	event generator tag	transfromation=csc_evgen08_trf.py transfromation version=14.2.0.1 Input file base=None SeedOffset=0 formats=EVNT cpu per event=30 memory=1000 priority =300 events per job=5000
e347	2008.07.21	event generator tag	transfromation=csc_evgen08_trf.py transfromation version=14.2.0.2 Input file base=None SeedOffset=0 formats=EVNT cpu per event=30 memory=1000 priority =300 events per job=5000
s462	2008.07.29	simulation tag	transfromation=csc_atlasG4_trf.py transfromation version=14.2.10.1 ConditionsTag=NONE DBRelease=5.5.1 Geometry=ATLAS-GEO-02-01-00 JobConfig=VertexPos.py PhysicsList=QGSP_BERT formats=HITS cpu per event=1200 memory=2000 priority =100 events per job=25
s478	2008.09.29	simulation tag	transfromation=csc_atlasG4_trf.py transfromation version=14.2.10.1 ConditionsTag=NONE DBRelease=5.5.1 Geometry=ATLAS-GEO-02-01-00 JobConfig=VertexPosTilted.py PhysicsList=QGSP_BERT formats=HITS cpu per event=1200 memory=2000 priority =100 events per job=25
s479	2008.10.01	simulation tag	transfromation=csc_atlasG4_trf.py transfromation version=14.2.10.1 ConditionsTag=NONE DBRelease=5.5.1 Geometry=ATLAS-GEO-02-01-00 JobConfig=VertexPos.py CalHits.py PhysicsList=QGSP_BERT formats=HITS cpu per event=1200 memory=2000 priority =100 events per job=25

Table A.5: Simulation and generator tags for samples used with detailed definition, creation date, and hyperlink to ATLAS production group page for each tag.

B Method for Assigning Errors

When performing efficiency and fakerate studies on Monte Carlo, the error assignment is not a simple task, as many approaches may be taken. Primarily, two issues must be resolved. The first issue is by which mathematical method should the error be calculated. Should standard Poisson or binomial errors be assigned or should another method be used? The second issue at hand is what the error should represent. Should the error be directly correlated to the number of events used in the study, or should it rather represent the error expected in real data?

Oftentimes the first issue is ignored, as at first glance it would appear that binomial error should be used, or in the case of a large number of events substituted with Poisson error for simplicity. However, as is fully discussed in Reference [87], and upon which this discussion is based, both these methods produce unphysical edge effects. Let N_{rec} define the number of events passing a specific criteria, in this case properly reconstructed and identified τ leptons and N_{gen} the total number of generated τ leptons or generated jets, in the case of the background.

The binomial distribution represents discrete independent events with a yes or no outcome, and would appear to be perfectly suited for the calculation of efficiency and fakerate errors. The expected value for $\langle N_{\text{rec}} \rangle$ is $\varepsilon_t N_{\text{gen}}$ where ε_t is the "true" efficiency. As the true efficiency is not available this is replaced with the measured efficiency and so the estimated binomial error is the error on the quantity N_{rec} divided by N_{gen}. The error on N_{rec} is just the square root of the variance, and so the error on the efficiency (or fakerate) is given by Equation B.1.

$$\sigma_\varepsilon = \frac{\sqrt{N_{\text{rec}}(1-\varepsilon)}}{N_{\text{gen}}} \tag{B.1}$$

This measurement for the error breaks down for the cases of $N_{\text{rec}} = 0, N_{\text{gen}}$. In both cases from the form of Equation B.1 it can be seen that the calculated error is $\sigma_\varepsilon = 0$. An error assignment of zero is of course unreasonable, as a measurement cannot be made with absolute certainty. While the error assignments for all other values of N_{rec} are reasonable, these exceptions are crucial. In nearly all efficiency plots within this thesis with respect to p_T, N_{rec} equals N_{gen} for high p_T bins. Similarly in the fakerate plots, N_{rec} equals 0 for low p_T bins. In neither case is the uncertainty on these measurements zero, and as such, binomial error assignment using the method described above is invalid.

Poisson error is often used instead of binomial error as the binomial distribution approaches the Poisson distribution for large numbers. The error for N_{rec} is then just $\sqrt{N_{\text{rec}}}$ and the same applies for N_{gen}. Using standard propagation of error the error on the efficiency or fakerate is then given by Equation B.2.

$$\sigma_\varepsilon = \left(\frac{N_{\text{rec}}^2 \left(N_{\text{rec}} + N_{\text{gen}} \right)}{N_{\text{gen}}} \right)^{1/2} \tag{B.2}$$

Again the same problem as for the binomial error occurs for $N_{\text{rec}} = 0$, the error is also equal to zero. For the case of $N_{\text{rec}} = N_{\text{gen}}$ the problem of no uncertainty no longer occurs. However, a new problem arises; the error distribution extends beyond one, and in some cases, even beyond zero. This clearly makes no sense, as an efficiency, and its subsequent error must remain within the interval of $[0, 1]$. As such, assigning error using the Poisson method is also less than desirable.

Returning to the binomial distribution, as this distribution does accurately model the events being studied for efficiency and fakerate calculations, the probability of observing N_{rec} given ε_t and N_{gen} is given by Equation B.3.

$$P\left(N_{\text{rec}}|\varepsilon_t, N_{\text{gen}}\right) = \left(\frac{N_{\text{gen}}!}{N_{\text{rec}}!\left(N_{\text{gen}} - N_{\text{rec}}\right)}\right) \varepsilon_t^{N_{\text{rec}}} (1-\varepsilon_t)^{N_{\text{gen}}-N_{\text{rec}}} \tag{B.3}$$

Using Baye's theorem [88], this probability can be rewritten for ε_t as is done in Equation B.4 where $\Gamma(x) = \int_0^\infty y^{x-1}e^{-y}\,dy$ and assuming the efficiency must fall within the range $[0, 1]$.

$$P\left(\varepsilon_t|N_{\text{rec}}, N_{\text{gen}}\right) = \left(\frac{\Gamma\left(N_{\text{gen}}\right)}{\Gamma\left(N_{\text{rec}}+1\right)\Gamma\left(N_{\text{gen}} - N_{\text{rec}} + 1\right)}\right) \varepsilon^{N_{\text{rec}}} (1-\varepsilon)^{N_{\text{gen}}-N_{\text{rec}}} \tag{B.4}$$

The error for the efficiency is then defined as the shortest interval from ε_a to ε_b on the probability distribution function defined by Equation B.4 such that the integral of this interval is one standard deviation of Gaussian error. In other words, minimize the function $\varepsilon_b - \varepsilon_a$ given that Equation B.5 holds true.

$$\int_{\varepsilon_a}^{\varepsilon_b} P\left(\varepsilon|N_{\text{rec}}, N_{\text{gen}}\right)\, d\varepsilon = \text{erf}\left(\frac{1}{\sqrt{2}}\right) \tag{B.5}$$

The solution of this minimization problem is non-trivial analytically, and so is performed numerically. The full implementation is performed using the `BayesDivide` routine implemented in ROOT. When the PDF's for Equation B.4 are plotted it can be seen that the shortcomings of the two previous methods discussed are overcome. Additionally, it is important to note that the error bars are not symmetric as the distribution is not necessarily centered around the value of ε. All efficiency and fakerate plots contained within this thesis use the above method to calculate errors.

While the mathematical method by which the error should be calculated has been demonstrated, what the errors represent has not yet been explained. While it is at times beneficial to demonstrate error with respect to what real data would look like, this is in general not the case for optimization studies of Monte Carlo. As such, the error for all calculated efficiencies is directly proportional to the number of events within the signal Monte Carlo sample used. For the case of the fakerates the situation becomes slightly more complex as now the background is split into four samples as explained in Appendix A.

Ideally this should not cause a problem when the fakerate is plotted with respect to p_T as the p_T of each generated jet should fall within its specific sample binning. This is not the case however, as the generator level reconstruction of jets does not match the Pythia generation of the jets and as such there is overlap between the samples. Normalizing all the samples with respect to their cross sections is one solution to this, but the error no longer represents the statistical uncertainty due to the size of the Monte Carlo sample. Additionally, due to the distinct differences in cross sections between the p_T bins it was found that any fakerate behavior in the high p_T region would be washed out. To provide an accurate representation of the actual error within the study the samples were added together without scaling for distributions with respect to p_T. For distributions with respect to η and ϕ the samples were normalized such that the number of events in the Monte Carlo sample with the largest cross section was maintained.

C Analysis Framework

The ATLAS analysis and reconstruction framework ATHENA is a derivative of the GAUDI framework developed initially for LHC-b but extended as a common framework between various physics experiments [89]. The primary code base of ATHENA is developed in C++ and is managed through the Configuration Management Tool (CMT) [90] which is intended to give the framework a highly modularized structure. CMT configures the files necessary to build packages, while the compiled code itself is run through Python wrappers to provide additional job options for individual runs.

The ATHENA reconstructed event model is broken into three levels of data containers: Event Summary Data (ESD), Analysis Object Data (AOD), and Derived Physics Data (DPD) [91]. The ESD is the most detailed of the containers with information that is often not necessary for most physics analyses. The AOD is less detailed but still contains nearly all relevant information necessary for a physics analysis. The DPD is highly specific to various work groups and no common format is currently used between groups. Both the ESD and AOD are only accessible through the ATHENA framework, while DPD's may be accessed through ROOT.

While the theory behind the ATHENA framework and data model is sound, the implementation is less than ideal. A decentralized development environment with no quality assurance or testing, lack of documentation, and lack of coordination has led to an analysis system that is oftentimes unusable. An example of this is compiling the standard "hello world" analysis skeleton outlined in various ATHENA tutorials. Using a standard installation of ATHENA 14.2.21, compile time (using the BASH `time` command) took 2 minutes and 55 seconds with the compiled code being linked to 156 libraries. Upon subsequent recompiles the behavior remained similar.

For performing a physics analysis such a compile time is unacceptable as turn around time for code development now is limited primarily by the long compile times. Ideally, for an agile development cycle a compile time on the order of seconds, and certainly not on the order of minutes, is necessary. This issue should be addressed directly by developing the configuration tool such that compilation and linking is done intelligently using a minimal number of recompiles and linkages. Unfortunately such a task was not within the scope of this project and so other methods were used to overcome these difficulties.

As this problem is common within ATLAS, the DPD was developed to allow for external analysis of data using only ROOT libraries. The DPD is written as a ROOT ntuple with all variables accessible using only ROOT libraries. However, current DPD's are written as flat ntuples, requiring rewriting of analysis code every time a variable is added to the ntuple structure. A flat format also leads to a highly complicated and non-intuitive interface for the user with variables for individual objects being spread over a variety of branches. Additionally, reading variables from a flat ntuple into a structured object for analysis is not good coding practice when the ntuple can contain these objects itself.

However, loading user written libraries into ATHENA such that structured ntuples can be written is a non-trivial task. Structured ntuples have been created using ATHENA, but currently are not in widespread use as the difficulties of properly loading definitions into ROOT is a hindrance for the end user. Ideally a structure needs to be available such that the end user can

simply access the ntuple in ROOT directly with no additional configuration on their part.

To accomplish this, an analysis skeleton was written during the writing of this thesis that, while far from perfect, does address many of the issues above. The framework consists of three components: an ntuple maker that runs directly through ATHENA and needs only be modified on occasion, an object library of structured physics objects such as muons, etc., and an analysis frame that can read the ntuple created by the ntuple maker.

The object library provides classes for τ leptons, muons, electrons, jets, tracks, missing energy, and generator level particles. All classes derive from a base particle class which consists of a basic four momentum vector and an assigned charge. The base class has all the methods available to the `TLorentzVector` class in ROOT, but in a standardized and documented fashion. The derived classes have the standard addition and subtraction operators defined and downcast to the base particle when added or subtracted to the other available classes.

Two constructors are provided for each class besides the base constructor. The first constructor accepts the arguments individually, for example:

```
particle *example = new particle(double E, double PX, double PY,
                                 double PZ, double CHARGE)
```

while the second constructor accepts as an argument two vectors of doubles.

```
tau *example = new tau(vector<double> FOURMOMENTUM,
                       vector<double> ADDITIONALINFO)
```

A full example of the header file for the generator level particle class is given in Listing C.1 and demonstrates some of the specialized methods available to the derived classes.

The second constructor is designed specifically to read objects created by the ntuple maker. In general, any physics object can be represented by two vectors of doubles. The first vector provides the basic kinematic information for that object, the four momentum vector and charge. The second vector carries additional information regarding the specifics of that object. For generator level particles two additional vectors are required as can be seen from Listing C.1. The first vector provides the barcodes of parent particles while the second provides the barcodes of child particles. Technically only one of these vectors is needed, but by providing both, a significant speedup occurs when searching for children or parents of a particle.

By using vectors of doubles the structure of the ntuple created remains the same, even when more information needs to be added to the ntuple. Additional information for an object can be simply pushed back into the additional information vector, while keeping the structure of the ntuple the same. A simple modification to the constructor of the specific class and the information is available within the analysis framework. Backwards compatibility can be maintained in a fully automated fashion by adding a version tag to the ntuple that is automatically read by the constructor. This even allows for the sharing of ntuples between various work groups with a specific tag given for each specialized ntuple. Most importantly, no additional configuration of ROOT is required as vectors are supported directly.

The ntuple maker writes structured ntuples directly to this format which are then read by the analyzer. The analyzer links to the specific object libraries discussed above, and for each event writes all the objects to a vector of the corresponding class for the object. As the libraries are small, compile time is fast (less than a second) and analysis is simple using the structured classes. The analyzer can be modularized by specific methods, and an options class allows for a job options file to be read which switches on and off components of the analyzer.

This three part analysis framework provides several advantages over the current methods being employed at ATLAS.

- Development cycle is fast and on the order of seconds rather than minutes.
- Code is structured with physics objects so that common code is reused, and done properly, once.
- Ntuples are structured, but in such a way that additional configuration of ATHENA and ROOT is not required.
- Ntuple tree format does not change with the addition of variables.
- Ntuples and code can be shared between groups with an underlying base.
- Versions of ntuples can automatically be accounted for using specific tags, and the constructors can adjust accordingly.

Ideally, however, the problem of the ATHENA framework should be solved by a consolidation and rewriting of code done by professional software developers using a realistic software development cycle. Until then, the method described above provides an adequate alternative for small scale analysis.

Listing C.1: Header file for the generator level particle class used in the writing of this thesis.

```
class generated : public particle
{
protected:
  // variables
  int pdgid;
  int barcode;
  int status;
  vector<int> parents;
  vector<int> children;
public:
  // methods
  int PdgId();
  int Barcode();
  int Status();
  vector<int> Parents();
  vector<int> Children();
  void SetPdgId(int PDGID);
  void SetBarcode(int BARCODE);
  void SetStatus(int STATUS);
  void SetParents(vector<int> PARENTS);
  void SetChildren(vector<int> CHILDREN);
  int  NumberOfParents();
  int  NumberOfChildren();
  void ReturnParents(vector<generated*> *OUT, vector<generated*> *DATA);
  void ReturnChildren(vector<generated*> *OUT, vector<generated*> *DATA);
  void ReturnAllChildren(vector<generated*> *OUT, vector<generated*> *DATA);
  void ReturnFinalChildren(vector<generated*> *OUT, vector<generated*> *DATA);
  bool HasParent(int PDGID, int STATUS, vector<generated*> *DATA);
  bool HasChild(int PDGID, int STATUS, vector<generated*> *DATA);
  // constructors
  generated();
  generated(double E, double PX, double PY, double PZ, double CHARGE,
       int PDGID, int BARCODE, int STATUS, vector<int> PARENTS,
       vector<int> CHILDREN);
  generated(vector<double> A, vector<double> B, vector<int> C,
            vector<int> D);
  // destructor
  ~generated ();
};
```

D Higgs Decay and Cross Section Calculations

All SM and MSSM Higgs boson decay widths of Figures 2.4 and 2.5 were calculated using `HDECAY` [25] which is available from Michael Spira at http://people.web.psi.ch/spira/proglist.html. An Octave [92] wrapper was written for the compiled FORTRAN code to allow for simple and fast analysis and plotting of the returned decay widths. This code is available upon request by emailing Philip Ilten at philten@gmail.com. For the MSSM model the parameters were adjusted to reflect the $m_{h^0}^{\max}$ scenario as outlined in Reference [27]. The relevant parameters are given in Table D.1. The input file `hdecay.in` used is given in Listing D.1.

Parameter	Value	Parameter	Value
m_t	174.3 GeV	M_{SUSY}	1 TeV
μ	200 GeV	M_2	200 GeV
X_t^{OS}	$2M_{SUSY}$	$X_t^{\overline{\mathrm{MS}}}$	$\sqrt{6}M_{SUSY}$
A_b	A_t	$M_{\tilde{g}}$	$0.8M_{SUSY}$

Table D.1: Parameters for the $m_{h^0}^{\max}$ MSSM benchmark scenario [27].

The cross sections of Figures 2.4 and 2.7 were produced using `HIGLU`, `VV2H`, `V2HV`, and `HQQ`. The programs were written by Michael Spira and are available through the website given earlier. Again an Octave wrapper was written for the above programs to facilitate fast and simple manipulation of the returned calculations. The MSSM benchmark parameters of Table D.1 were used for all MSSM plots. An example input file for `HIGLU` is given in Listings D.2 and D.3. The input files for the remaining programs are similar.

The plots made for both cross sections and decay widths were checked against plots from Reference [93] to ensure accuracy. Slight deviations exist between the plots of this paper and the plots of Reference [93] but are most probably due to small differences in calculation methods and input parameters. An additional check was made using `FEYNHIGGS` version 2.6.5 [94] which is available at http://www.feynhiggs.de. An Octave wrapper was also written for `FEYNHIGGS` and is available upon request.

Figure D.1 shows the results from using `FEYNHIGGS` and matches relatively well with the results obtained from the Spira programs. Masses below $M_{A^0} = 100$ GeV were not available for calculation and so the plots range only from 100 to 500 GeV. Additionally, weak boson fusion calculations were not available for all MSSM Higgs types, while associated W and Z production calculations were not available for the A^0.

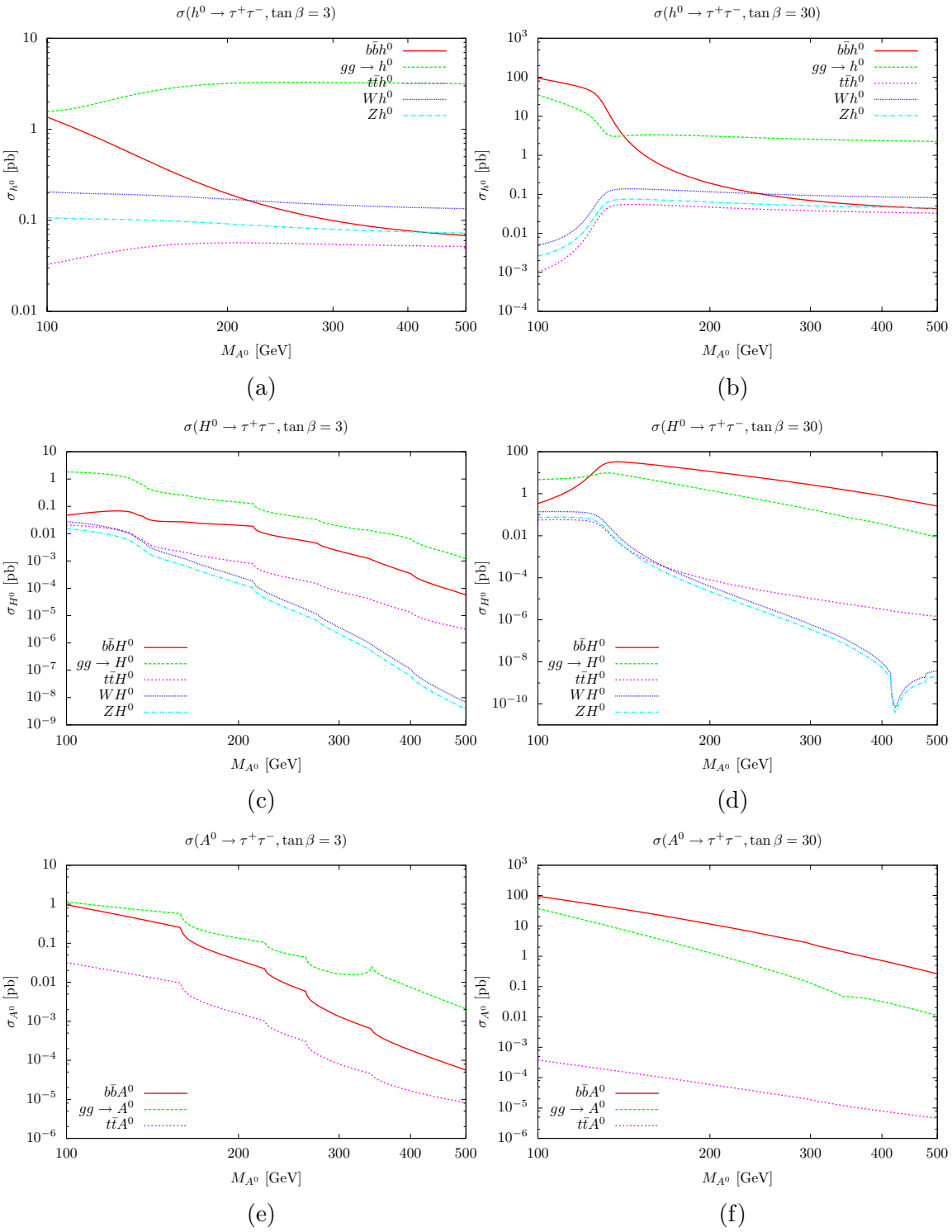

Figure D.1: The equivalent plots of Figure 2.7 but produced using `FEYNHIGGS`. Weak boson fusion calculations for all MSSM Higgs types along with associated W and Z production for A^0 were not possible with `FEYNHIGGS`.

Listing D.1: Input file `hdecay.in` for calculating decay widths using `HDECAY`.

```
SLHAIN    = 0
SLHAOUT   = 0
HIGGS     = XXXXX
MODEL     = 1
TGBET     = XXXXX
MABEG     = XXXXX
MAEND     = XXXXX
NMA       = XXXXX
ALS(MZ)   = 0.118D0
MSBAR(1)  = 0.190D0
MC        = 1.40D0
MB        = 4.60D0
MT        = 174.3D0
MTAU      = 1.7771D0
MMUON     = 0.105658389D0
1/ALPHA   = 137.0359895D0
GF        = 1.16639D-5
GAMW      = 2.080D0
GAMZ      = 2.490D0
MZ        = 91.187D0
MW        = 80.41D0
VUS       = 0.2205D0
VCB       = 0.04D0
VUB/VCB   = 0.08D0
MU        = 200.D0
M2        = 200.D0
MGLUINO   = 800.D0
MSL1      = 1000.D0
MER1      = 1000.D0
MQL1      = 1000.D0
MUR1      = 1000.D0
MDR1      = 1000.D0
MSL       = 1000.D0
MER       = 1000.D0
MSQ       = 1000.D0
MUR       = 1000.D0
MDR       = 1000.D0
AL        = 1000.D0
AU        = 1000.D0
AD        = 1000.D0
NNLO (M)  = 0
ON-SHELL  = 0
ON-SH-WZ  = 0
IPOLE     = 0
OFF-SUSY  = 1
INDIDEC   = 0
NF-GG     = 5
IGOLD     = 0
MPLANCK   = 2.4D18
MGOLD     = 1.D-13
```

Listing D.2: First part of input file `higlu.in` used for calculating gluon gluon fusion cross sections using `HIGLU`.

```
PROCESS:   0 = GG --> H            1 = H --> GG
=========

PROCESS  = 0
-------------------------------------------------------------------------
COLLIDER:    0 = P P                 1 = P PBAR
=========

COLLIDER = 0
-------------------------------------------------------------------------
TOTAL ENERGY: [TEV]
=============

ENERGY   = 14.D0
-------------------------------------------------------------------------
MODEL:     0 = SM    MSSM: 1 = SUBHPOLE  2 = SUBH
=======                    3 = FEYNHIGGSFAST

MODEL    = XXXXX
-------------------------------------------------------------------------
TAN(BETA): (MSSM)
==========

TANBETA  = XXXXX
-------------------------------------------------------------------------
COUPLINGS:   G_B = BOTTOM     G_T = TOP
==========   (MODEL = 0)

G_B      = 1.D0
G_T      = 1.D0
-------------------------------------------------------------------------
QUARK MASSES: [GEV]
============

M_SB(1)  = 0.190D0
M_C      = 1.40D0
M_B      = 4.60D0
M_T      = 174.3D0
-------------------------------------------------------------------------
HIGGS TYPE AND MASS [GEV]: 1 = HEAVY SCALAR 2 = PSEUDOSCALAR 3 = LIGHT SCALAR
=========================  INDIVIDU = 0: M_HIGGS = M_A

TYPE     = XXXXX
INDIVIDU = 0
M_HIGGS  = XXXXX
-------------------------------------------------------------------------
SCALES: [GEV] MU = MU_1*M_HIGGS + MU_2:   RENORMALIZATION SCALE
========      Q =  Q_1*M_HIGGS +  Q_2:     FACTORIZATION SCALE

MU_1     = .2D0
MU_2     = 0.D0
Q_1      = 1.D0
Q_2      = 0.D0
-------------------------------------------------------------------------
ORDER OF ALPHA_S:   1 = LO      2 = NLO
================

LOOP     = 2
-------------------------------------------------------------------------
DEFINITION OF ALPHA_S:   1 = ALPHA_S (M_Z)   2 = BY LAMBDA (N_F)
======================

CHOICE   = 1
-------------------------------------------------------------------------
ALPHA_S (M_Z):
=============

ALPHA_S  = 0.118D0
-------------------------------------------------------------------------
LAMBDA_NF: [GEV] (QCD SCALE)
==========

N_F      = 3
LAMBDA   = 0.226D0
-------------------------------------------------------------------------
```

Listing D.3: Second part of input file `higlu.in` used for calculating gluon gluon fusion cross sections using `HIGLU`.

```
NUMBER OF EXTERNAL LIGHT FLAVORS: (FOR H --> GG)
================================

N_EXT     = 5
------------------------------------------------------------------
VEGAS:          ABSERR = ABSOLUTE ERROR
=====           POINTS = NUMBER OF CALLS
                ITMAX  = NUMBER OF ITERATIONS
                PRINT  = PRINT OPTION FOR INTERMEDIATE VEGAS-OUTPUT
                  0              1              10
                  NO OUPUT       PRETTYPRINT    TABLE

ABSERR    = 0.D0
POINTS    = 10000
ITMAX     = 5
PRINT     = 10
------------------------------------------------------------
STRUCTURE FUNCTIONS: STFUN: 0 = PDFLIB   1 = GRV    NGROUP: -1 = CTEQ6
==================== SCHEME = FACTORIZATION SCHEME: 0 = MSBAR    1 = DIS

STFUN   =  0
SET     =  2
SCHEME  =  0
NGROUP  = -1
NSET    =  1
------------------------------------------------------------------
PARAMETERS: (FOR RAD. CORR. OF SUSY-COUPLINGS)
==========
              MZ    = Z-MASS [GEV]
              MSQ   = SQUARK-MASS [GEV]

GF        =  1.16639D-5
MZ        =  91.187D0
MW        =  80.41D0
MGLUINO   =  800.D0
MSQ       =  1000.D0
MUR       =  1000.D0
MDR       =  1000.D0
M2        =  200.D0
MU        =  200.D0
AU        =  0.D0
AD        =  0.D0
```

Bibliography

[1] P. Ilten, *A Study of Tau Identification with the CMS Detector at the LHC*, Massachusetts Institute of Technology (June 2008), Bachelor of Science Thesis.

[2] R. Mohapatra and et al, *Theory of neutrinos: A white paper*, Reports on Progress in Physics **70** (2007) 1757, hep-ph/0510213.

[3] M. Peskin and V. Schroeder, *An Introduction to Quantum Field Theory*, Westveiw Press, 8th edn., (1995).

[4] D. Griffiths, *Introduction to Elementary Particles*, Wiley-VCH, 2nd edn., (2008).

[5] F. Halzen and A. Martin, *Quarks and Leptons: An Intorductory Course in Modern Particle Physics*, Wiley, 1st edn., (1984).

[6] P. Higgs, *Broken Symmetries and the mass of gauge bosons*, Physical Review Letters **13(16)** (October 1964) 508.

[7] R. Feynman and M. Gell-Man, *Theory of the Fermi Interaction*, Physical Review **109(1)** (January 1957) 193.

[8] S. Weinberg, *A Model of Leptons*, Physical Review Letters **19(21)** (November 1967) 1264.

[9] A. Salam, *Weak and electromagnetic interactions*, in: *Elementary Particle Theory, Proceedings Of The Nobel Symposium Held 1968 At Lerum, Sweden, Stockholm*, (1968), 1968 367–377.

[10] G. 't Hooft, *Renormalizable Lagrangians for Massive Yang-Mills Fields*, Nulcear Physics **B(35)** (July 1971) 167.

[11] H. Georgi and S. Glashow, *Unity of All Elementary-Particle Forces*, Physical Review Letters **32(8)** (February 1974) 438.

[12] A. Natale and R. Shellard, *The gauge heirarchy problem*, Journal of Physics G: Nuclear and Particle Physics **8** (1982) 635.

[13] H. Haber, *Supersymmetry, Part I (Theory)*, Physics Letters **B(667)** (October 2008) 1.

[14] S. Martin, *A Supersymmetry Primer*, hep-ph/9709356.

[15] M. Perl and et al, *Evidence for Anomalous Lepton Production in e^+e^- Annihilation*, Physical Review Letters **35(22)** (December 1975) 1489.

[16] M. Acciarri and et al, *Measurement of the lifetime of the tau lepton*, Physics Letters **B(479)** (April 2000) 67.

[17] W. Marciano and A. Sirlin, *Electroweak Radiative Correction to tau Decay*, Physical Review Letters **61(16)** (October 1988) 1815.

[18] M. Yao and et al, *Review of Particle Physics*, The European Physical Journal **B(667)** (2008) 1+.

[19] M. Perl, *The tau lepton*, Reports on Progress in Physics **55** (1992) 653.

[20] A. Martin, R. Roberts, W. Stirling, and R. Thorne, *Parton distributions and the LHC: W and Z production*, European Physical Journal **C14** (2000) 133, hep-ph/9907231.

[21] A. Ahmad and et al, *Search for the Standard Model Higgs boson via Vector Boson Fusion production process in the di-tau channels with ATLAS*, ATLAS Note **ATL-PHYS-INT(2008-000)** (October 2008) 1.

[22] J. Ellis, M. Galliard, and D. Nanopoulos, *A Phenomenological Profile of the Higgs Boson*, Nuclear Physics **B(106)** (November 1975) 292.

[23] W. Lee, C. Quigg, and H. Thacker, *Strength of Weak Interactions at Very High Energies and the Higgs Boson Mass*, Physical Review Letters **38(16)** (April 1977) 883.

[24] M. Spira and et al, *QCD effects in Higgs physics*, Fortschritte der Physik **46** (April 1999) 203.

[25] A. Djouadi, J. Kalinowski, and M. Spira, *HDECAY: A program for Higgs boson decays in the standard model and its supersymmetric extension*, Computer Physics Communication **108** (1998) 56, hep-ph/9704448.

[26] G. Aad and et al, *Expected Performance of the ATLAS Experiment Detector, Trigger and Physics*, ATLAS Note **CERN-OPEN(2008-020)** (December 2008) 1.

[27] M. Carena, S. Heinemeyer, C. Wagner, and G. Weiglein, *Suggestions for benchmark scenarios for MSSM Higgs boson searches at hadron colliders*, European Physical Journal **C26** (2003) 601, hep-ph/0202167.

[28] ATLAS Collaboration, *ATLAS Detector and Physics Performance Technical Design Report*, ATLAS Note **ATLAS TDR(015)** (May 1999) 459.

[29] R. Chierici, *Search fo new physics with τs at the LHC*, Nuclear Physics **B(144)** (2004) 349.

[30] C. Hensel, *Personal Communication*.

[31] O. Bruning, P. Collier, P. Lebrun, S. Myers, R. Ostojic, J. Poole, and P. Proudlock, *LHC Design Report*, CERN, Geneva, (2004).

[32] H. Wiedemann, *Synchrotron Radiation*, Springer, 5th edn., (2003).

[33] C. Kim, *A 3-D Touschek Scattering Theory*, in: *Sixth European Particle Accelerator Conference*, (June 1998), 1998 1–3.

[34] C. Hill, A. Lombardi, R. Scrivens, and M. Vretenar, *Test of the CERN LINAC Performance for LHC-type Beams*, in: *XX International Linac Conference*, (August 2000), 2000 590–592.

[35] K. Reich, *The CERN Proton Synchrotron Booster*, IEEE Transactions on Nuclear Science **16(3)** (June 1969) 959.

[36] M. Benedikt and et al, *The PS Complex as Proton Pre-Injector for the LHC - Design and Implementation Report*, CERN, Geneva, (2000).

[37] K. Schindl, *The Injector Chain for the LHC*, in: *9th LEP Performance Workshop in Chamonix*, (1999), 1999 47–52.

[38] G. Aad and et al, *The ATLAS Experiment at the CERN Large Hadron Collider*, Journal of Instrumentation **3(S08003)** (August 2008) 1.

[39] A. Yamamoto and et al, *The ATLAS central solenoid*, Nuclear Instruments and Methods in Physics Research Section A: Accelerators, Spectrometers, Detectors and Associated Equipment **584(1)** (2008) 53.

[40] ATLAS Collaboration, *ATLAS Detector and Physics Technical Design Report*, ATLAS Note **ATLAS TDR(014)** (May 1999) 1.

[41] D. Baynham and et al, *Engineerinig Status of the Superconducting End Cap Toroid Magnets for the ATLAS Experiment at LHC*, IEEE Transactions on Applie Superconductivity **10(2)** (March 2000) 357.

[42] M. Aleksa and et al, *Measurement of the ATLAS solenoid magnetic field*, Journal of Instrumentation **3(P04003)** (April 2008) 1.

[43] G. Aad and et al, *ATLAS pixel detector electronics and sensors*, Journal of Instrumentation **3(P07007)** (July 2008) 1.

[44] A. Ahmad and et al, *The silicon microstrip sensors of the ATLAS semiconductor tracker*, Nuclear Instruments and Methods in Physics Research **A(578)** (2007) 98.

[45] E. Abat and et al, *The ATLAS Transition Radiation Tracker (TRT) proportional drift tube: design and performance*, Journal of Instrumentation **3(P02013)** (February 2008) 1.

[46] J. Hostachy, *Construction and test results of the ATLAS EM barrel calorimeter and presampler*, Nuclear Physics B - Proceedings Supplements **125** (2003) 112 , Innovative Particle and Radiation Detectors.

[47] M. Aharrouche and et al, *Energy linearity and resolution of the ATLAS electromagnetic barrel calorimeter in an electron test-beam*, Nuclear Instruments and Methods in Physics Research **A(568)** (August 2006) 601.

[48] B. Aubert, *Construction, assembly and tests of the ATLAS electromagnetic barrel calorimeter*, Nuclear Instruments and Methods in Physics Research Section A: Accelerators, Spectrometers, Detectors and Associated Equipment **558(2)** (2006) 388.

[49] M. Aleksa and et al, *Construction, assmebly and test of the ATLAS electromagnetic end-cap calorimeters*, Journal of Instrumentation **3(P06002)** (June 2008) 1.

[50] J. Abdallah and et al, *Design, Construction and Installation of the ATLAS Hadronic Barrel Scintillator -Tile Calorimeter*, ATLAS Note **ATL-ATL-COM-TILECAL(2007-019)** (July 2008) 1.

[51] H. Okawa, *Commissioning of the ATLAS tile calorimeter with cosmic ray and single beam data*, ATLAS Note **ATL-TILECAL-PROC(2008-002)** (November 2008) 1.

[52] S. Akhmadaliev and et al, *Results from a new combined test of an electromagnetic liquid argon calorimeter with a hadronic scintillating-tile calorimeter*, Nuclear Instruments and Methods in Physics Research Section A: Accelerators, Spectrometers, Detectors and Associated Equipment **449(3)** (2000) 461.

[53] S. Palenstini, *The Muon Spectrometer of the ATLAS Experiment*, Nuclear Physics **B(125)** (2003) 337.

[54] J. Wotschack, *ATLAS Muon Chamber Construction Parameters for CSC, MDT, and RPC chambers*, ATLAS Note **ATL-MUON-PUB(2008-006)** (April 2008) 1.

[55] R. Achenbach, *The ATLAS Level-1 Calorimeter Trigger*, Journal of Instrumentation **3(P03001)** (March 2008) 1.

[56] M. Casado and et al, *The ATLAS tau trigger*, ATLAS Note **ATL-DAQ-PROC(2008-008)** (December 2008) 1.

[57] A. Kalinowski, *Tau Lepton Reconstruction and ID with the ATLAS Detector at the LHC*, in: *10th International workshop on Tau Lepton Physics*, (September 2008), 2008 1–14.

[58] S. Gennai and et al, *Tau jet reconstruction and tagging at High Level Trigger and off-line*, CMS Note **2006(028)** (January 2006) 1.

[59] The CDF Collaboration, *Search for New Physics with High Mass Tau Pairs in CDF*, CDF Note **7176** (November 2004) 1.

[60] J. Lagarias, J. Reeds, M. Wright, and P. Wright, *Convergence Properties of the Nelder-Mead Simplex Method in Low Dimensions*, SIAM Journal on Optimization **9(1)** (December 1998) 112.

[61] A. Nelder and R. Mead, *A simplex method for function minimization*, The Computer Journal **7(4)** (January 1965) 308.

[62] The Mathworks Inc., Natick, Massachusetts, *MATLAB*, (January 2007), Version 7.4.0.287 (R2007a).

[63] Z. Czyczula, *Tau Physics with First Data in ATLAS*, ATLAS Note **ATL-PHYS-PROC(2008-079)** (December 2008) 1.

[64] R. Brenner, *The ATLAS hadronic tau trigger - performance and early running plans*, in: *Prospects For Charged Higgs Discovery At Colliders*, (September 2008), 2008 1–24.

[65] B. Gosdzik, *Status report on tauID with safe variables*, in: *ATLAS Tau Meeting*, (December 2008), 2008 1–25.

[66] J. Aldrich, *R. A. Fisher and the Making of Maximum Likelihood 1912 - 1922*, Statistical Science **12(3)** (August 1997) 162.

[67] K. Benslama and et al, *Tau identification using the TauDiscriminant package*, ATLAS Note **ATL-COM-PHYS(2008-212)** (November 2008) 1.

[68] M. Wolter, *Tau identification using multivariate techniques in ATLAS*, ATLAS Note **ATL-PHYS-PROC(2009-016)** (January 2009) 1.

[69] F. Rosenblatt, *The Perceptron: A Perceiving and Recognizing Automaton, Project PARA*, Cornell Aeronautical Laboratory Report 85-460-1.

[70] M. Minsky and S. Papert, *Perceptrons, An Introduction to Computational Geometry*, MIT Press, (1969).

[71] G. Cybenko, *Approximation by Superpositions of a Sigmoidal Function*, Mathematics of Control, Signals, and Systems **2** (1989) 303.

[72] H. Siegelmann and E. Sontag, *Turing Computability with Neural Nets*, Applied Mathematics Letters **4** (1991) 77.

[73] A. Zell and et al, *Stuttgart Neural Network Simulator*, University of Stuttgart and University of Tübingen, 4th edn., (2000).

[74] Y. Freund and R. Schapire, *A Short Introduction to Boosting*, Journal of Japanese Society for Artificial Intelligence **14(5)** (September 1999) 770.

[75] Y. Freund and R. Schapire, *A decision-theoretic generalization of on-line learning and an application to boosting*, Journal of Computer and System Sciences **55(SS971504)** (December 1997) 119.

[76] J. Godfrey and D. O'Neil, *Using Boosted Decision Trees for Tau ID in ATLAS*, in: *PPD CAP 2008*, (June 2008), 2008 1–21.

[77] B. Roe, H. Yang, J. Zhu, Y. Liu, I. Stancu, and G. McGregor, *Boosted Decision Trees as an Alternative to Artificial Neural Networks for Particle Identification*, Nuclear Instruments and Methods in Physics Research **543** (2005) 577.

[78] A. Kalinowskim and A. Nikitenko, *Measurement of the tau tag efficiency using the* $Z \to \tau\tau \to \mu + hadrons + X$ *events*, CMS Note **2006(074)** (May 2006) 1.

[79] S. Frixione and B. Webber, *Matching NLO QCD computations and parton shower simulations*, Journal of High Energy Physics **2002(06)** (2002) 029.

[80] S. Hassani, *STACE Status*, in: *Freiburg*, (October 2004), 2004 1–11.

[81] M. Schott, *Z Boson Production and Properties at LHC*, in: *EPS Conference*, (2007), 2007 1–15.

[82] S. Myers, *Summary of Chamonix 09*, in: *ATLAS Week*, (January 2009), 2009 1–47.

[83] J. Kroseberg and et al, *Estimation of* $Z \to \tau\tau$ *from data using embedding*, in: $M_{\tau\tau}$ *Conference*, (January 2009), 2009 1–13.

[84] T. Sjöstrand, S. Mrenna, and P. Skands, *PYTHIA 6.4 physics and manual*, JHEP **05** (2006) 026, hep-ph/0603175.

[85] J. Allison, , and et al, *Geant4 developments and applications*, IEEE Transactions on Nuclear Science **53(1)** (February 2006) 270.

[86] Fermi National Accelerator Laboratory, Batavia, Illinios, *MCFM*, (July 2007), MCFM v5.2.

[87] M. Paterno, *Calculating Efficiencies and Their Uncertainties*, FNAL/CD/CEPA/SLD.

[88] T. Bayes, *An Essay towards solving a Problem in the Doctrine of Changes*, Personal Letters.

[89] LHCb Software Architecture Group, CERN, Switzerland, *GAUDI*, (1998).

[90] Laboratoire de l'Accélérateur Linéaire, Orsay Cedex, France, *CMT*, (2009).

[91] A. Farbin, *ATLAS analysis model*, Journal of Physics Conference Series **119(4)** (July 2008) 042012.

[92] Department of Chemical Engineering, University of Wisconsin, Madison, Wisconsin, *Octave*, (2007), Version 3.0.0.

[93] A. Djouadi, *The Anatomy of electro-weak symmetry breaking. II. The Higgs bosons in the minimal supersymmetric model*, Physical Reports **459** (2008) 1, hep-ph/0503173.

[94] S. Heinemeyer, W. Hollik, H. Rzehak, and G. Weiglein, *The Higgs sector of the complex MSSM at two-loop order: QCD contributions*, Physics Letters **B652** (2007) 300, 0705.0746.

Acknowledgements

I would like to thank first and foremost Markus Klute, who made this thesis possible. He always has time to talk about physics and has done more for me than should be expected from any thesis supervisor. Markus is not only a scholar and a gentleman, but an incredible individual. I owe a debt of gratitude to the Krupp Foundation for providing funding for my position and their general support of scientific research in Germany. The entire HEP group here at Göttingen has provided invaluable help and this thesis would not be possible without their contributions. I would especially like to thank Ulla Blumenschein, Despoina Evangelakou, Katharina Fiekas, Adam Roe, Carsten Hensel, Michael Uhrmacher, and Professor Arnulf Quadt.

Of course I would not be here without my family: Mark and Karen, Jennifer, Adam and Zoe, and Nathan and Carla. I also would not have finished this thesis with my sanity intact without Éadaoin to whom I owe a special thanks.

This thesis is dedicated to my grandparents, Bob and Pat Ilten.